TU/e EINDHOVEN UNIVERSITY OF TECHNOLOGY

Laminar burning velocities at elevated pressures using the heat flux method

Citation for published version (APA):
Goswami, M. (2014). *Laminar burning velocities at elevated pressures using the heat flux method*. [Phd Thesis 1 (Research TU/e / Graduation TU/e), Mechanical Engineering]. Technische Universiteit Eindhoven. https://doi.org/10.6100/IR766389

DOI:
10.6100/IR766389

Document status and date:
Published: 01/01/2014

Document Version:
Publisher's PDF, also known as Version of Record (includes final page, issue and volume numbers)

Please check the document version of this publication:

• A submitted manuscript is the version of the article upon submission and before peer-review. There can be important differences between the submitted version and the official published version of record. People interested in the research are advised to contact the author for the final version of the publication, or visit the DOI to the publisher's website.
• The final author version and the galley proof are versions of the publication after peer review.
• The final published version features the final layout of the paper including the volume, issue and page numbers.

Link to publication

General rights
Copyright and moral rights for the publications made accessible in the public portal are retained by the authors and/or other copyright owners and it is a condition of accessing publications that users recognise and abide by the legal requirements associated with these rights.

• Users may download and print one copy of any publication from the public portal for the purpose of private study or research.
• You may not further distribute the material or use it for any profit-making activity or commercial gain
• You may freely distribute the URL identifying the publication in the public portal.

If the publication is distributed under the terms of Article 25fa of the Dutch Copyright Act, indicated by the "Taverne" license above, please follow below link for the End User Agreement:

www.tue.nl/taverne

Take down policy
If you believe that this document breaches copyright please contact us at:

openaccess@tue.nl

providing details and we will investigate your claim.

Download date: 16. Nov. 2023

Laminar Burning Velocities at Elevated Pressures using the Heat Flux Method

PROEFSCHRIFT

ter verkrijging van de graad van doctor aan de
Technische Universiteit Eindhoven, op gezag van de
rector magnificus, prof.dr.ir. C.J. van Duijn, voor een
commissie aangewezen door het College voor
Promoties in het openbaar te verdedigen
op maandag 7 april 2014 om 16.00 uur

door

Mayuri Goswami

geboren te Jorhat, India

Dit proefschrift is goedgekeurd door de promotoren en de samenstelling van de promotiecommissie is als volgt:

Voorzitter:	prof.dr.ir. M.G.D. Geers
1^{e} promotor:	prof.dr. L.P.H. de Goey
2^{e} promotor:	prof.dr. A.A. Konnov
copromotor:	dr.ir. R.J.M. Bastiaans
leden:	prof.dr. F.N. Egolfopoulos (University of Southern California, VS)
	prof.dr. S. Verhelst (Universiteit Gent, België)
	prof.dr. E.J.M. Hensen

purnamadah purnamidam purnat purnamudacyate
purnasya purnamadaya purnamevuvasishyate

From infinity is born infinity. When infinity is
taken out of infinity, only infinity is left over.

- Atharva Veda
1200 BC

Copyright © 2014 by M. Goswami
All rights reserved. No part of this publication may be reproduced, stored in a retrieval system, or transmitted, in any form, or by any means, electronic, mechanical, photocopying, recording, or otherwise, without prior permission of the author.

This research was financially supported by H_2-IGCC: Low Emission Gas Turbine Technology for Hydrogen-rich Syngas (FP7-ENERGY-2008-TREN-1).

Goswami, Mayuri

Laminar Burning Velocities at Elevated Pressures using the Heat Flux Method
Eindhoven University of Technology, 2014

A catalogue record is available from the Eindhoven University of Technology Library.
ISBN: 978-90-386-3564-4 Cover: M. Goswami. The illustration signifies the clean (green) emission-free nature of hydrogen flames (blue).
Publisher: BOXPress, Proefschriftmaken.nl
Typesetting in LaTeX

Subject headings: Combustion / Premixed flames / Syngas/ Hydrogen / Heat flux method / Chemical Reaction Mechanism / Thermographic Phosphor

Contents

Contents **1**

1 Introduction **5**
1.1 H_2-IGCC Project 5
1.2 Laminar Burning Velocity 7
1.3 Measurement of the Laminar Burning Velocity 9
1.4 Objective 11
1.5 Thesis Outline 12

2 Heat Flux Method **13**
2.1 Principle 13
2.2 Experimental Setup 16
2.3 Operation 18
2.4 Error Estimation 18

3 2D - Simulations at Elevated Pressures **23**
3.1 Axisymmetric Simulations 25
3.2 Computational Domain 27
3.3 Results and Discussion 30

4 High Pressure Experimental Facility **37**
4.1 High Pressure HFM-I 37
4.2 High Pressure HFM-II 40
4.3 Nitrogen Flushing System 44

5 Experimental Results: Lower Alkanes **47**
5.1 Methane 47
5.2 Ethane and Propane 60

6 Experimental Results: Syngas Mixtures (H_2/CO/N_2) **63**
6.1 Syngas Combustion 63
6.2 Experimental Results 66

6.3 General Discussion 71

7 Chemical Reaction Mechanism for Syngas Mixtures 75
7.1 Chemical Reaction Mechanism 75
7.2 Literature Review 76
7.3 Kinetic Modeling 78
7.4 Model Validation using Literature Results 89

8 Thermographic Phosphor Technique in HFM 97
8.1 Thermographic Phosphor Technique 98
8.2 Optical Setup 108
8.3 Results 114
8.4 Possible Improvements 117

9 Conclusions & Future Work 121

A Tabulated Experimental Results 125

B CHEM1D 131

Nomenclature 135

Bibliography 137

Samenvatting 149

Acknowledgements 151

Curriculum Vitae 153

Summary

With the emergence of the energy crisis in the world, alternative fuels have found great importance in the power sector. Many technologies like, for example, the Integrated Gasification Combined Cycle operates gas turbines at elevated pressures and temperatures. The ongoing technological modifications today aim at increased plant efficiency, fuel flexibility, carbon capture and storage (CCS) and managing stringent emission norms. Some of the fuels that are used today are natural gas and syngas. Combustion properties of such gases are very important for many purposes especially at practically relevant conditions (gas turbine conditions: pressure $\sim$ 30 bar, initial temperature $\sim$ 673 K and lean mixtures). This thesis is dedicated to assist in such applications. The laminar burning velocity is a combustion property of a fuel-oxidizer mixture and is a function of pressure, temperature and equivalence ratio of the mixture. This property is utilized in stability, flashback and blow-off studies for burner designs. Along with that, the laminar burning velocity is also used in validating chemical reaction mechanisms which are a necessary input to numerical simulations of combustion systems like combustion chambers (including burner) of a gas turbines.

This thesis is dedicated to the experimental and numerical investigation of syngas ($H_2/CO/N_2$) and lower alkane (C1-C3) flames at elevated pressures. One-dimensional, adiabatic, stretchless flat flames were stabilized on a heat flux method burner. Along with outlining the principle and operation of an atmospheric heat flux method (HFM) system, numerical simulations were performed in understanding the effect of pressure on the flat flame and how the geometry of a perforated burner plate used in the experiments affects the flame. In this study it was concluded that at high pressures, a lower burner plate hole diameter and high porosity of the plate creates a flat flame.

A high pressure experimental heat flux method facility was developed for performing experiments at elevated pressures. For C1-C3 alkanes, results were obtained for pressures up to 5 atm, 298 K and equivalence ratio from 0.8 to 1.4. An elaborate analysis of pressure dependence of methane - air mixture is

also included with correlations. Similar correlations are also derived for ethane - air and propane - air mixtures. Two popular chemical reaction mechanisms from literature were validated against these experimental results. Experiments were further carried out for syngas mixtures (50:50 H_2-CO, 85:15 H_2-CO and 85:15 H_2-N_2) from atmospheric pressure to 10 atm, 298 K and lean conditions (equivalence ratio up to 0.5). These experiments are novel and new in the combustion community. A chemical reaction mechanism dedicated to syngas mixtures was updated and validated with the obtained experimental results and those from literature for a wide range of pressures, temperatures and equivalence ratios. This mechanism can be utilized for future numerical studies involving gas turbine burner designs.

In addition to the study of extending the heat flux method to elevated pressure, an attempt was made to introduce an unconventional thermophosphor technique (non-intrusive) in measuring burner plate temperature to assess the accuracy of the HFM system. Conventional heat flux method experiments of methane - air mixture using thermocouples were compared to the thermophosphor experiments. The accuracy of the system with thermophosphor technique was similar to that of conventional system. However, from further analysis of the measurement procedure it was concluded that a few modifications in the optical setup can assist in improving the accuracy of the measurements.

CHAPTER 1

Introduction

From time immemorial, human civilization is relying on fuels to generate power in the form of heat and light. Beginning with just a simple wood fire to advanced power generation systems like engines and gas turbines, the face of combustion science has evolved slowly but with great potential. Studying fuels can be regarded as a very important research field especially in these times when alternative fuels have become the need of the hour. Investigation of gaseous fuels like natural gas and syngas (synthesis gas) is an interesting domain for the present combustion community. Hydrogen (H_2) is another important gas that has high potential in the present and future energy sector (power and automotive). In the current scenario, many of the combustion systems operate at elevated pressure for greater efficiency and output. The Integrated Gasification Combined Cycle (IGCC) is such a technology that utilizes gas turbines that operate at pressures as high as 30 bar. In this thesis, syngas/H_2 rich syngas mixtures and lower alkanes are investigated at elevated pressures experimentally.

1.1 H_2-IGCC Project

Renewed interest in the combustion characteristics of H_2-CO mixtures is motivated by the foreseeable increasing application of synthesis gas (syngas) in energy production and propulsion [1]. The integrated gasification combined cy-

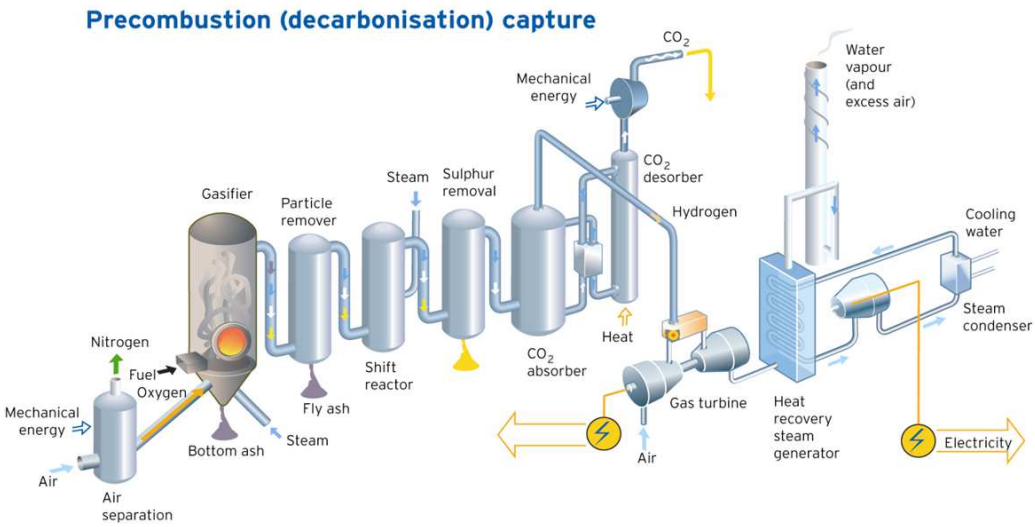

Figure 1.1. IGCC plant operation

cle (IGCC) is one of the most recent technologies that utilizes syngas to reduce NO_x emissions without compromising efficiency in power production (figure 1.1). IGCC enables the conversion of coal and biomass to a gaseous synthetic fuel gas (syngas) in the gasifier. Syngas is a mixture of hydrogen (H_2), carbon monoxide (CO), carbon dioxide (CO_2) and steam (H_2O). In combination with gasification, removal of CO_2 is possible leaving increased levels of H_2. This technology of carbon capture and storage (CCS) is considered to be very promising. Usage of high hydrogen content syngas may not only reduce the production of certain pollutants, it also increases the scope of utilizing its high energy content in the form of a fuel. Use of high H_2 fractions in combination with other gases like CO is a present trend that requires a great deal of research. Gas turbines used in such technology operate at conditions of high pressure, temperature and lean fuel-air mixtures. Hence, studying syngas combustion behavior at such conditions has become important. The H_2-IGCC project is a European Union funded project that focusses on developing a complete plant that operates on the above mentioned technology. Being a partner, TU Eindhoven was dedicated in the combustion sub-project to deliver a laminar burning velocity database of lean syngas mixtures at elevated pressure and kinetic model development.

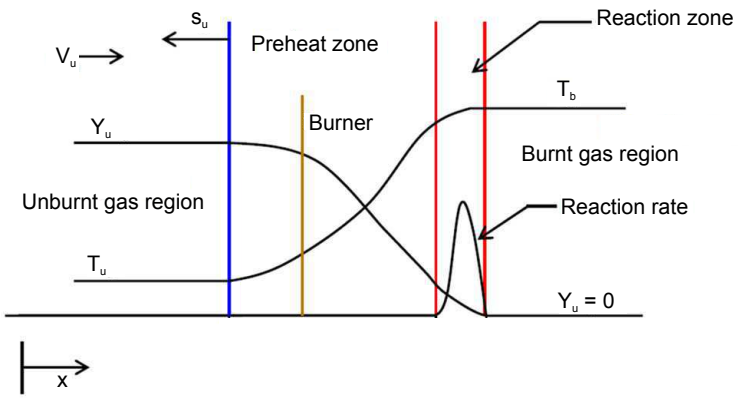

Figure 1.2. Laminar flame structure

1.2 Laminar Burning Velocity

A flame is a self-sustaining propagation of a localized combustion zone at subsonic velocities [2]. The premixed flame is obtained when the fuel and the oxidizer are completely mixed in a certain stoichiometry prior to combustion. The flame can be divided into two zones: (1) preheat zone (2) reaction zone. The chemical energy is released in the reaction zone. The reactants enter the flame with a velocity equal to the flame speed S_L. Figure 1.2 shows the structure of a typical flame which contains gradients of temperature (from T_u to T_b), species fraction (Y_u) and reaction rate from unburnt to burnt side. A necessary prerequisite to the study of turbulent flames is to understand laminar flames. The laminar burning velocity (S_L) defines the rate at which the unburnt mixture is consumed in a propagating laminar flame. This parameter is considered one of the most important entities in assessing many phenomena like flame quenching, flashback and stabilization in burners and combustors. Along with its importance in designing combustors for the systems mentioned above, this parameter also plays a key role in validating chemical reaction mechanisms. These chemical reaction mechanisms are employed in numerical simulations of practical systems (eg. turbulent flames) to analyze system behavior. In theory, S_L can be obtained when a flame is one-dimensional, adiabatic and stretchless. In case of stretched flames, experiments are performed at various stretch rates which are subsequently plotted and extrapolated to zero stretch.

The factors influencing the laminar burning velocity of a fuel-oxidizer mixture are:

- Temperature: The dependence of laminar burning velocity on temperature is studied by many researchers. Hermanns et al. [3] studied recently this behavior for methane enriched with hydrogen and used the correlation given by equation 1.1 which is used commonly in literature,

$$S_L = S_{L0} \left(\frac{T}{T_0}\right)^{\alpha_1}, \tag{1.1}$$

  where S_{L0} is the laminar burning velocity at reference conditions (usually at 1 atm), T_0 is the reference temperature and α_1 is the temperature power exponent.

- Pressure: Experimental results have shown that laminar burning velocity depends inversely on pressure. A common correlation used in literature is given by:

$$S_L = S_{L0} \left(\frac{P}{P_0}\right)^{\beta_1}, \tag{1.2}$$

  where S_{L0} is the laminar burning velocity at reference conditions (usually at 1 atm), P_0 is the reference pressure and β_1 is the pressure power exponent. Many studies have been reported in recent literature on pressure dependence [4]. Recently published study from Goswami et al. [5] outlines the pressure dependent correlations used in literature for the last few decades for methane-air mixtures. This analysis can be found in chapter 5. This thesis is also dedicated in studying the dependence of this property on pressure for syngas mixtures.

- Equivalence Ratio: The equivalence ratio of a fuel-oxidizer mixture defines the lean or rich character of the mixture. A stoichiometric mixture is defined as the fuel-oxidizer mixture that contains the exact amount of oxidizer required to convert all of the fuel into products. The equivalence ratio, ϕ is defined as:

$$\phi = \frac{(m_{\mathrm{fuel}}/m_{\mathrm{oxidizer}})_{\mathrm{actual}}}{(m_{\mathrm{fuel}}/m_{\mathrm{oxidizer}})_{\mathrm{stoichiometric}}}, \tag{1.3}$$

  where m is the mass of the reactant given by the subscripts (fuel or oxidizer). A mixture with $\phi < 1$ is called a lean mixture. If $\phi > 1$, the mixture is termed rich. The laminar burning velocity is primarily affected by the equivalence ratio as a result of how it affects the flame temperature. Therefore, it is expected that a maximum of flame speed is

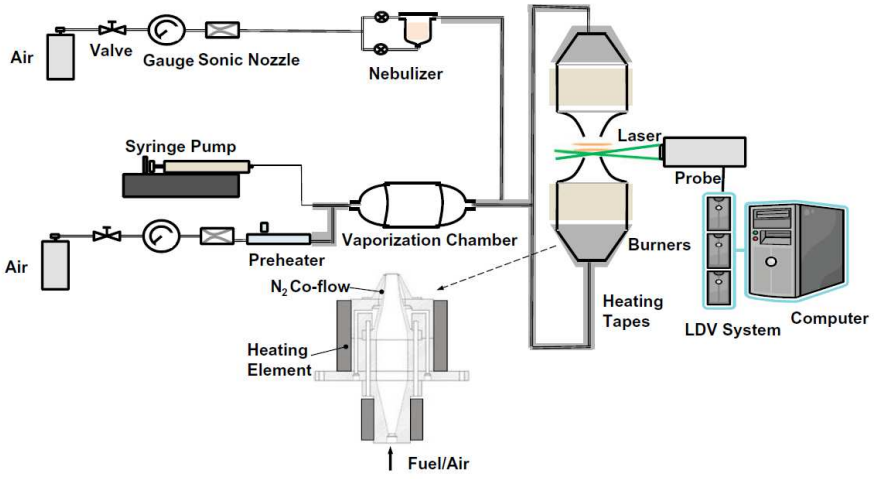

Figure 1.3. Schematic of the experimental setup used at University of Southern California [9]

obtained from a slightly rich mixture. Many studies have validated this in case of fuels like hydrocarbons [6] and syngas [7].

1.3 Measurement of the Laminar Burning Velocity

There are a number of methods that can be employed to measure the laminar burning velocity. Some of them are the counterflow flame method [6], the spherically propagating flame method [7, 4] and the conical flame method [1].

Counterflow flame method

The counterflow flame method involves establishment of two symmetrical, planar, nearly adiabatic flames in a nozzle-generated counterflow. The determination of the axial velocity profile along the centerline of the flow by using laser Doppler velocimetry, and the identification of the minimum point of the velocity profile as a reference upstream flame speed $\mathrm{S_L}$ corresponding to the imposed stretch rate K. Plotting $\mathrm{S_L}$ versus K, the laminar flame speed without stretch $\mathrm{S_L}$ can be determined through linear extrapolation to $\mathrm{K} = 0$ [8]. The flame stretch rate is, $\mathrm{K} = (1/\mathrm{A})(\mathrm{dA}/\mathrm{dt})$ where A is the area of the flame. A schematic representation of the experimental setup is given in figure 1.3.

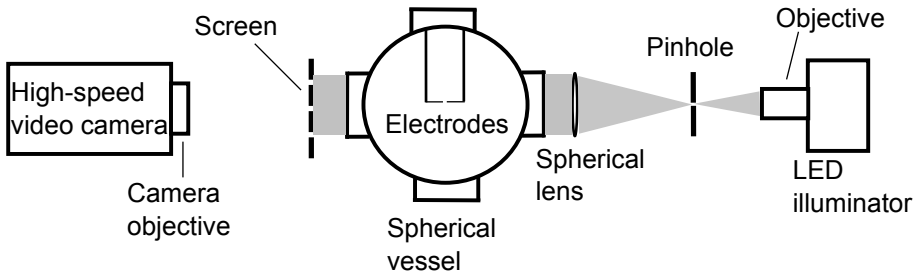

Figure 1.4. Schematic of the experimental setup used at Universite d' Orleans [11]

Spherical flame method

The experimental apparatus of the spherical flame method comprises of a spherical vessel. The vessel is filled with the fuel-oxidizer mixture using partial pressures. After the mixture is ignited via spark discharge at the center, the flame propagation is recorded visually through optical access or through measuring a pressure-time trace using a pressure sensor [10]. A schematic representation of the experimental setup is given in figure 1.4. The flame speed in this method is affected by flame movement, strain and pure curvature.

Conical flame method

A conical flame is stabilized on the rim of a cylindrical burner. This flame is not one-dimensional and is affected by strain and curvature. The effect of such strain on the flame speed depends on the Markstein length of the mixture. The average flame speed is calculated by dividing the volume flow rate of the mixture by the luminous cone surface area. It is given by $\mathrm{S_L} = \mathrm{v_u} \cdot \mathrm{sin}\alpha$ where $\mathrm{v_u}$ is the velocity of the unburnt gas mixture, α is the half cone angle. A schematic representation of the experimental setup is given in figure 1.5,

Heat flux method

The heat flux method (HFM) originated in TU Eindhoven two decades ago. The publication of Powlings [12] and Botha and Spalding [13] were the first step towards flat flame method. The heat flux method was introduced by de Goey et al. [14] in 1993. Since then, many researchers [15, 16, 17, 18, 5] have worked towards improving the method and generating burning velocity data for a variety of fuels. The method [16] has proven to be accurate for measuring $\mathrm{S_L}$ since it creates a flame very close to the one-dimensional, adiabatic and stretchless state. The main principle of the heat flux method is the stabilization of a flat flame with an unburnt gas velocity such that the heat loss by the flame needed

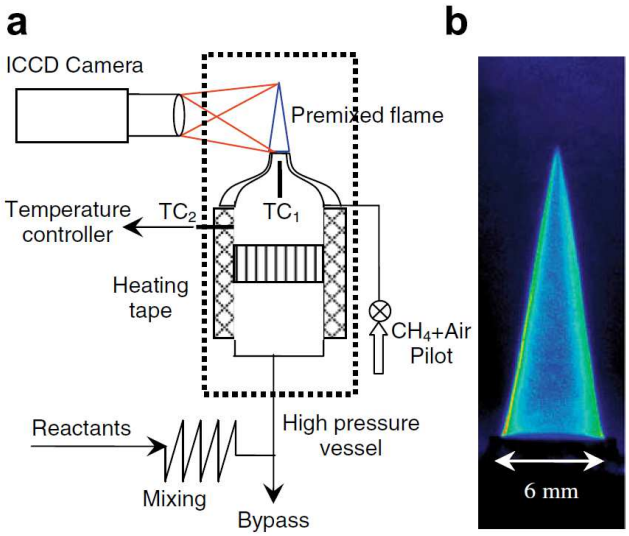

Figure 1.5. (a) Schematic of the experimental setup (TC = thermocouple) used at Georgia Institute of Technology [1]. Mixing is achieved through long flow lines. (b) Typical image of flame emission from OH* and CO_2* (80:20 H_2/CO fuel mixture, 10:90 O_2:He oxidizer, 15 atm and 600 K unburnt gas temperature).

to stabilize it on the burner is compensated by the heat added to the unburnt gases. This differential heat flux is reflected in the burner plate temperature profile that specifies the adiabatic state of the flame. This method is used in the present work. The temperature measurements in this technique is done through thermocouples.

1.4 Objective

The essence of this thesis is to analyze laminar flames at elevated pressures. The objectives of this thesis are to:

- Gain insight into heat flux method at elevated pressure and numerically analyze the effect of pressure.
- Experimentally determine laminar burning velocity of syngas mixtures and lower alkanes (C1-C3) at elevated pressures using heat flux method.
- Propose and validate a chemical reaction mechanism for syngas mixtures with experimental results.

- Introduce an alternative temperature measurement (non-intrusive) technique using thermophosphors in HFM measurements and check its feasibility.

1.5 Thesis Outline

The following chapter discusses the principle and working of the experimental technique 'heat flux method' used in this work. The description outlines the experimental setup, operation of the HFM burner (without elevated pressure conditions), the procedure to determine S_L and the errors involved in the technique. Chapter 3 is dedicated to a numerical analysis of flat flames at elevated pressure and investigate the dependence of burner plate dimensions on the flatness of the flame. Chapter 4 introduces the high pressure facility developed that houses the HFM burner. This facility was utilized in generating S_L data at high pressure. The experimental results for lower alkanes (C1-C3) and syngas mixtures are discussed in chapter 5 and 6. The development and validation of a chemical reaction mechanism for syngas mixtures is discussed in chapter 7. The predicted values of the laminar burning velocity were obtained by using the in-house laminar flame code CHEM1D [19]. An attempt to introduce the non-intrusive technique of thermophosphor to heat flux method for temperature measurement is discussed in chapter 8. The conclusions from this thesis and the future scope of work are outlined in chapter 9.

CHAPTER 2

Heat Flux Method

The experimental tool used in this thesis is the heat flux method (HFM). As introduced in the previous chapter, this method is relatively new when compared to other methods in determining laminar burning velocity of fuels. This method has been used widely for measurements at atmospheric pressure. This chapter is dedicated to the operation and understanding of this method. Therefore, the explanations in this chapter are for the basic (atmospheric) setup. The additions to the basic HFM setup for high pressure operations are outlined in chapter 4. For more details on HFM, the published study of Bosschaart and de Goey [16] can be referred which gives a detailed account of the principle, operation and error analysis of the heat flux method.

2.1 Principle

The burner used in the heat flux method houses a burner plate that consists of small holes. The cross section of a very small part of the burner plate (3 holes) is shown in figure 2.1. The streamlines of the gas flow are depicted through the left most hole. The arrows shown in the right most hole indicate the heat balance. The horizontal arrows show heat gain from the burner plate to the unburnt gas mixture, while the vertical arrows indicate the heat loss from the flame to the burner plate. The net difference between the heat loss and the heat gain

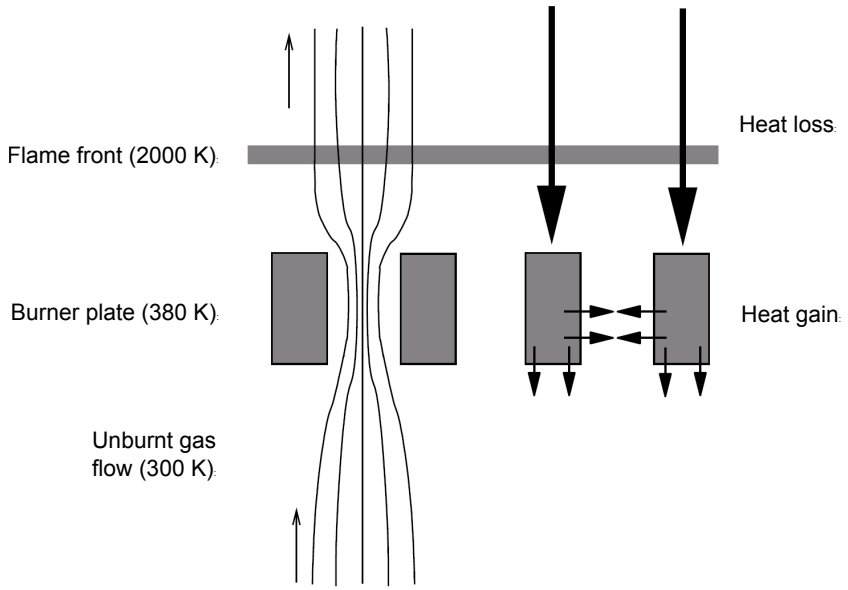

Figure 2.1. Schematic of the heat flux between the unburnt gas, flame and burner plate.

(summed over the burner plate) is responsible for the temperature distribution over the burner plate. This can be observed from the eight thermocouples attached to the plate. The flame can be considered adiabatic when the heat loss equals the heat gain. This will result in a constant temperature distribution over the plate. When the unburnt gas velocity is higher than the laminar burning velocity (super-adiabatic) the heat gain by the gas is larger than the heat loss from the flame. The situation is opposite in case of a sub-adiabatic flame. The radial profile of temperature on the burner plate close to the adiabatic burning velocity is fitted by the method of least squares to a parabolic profile explained in the next section.

Energy Equation

In this section, the heat flux balance of the burner plate is visualized analytically. The energy equation of the burner plate in cylindrical coordinates, assuming rotational symmetry can be written as,

$$-\frac{\partial}{\partial \mathrm{x}}\left[\lambda_{\mathrm{p,x}}(\mathrm{r})\frac{\partial \mathrm{T_p(x,r)}}{\partial \mathrm{x}}\right]-\frac{1}{\mathrm{r}}\frac{\partial}{\partial \mathrm{r}}\left[\lambda_{\mathrm{p,r}}(\mathrm{r})\mathrm{r}\frac{\partial \mathrm{T_p(x,r)}}{\partial \mathrm{r}}\right]=\alpha_{\mathrm{gb}}(\mathrm{x})\left[\mathrm{T_g(x,r)}-\mathrm{T_p(x,r)}\right], \tag{2.1}$$

where $\mathrm{T_p}$ is the temperature of the burner plate, $\mathrm{T_g}$ is the temperature of the gas, $\lambda_{\mathrm{p,x}}$ is the thermal conductivity of the burner plate in axial direction x, and $\lambda_{\mathrm{p,r}}$ is the thermal conductivity of the burner plate in radial direction r. α_{gb} is the volumetric heat transfer coefficient between the gas and the burner plate. Due to the perforation pattern in the plate, the thermal conductivities in radial and axial direction differ from each other. The above equation is integrated over the plate thickness from $\mathrm{x} = 0$ to $\mathrm{x} = \mathrm{h}$,

$$\begin{aligned} -\frac{1}{\mathrm{r}}\frac{\partial}{\partial \mathrm{r}}\left[\lambda_{\mathrm{p,r}}(\mathrm{r})\mathrm{r}\frac{\partial}{\partial \mathrm{r}}\int_0^{\mathrm{h}} \mathrm{T_p}(\mathrm{x},\mathrm{r})\mathrm{dx}\right] &= \int_0^{\mathrm{h}} \alpha_{\mathrm{gb}}(\mathrm{x})\left[\mathrm{T_g}(\mathrm{x},\mathrm{r}) - \mathrm{T_p}(\mathrm{x},\mathrm{r})\right]\mathrm{dx} \\ &+\lambda_{\mathrm{p,x}}\frac{\partial \mathrm{T_p}}{\partial \mathrm{x}}\Big|_{\mathrm{x}=\mathrm{h}} - \lambda_{\mathrm{p,x}}\frac{\partial \mathrm{T_p}}{\partial \mathrm{x}}\Big|_{\mathrm{x}=0} = \mathrm{q}(\mathrm{r}), \end{aligned} \tag{2.2}$$

with $\mathrm{q}(\mathrm{r})$ the net heat transfer from the gas to the burner plate. The average plate temperature can now be defined as:

$$\overline{\mathrm{T}}_{\mathrm{p}}(\mathrm{r}) = \frac{1}{\mathrm{h}}\int_0^{\mathrm{h}} \mathrm{T_p}(\mathrm{x},\mathrm{r})\mathrm{dx} \tag{2.3}$$

This can be combined with equation 2.2, resulting in:

$$-\frac{1}{\mathrm{r}}\frac{\mathrm{d}}{\mathrm{dr}}\left[\lambda_{\mathrm{p,r}}(\mathrm{r})\mathrm{r}\frac{\mathrm{d}\overline{\mathrm{T}}_{\mathrm{p}}(\mathrm{r})}{\mathrm{dr}}\right] = \frac{\mathrm{q}(\mathrm{r})}{\mathrm{h}} \tag{2.4}$$

Assuming that the conduction coefficient $\lambda_{\mathrm{p,r}}$ does not depend on temperature and therefore not on r, equation 2.4 can be solved as:

$$\overline{\mathrm{T}}_{\mathrm{p}}(\mathrm{r}) = \mathrm{T}_{\mathrm{center}} - \frac{\mathrm{q}}{4\lambda\mathrm{h}}\mathrm{r}^2 \tag{2.5}$$

The parabolic coefficient γ can now be introduced as:

$$\gamma = -\frac{\mathrm{q}}{4\lambda\mathrm{h}}, \tag{2.6}$$

This results in the simplified equation for the temperature profile over the burner plate:

$$\overline{\mathrm{T}}_{\mathrm{p}}(\mathrm{r}) = \mathrm{T}_{\mathrm{center}} + \gamma\mathrm{r}^2 \tag{2.7}$$

Equation 2.7 shows that the temperature distribution over the burner plate has a parabolic shape and the gradient in temperature depends on the last term in the equation. Analysis of Bosschaart [20] showed that the heat conductivity of brass can be assumed to be constant (independent of the temperature) in practical conditions and the parabolic coefficient γ, therefore only depends on the net heat transfer q.

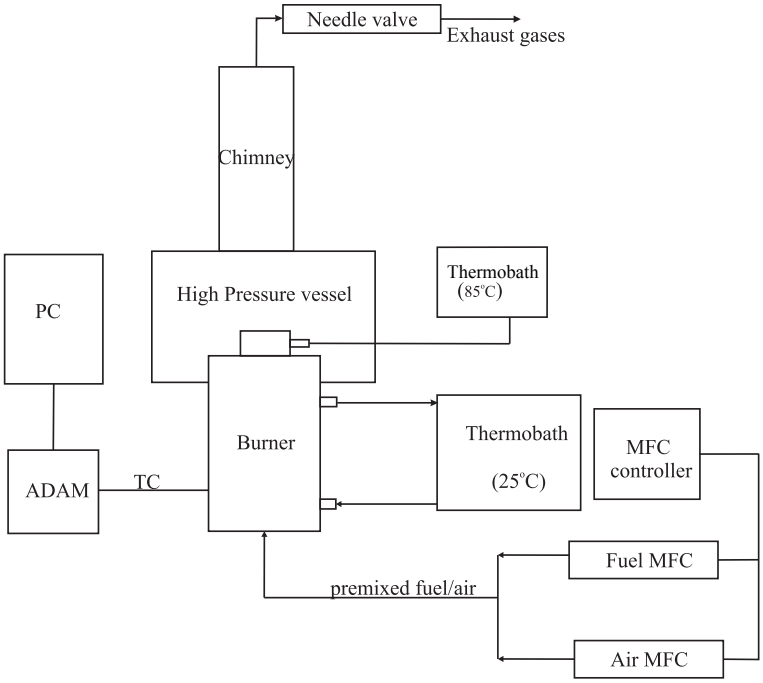

Figure 2.2. Schematic of the experimental setup

2.2 Experimental Setup

A schematic representation of the experimental setup is shown in figure 2.2. The heat flux method burner, shown in figure 2.3, consists of two parts; the plenum chamber (bottom) and the burner head (top). These parts are made out of brass and can safely be used up to 10 bar. Their goal is to create a uniform flow towards the burner plate, which is placed on top of the burner head. The inlet for the premixed fuel/oxidizer is placed on the bottom of the plenum chamber. A perforated plate is placed inside at 15 mm from the bottom, which is used as a flow straightener. The holes in this plate have a diameter of 2 mm and a pitch of 4 mm. The plenum chamber is cooled to 25 °C by water owing through a jacket in the wall. This is done to ensure that the temperature of the incoming gas mixture stays constant at $25°$C, before it reaches the heated burner head. The inlet and outlet of the water jacket are connected to a water bath which controls the temperature of the water. The unburned mixture needs to be heated by the burner plate to compensate for the heat loss of the flame towards the plate. The burner plate is kept at a constant temperature of 85 °C, which is 60 °C higher than the mixture. This is done by an electrical microtubular heating element wrapped around the top

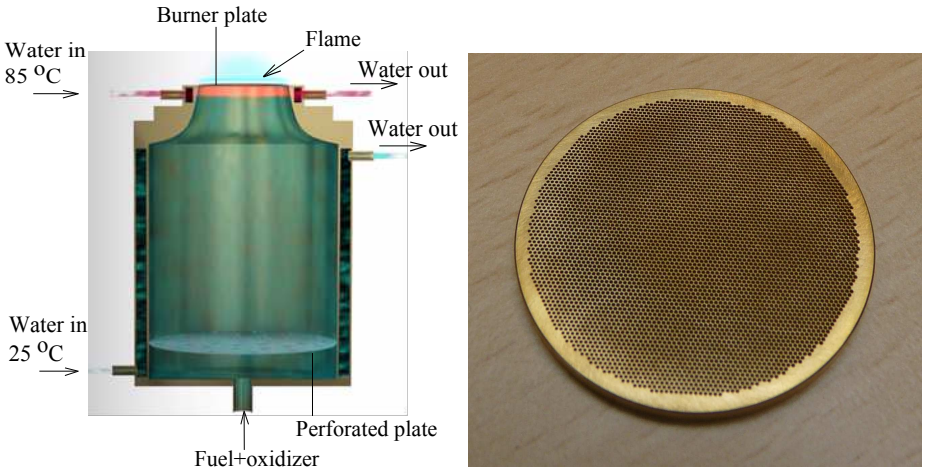

Figure 2.3. Burner and burner plate

of the burner head. When this temperature difference is decreased below 30 °C the flame blows off, whereas an increase will move the flame closer to the burner plate. A type J thermocouple is built in to monitor the temperature of the heating element. To insulate the hot top part of the burner head from the rest of the burner, a PEEK (high grade polymer material) ring is placed below the heated part. The burner is housed in a high pressure vessel, with a teflon ring in between them for thermal insulation. On both sides of the teflon ring, O-rings are used to make the connection leak tight. The 1 mm thick perforated burner plate has holes of 0.3 mm diameter and 0.4 mm pitch drilled in a hexagonal pattern. The plate itself has a diameter of 30 mm. Eight Copper-Constantan thermocouples (type T) are attached at following radius (mm) - angle (°) positions on the plate from the centre: 0 (0°), 2.8 (330°), 4.9 (150°), 7.7 (270°), 9.1 (30°), 10.5 (90°), 12.6 (210°), 14.7 (330°).

Gas Flow Control

The gas flow board consists of individual mass flow controllers (MFC) for fuel and oxidizer. A cylindrical buffer vessel is placed before each MFC to damp pressure variations from the supply. Filters are also installed just before the MFC to avoid contamination. The MFCs are connected to the computer via an RS232 serial line and communicates through Bronkhorst program. The total volume flow rate (l/min) $\mathrm{Q_t}$ is given by,

$$\mathrm{Q_t} = \mathrm{U_g} \cdot \mathrm{A} \cdot 60 \cdot 1000 \tag{2.8}$$

$\mathrm{U_g}$ is the unburnt gas velocity, A is the cross section area of the inlet. The

capacity (calibrated) of MFCs for methane, H_2-CO and oxidizer (O_2/N_2 or O_2/He) are 5 ln/min, 20 ln/min and 160 ln/min respectively where ln/min denotes litre normal per minute (reference conditions are 0 $^\circ$ and 1.013 bar [21]). The volume flow rate fraction of fuel and oxidizer is calculated based on equation 2.8. The entire gas flow control system is built to handle higher pressure by using Swagelok couplings, valves and connections. Copper and stainless steel pipelines are installed to ensure smooth high pressure operations. The gas lines that handle CO flow are specifically made of copper and brass components. CO often reacts slowly with Ferrous and Nickel containing lines/components resulting in changed gas composition which might ultimately affect the flame [22].

2.3 Operation

When the unburnt gas velocity is higher than the laminar burning velocity (super-adiabatic) the heat gain by the gas is larger than the heat loss from the flame. The situation is opposite in case of a sub-adiabatic flame. The only measurement required in this technique is the temperature profile of the burner plate. The radial profile of temperature on the burner plate close to the laminar burning velocity is fitted by the method of least squares to a parabolic profile given by equation 2.7. γ is the parabolic coefficient and accounts for the net heat flux between the unburnt gas, plate and the flame.

The coefficients of such polynomials are plotted against gas flow velocities. The adiabatic state is reached for zero value of the parabolic coefficient γ. Figure 2.4 (left) shows the temperature profiles obtained at different gas velocities for a methane-air flame at $\phi = 0.9$ and 3 atm and 298 K. The sub-adiabatic flame is represented by convex profiles and super-adiabatic flames by concave profiles. The laminar burning velocity is interpolated from the plot in figure 2.4 (right) for $\gamma = 0$. The thermocouples attached to the burner plate must ideally be fixed on the same height in the holes. But practically, due to the height variation, a small systematic error may sweep in which can deviate temperature measurement by more than $\pm$ 1 K. In such cases, a correction of this error is done by first calculating the parabolic coefficient. According to the deviation experienced, the measured temperatures are adapted to find the corrected temperature.

2.4 Error Estimation

This section is dedicated to estimation of errors involved in a standard heat flux method measurement. The flow rates in the system are regulated by mass

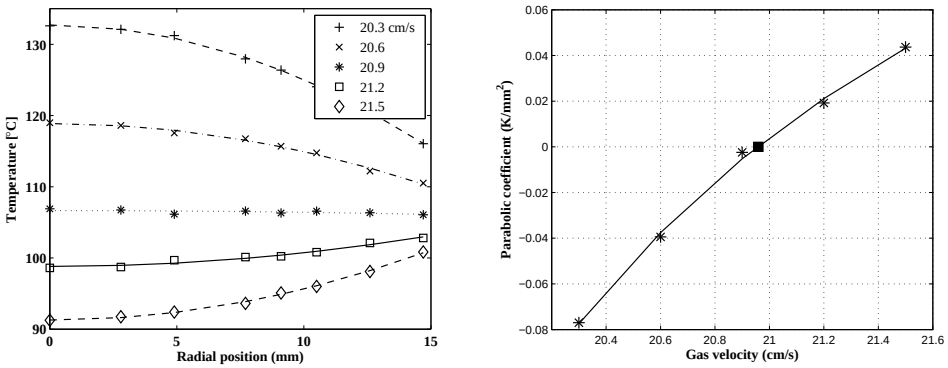

Figure 2.4. (Left) Corrected thermocouple temperature profiles at different gas velocities for methane-air flame at 3 atm, $\phi = 0.9$ and unburnt gas temperature 298 K. The profiles are corrected for the systematic errors due to difference in thermocouple attachment position. (Right) Parabolic coefficients of profiles are plotted with gas velocities. Laminar burning velocity is deduced by interpolating velocity at γ=0 (denoted by black square).

flow controllers (MFC) fabricated by Bronkhorst High-Tech [21]. The error in the controller operations are high when the flow rates are less than 10% of the full scale. This decreases to almost $\pm$1% for higher flows. The MFCs were calibrated regularly using the calibration setup described by [20]. The uncertainty of the MFCs is defined by equation 2.9.

$$\Delta \mathrm{m}' = 0.8\%\mathrm{Reading}{+}0.2\%\mathrm{Fullscale} \tag{2.9}$$

The error in equivalence ratio can be estimated by using partial derivatives of the equivalence ratio as a function of mass flows since ϕ is a function of flow rates. The relative error in ϕ is given by the sum of relative errors of flows:

$$\frac{\Delta\phi}{\phi} = \sum_{\mathrm{i1}}^{\mathrm{N_{MFC}}} \left|\frac{\Delta \mathrm{m_i'}}{\mathrm{m_i'}}\right| \tag{2.10}$$

Relative error in the gas velocity is a summation of errors from unburnt gas temperature, chamber pressure, area and the mass flow rates (from MFCs). A straight forward analysis using partial derivatives of the gas velocity as a function of the conditions and the mass flows. Hence, the error is given by the equation 2.11.

$$\frac{\Delta \mathrm{U_g}}{\mathrm{U_g}} = \left|\frac{\Delta \mathrm{T}}{\mathrm{T}}\right| + \left|\frac{\Delta \mathrm{p}}{\mathrm{p}}\right| + \left|\frac{\Delta \mathrm{A}}{\mathrm{A}}\right| + \sum_{\mathrm{i1}}^{\mathrm{N_{MFC}}} \left|\frac{\Delta \mathrm{m_i'}}{\mathrm{m_i'}}\right| \tag{2.11}$$

The main measurement quantity in HFM is the burner plate temperature using thermocouples. In the previous section, the systematic error emerging from thermocouple height is resolved. The remaining fluctuations in the thermocouple readings which influence the burning velocity is addressed in this section. The radial profile of temperature on the burner plate close to the laminar burning velocity is fitted by the method of least squares to a parabolic profile given by equation 2.7 where γ is the parabolic coefficient and accounts for the net heat flux between the unburnt gas, plate and the flame. The sensitivity, s indicating the variation of the parabolic coefficient γ with change in gas velocity is given by,

$$\mathrm{s} = \frac{\mathrm{d}\gamma}{\mathrm{dU_g}}|_{\gamma\,=\,0} \tag{2.12}$$

Sensitivity, s can be calculated from figure 2.4 (right). By taking standard deviations from the residues of the parabola fits, error from temperature readings can be calculated. Therefore, uncertainty in the parabolic coefficient is given by,

$$\sigma_\gamma = \frac{2\sigma_{\mathrm{tc}}}{\mathrm{r_b^2}} \tag{2.13}$$

Error in measured laminar burning velocity $\mathrm{S_L}$ due to the remaining scatter in the thermocouple measurements is,

$$\sigma_{\mathrm{S_L}} = \frac{1}{\mathrm{s}}.\frac{2\sigma_{\mathrm{tc}}}{\mathrm{r_b^2}} \tag{2.14}$$

The position of the thermocouple on the edge of the burner plate, $\mathrm{r_b}$ is 14.7 mm in case of a 30 mm plate and 9.8 mm for a 20 mm plate. The resulting total error in burning velocity is mentioned in chapter 5 and 6 for high pressure measurements and are listed in appendix A for each experiment performed during this study.

Summary

The principle, operation and error analysis of the heat flux method are discussed. In this technique a near adiabatic flame is stabilized by balancing the heat loss from the flame to the burner with heat gain to the unburnt gas mixture such that no net heat loss to the burner is observed. When the unburnt gas velocity is higher than the laminar burning velocity (super-adiabatic) the heat gain by the gas is larger than the heat loss from the flame. The situation is opposite in case of a sub-adiabatic flame. The only measurement required in this technique is the temperature profile of the burner plate. The radial profile of temperature

on the burner plate close to the laminar burning velocity is fitted by the method of least squares to a parabolic profile. The profile accounts for the net heat flux between the unburnt gas, plate and the flame.

CHAPTER 3

2D - Simulations at Elevated Pressures

The main feature of the heat flux method is that the heat loss from the flame is compensated by adding heat to the unburnt gas mixture. A perforated plate is fitted on a burner head which is maintained at a temperature higher than the unburnt gas temperature. This gives a heat transport from the burner head to the burner plate and finally to the unburnt gas mixture. The temperature profile obtained from the perforated burner plate determines whether a flame is adiabatic or not. The burner plate creates a pressure drop in the flow and damps out any fluctuation downstream. Therefore, the plate plays an important role in stabilizing a flat flame. The numerical simulations performed by de Goey et al. [23] showed that methane-air flame experienced small curvature with inlet velocity higher than 40 cm/s with a burner plate having hole diameter $(\mathrm{d}) = 0.5$ mm and pitch $(\mathrm{s}') = 0.7$ mm. This was done at atmospheric pressure. Other simulations [19] showed that a decrease in hole diameter can reduce the flame curvature. It was also showed that very small porosity (χ) will lead to early blow off due to high velocity in the holes. The relationship between porosity (χ) and pitch (s') is described in subsequent section.[1]

[1] *The results shown in this chapter have been published by Goswami et al. Combustion Science and Technology (Accepted) (2014)*

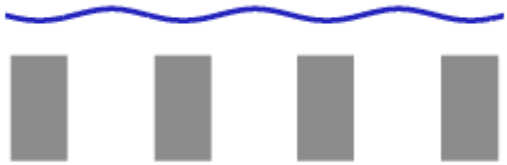

Figure 3.1. Schematic of flame curvature above the burner plate.

Under conditions of elevated pressure, if the upstream flow fluctuations are not damped in time, the flame may show curvature due to distortion in heat and mass transport as shown in figure 3.1 that depicts the cross section of a burner plate. The rectangular part represents the plate with holes between them. These curvature effects may not be visible to the naked eye. The increase in surface area may hence, influence the burning velocity measured at elevated pressure. Therefore, the objective of the present study is to focus on the question if the flatness of stoichiometric methane (CH_4)-air flames obtained from different burner plate designs or models depends on the plate hole diameter and distance between successive holes. In order to assess how a flat (heat flux method) flame behaves in a high pressure environment, two-dimensional axisymmetric simulations have been performed on three burner plate models. The first model is with $\mathrm{d} = 0.5$ mm and $\chi = 0.63$. The second burner plate model has a reduced diameter of $\mathrm{d} = 0.3$ mm but similar porosity $\chi = 0.63$. Finally, the third burner plate model which is also used in high pressure experiments [5] is with $\mathrm{d} = 0.3$ mm and reduced porosity $\chi = 0.51$. The three models are summarized in table 3.1.

Table 3.1. Dimensions of the burner plate models

Model	Hole diameter (mm)	Porosity χ (-)	Pitch s' (mm)
1	0.5	0.63	0.6
2	0.3	0.63	0.36
3	0.3	0.51	0.4

3.1 Axisymmetric Simulations

The 2-dimensional axisymmetric simulations are performed for a stoichiometric methane-air mixture with an unburnt gas temperature of 300 K using the commercially available CFD code Fluent [24]. Steady state simulations with an incompressible flow and a one-step kinetic mechanism are performed up to 7 bar. Earlier studies [23] present a comparison of a one-step mechanism with the skeletal mechanism, introduced by Smooke [25]. The results showed only small differences in the calculated temperature profile, which is used to determine the flame curvature. Therefore, it was concluded that the one-step mechanism is well suited to predict the flame shape and curvature effects [23]. Detailed simulations using the DRM19 mechanism [26] are also performed up to 15 bar, with model 3 that resembles the burner plate from the experimental setup.

Governing Equations

The combustion of gases is governed by a set of equations describing the conservation of mass, momentum, energy and species. The equations are given by

$$\frac{\partial \rho}{\partial \mathrm{t}} + \nabla \cdot (\rho \vec{\mathrm{v}}) = 0, \tag{3.1}$$

$$\frac{\partial}{\partial \mathrm{t}}(\rho \vec{\mathrm{v}}) + \nabla \cdot (\rho \vec{\mathrm{v}} \vec{\mathrm{v}}) = -\nabla \mathrm{p} + \nabla \cdot (\overline{\overline{\tau}}) + \rho \vec{\mathrm{g}} + \vec{\mathrm{F}}, \tag{3.2}$$

$$\nabla \cdot (\vec{\mathrm{v}}(\rho \mathrm{E} + \mathrm{p})) = \nabla \cdot (\mathrm{k} \nabla \mathrm{T} - \sum_{\mathrm{i}} \mathrm{h_i} \vec{\mathrm{J}_\mathrm{i}} + (\overline{\overline{\tau}} \cdot \vec{\mathrm{v}})) + \mathrm{S_h}, \tag{3.3}$$

where v is the gas mixture velocity and ρ the density, p is the static pressure, $\overline{\overline{\tau}}$ is the stress tensor, and $\rho\vec{\mathrm{g}}$ and $\vec{\mathrm{F}}$ are the gravitational body force and external body forces. k is the thermal conductivity and $\vec{\mathrm{J}_\mathrm{i}}$ is the diffusion flux of species. The first three terms on the right-hand side of equation 3.3 represent energy transfer due to conduction, species diffusion and viscous dissipation respectively. $\mathrm{S_h}$ is the source term which includes the heat of chemical reaction for reactive flows. The total specific energy $\mathrm{E} = \mathrm{h} - \frac{\mathrm{p}}{\rho} + \frac{\mathrm{v}^2}{2}$, where sensible enthalpy h is defined for ideal gases as $\sum_\mathrm{i} \mathrm{Y_i h_i}$, with $\mathrm{Y_i}$ the mass fraction of species i and $\mathrm{h_i} = \int_{\mathrm{T_{ref}}}^{\mathrm{T}} \mathrm{c_{p,i}}\,\mathrm{dT}$ where $\mathrm{T_{ref}}$ is 298.15 K. The source term $\mathrm{S_h}$ is essentially the energy produced due to chemical reaction which is given by $\mathrm{S_h} = -\sum_\mathrm{i} \frac{\mathrm{h_i^0}}{\mathrm{M_i}} \mathrm{R_i}$ where $\mathrm{h_i^0}$ is the enthalpy of formation of species and $\mathrm{R_i}$ is the volumetric rate of creation of species i.

For solving conservation equations for chemical species, the solver predicts the local mass fraction of each species, $\mathrm{Y_i}$, through the solution of a convection-diffusion equation for the $\mathrm{i_{th}}$ species. This species conservation equation has the general form

$$\frac{\partial}{\partial \mathrm{t}}(\rho \mathrm{Y_i}) + \nabla \cdot (\rho \vec{\mathrm{v}} \mathrm{Y_i}) = -\nabla \cdot \vec{\mathrm{J_i}} + \mathrm{R_i}, \tag{3.4}$$

where $\mathrm{R_i}$ is the net rate of production of species i by chemical reaction. Equation 3.4 needs to be solved for $\mathrm{N_s} - 1$ species (where $\mathrm{N_s}$ is the total number of species) since the mass fraction of one of the species can be solved using the constraint that the sum of all the species mass fractions equals 1. To minimize the numerical error, the species that is present in abundance is chosen for this purpose. In case of methane-air mixture it is nitrogen. The chemical source terms are computed in Fluent by the laminar finite-rate model using Arrhenius expressions from the reaction mechanism file. The net source of chemical species due to reaction, $\mathrm{R_i}$, is computed as the sum of the Arrhenius reaction sources over the reactions that the species participate in.

$$\mathrm{R_i} = \mathrm{M_{w,i}} \sum_{\mathrm{r}=1}^{\mathrm{N_R}} \widehat{\mathrm{R}}_{\mathrm{i,r}}, \tag{3.5}$$

where $\mathrm{M_{w,i}}$ is the molecular weight of species i and $\widehat{\mathrm{R}}_{\mathrm{i,r}}$ is the Arrhenius molar rate of creation or destruction of species i in reaction r. The stiff laminar flames are modeled with the laminar finite-rate model using the pressure-based solver. For steady simulations, this option approximates the reaction rate $\mathrm{R_i}$ in the species transport equation 3.4 as,

$$\mathrm{R_i^*} = \frac{1}{\tau} \int_0^{\tau} \mathrm{R_i}\, \mathrm{dt}, \tag{3.6}$$

where τ is a time step, with the default value set to one-tenth of the minimum convective or diffusive time-scale in the cell.

The solver uses a control-volume-based technique to convert the governing equations to algebraic equations that can be solved numerically. The second order upwind scheme is used for spatial discretization of all the governing equations. The pressure-based coupled algorithm is used to enable full pressure-velocity coupling. This algorithm solves the momentum and pressure based continuity equations together, which improves the rate of solution convergence when compared to the segregated algorithm. The standard pressure interpolation scheme is used to interpolate the pressure values at the faces. The double-precision solver is utilized for solving the discretized set of algebraic equations. To obtain a converged solution, a two-step solution process was adopted. First,

the flow, energy and species equations were solved with the reactions disabled. This cold flow solution was obtained within 1000 iterations and provided a good starting point for the combustion problem. With the basic flow pattern now established, the second step was to enable the reactions and ignite the mixture. The density ρ, of the multicomponent mixture is calculated using the ideal gas law for an incompressible flow. The viscosity μ, and the thermal conductivity, k, for the individual species are computed using the kinetic theory. These two properties of the mixture are calculated with the ideal gas mixing law, which is allowed when the ideal gas law is used for the density. The inputs to the calculation of viscosity, thermal conductivity, specific heat and mass diffusion coefficient of individual species are taken from the chemical reaction mechanism which includes thermodynamic and transport properties of the species. The Soret effect is taken into consideration in computing the diffusion flux.

3.2 Computational Domain

The three burner plate models investigated in this work are described in table 3.1. The burner plate used in experiments is a round perforated plate with a diameter of 30 mm and a thickness of 1 mm (model 3). The holes have a diameter of $\mathrm{d} = 0.3$ mm and a pitch of $\mathrm{s}' = 0.4$ mm. They are placed in a hexagonal pattern in order to stabilize a flat flame above the burner plate. The actual plate has over 5000 holes, but a schematic representation is shown in figure 3.2. The presence of symmetry planes can be used to isolate a small hexagonal unit cell, this unit cell is approximated by an axisymmetrical cell. The red rectangle represents the plane that needs to be modeled, with the axis of rotation through the center of a hole. The round edge of the cell is modeled as a symmetry boundary. The right side of figure 3.2 shows that when the actual pitch, s', is used in the model, there will be parts of the burner plate that are not taken into account. This will lead to a different porosity than the actual plate. To compensate for this, the pitch, s is now chosen such that the porosity of the axisymmetrical cell (axi) is equal to the porosity of the hexagonal unit cell (hex).

$$\chi_{\mathrm{axi}} = \left(\frac{\mathrm{d}}{\mathrm{s}}\right)^2 \tag{3.7}$$

$$\chi_{\mathrm{hex}} = \left(\frac{\pi}{2\sqrt{3}}\right)\left(\frac{\mathrm{d}}{\mathrm{s}'}\right)^2 \tag{3.8}$$

The axisymmetric axis is defined along the x-axis and goes through the center of a hole. The round edge of the domain is modeled as a symmetry boundary

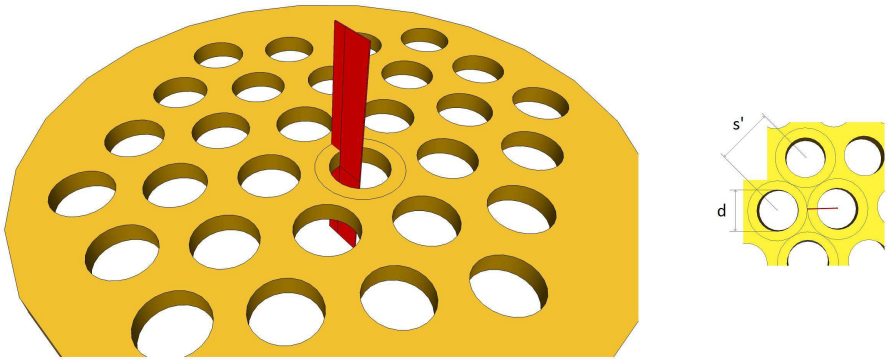

Figure 3.2. Burner plate with hexagonal pattern for holes. Red plane is the computational domain which is rotated along the axis through the center of the hole.

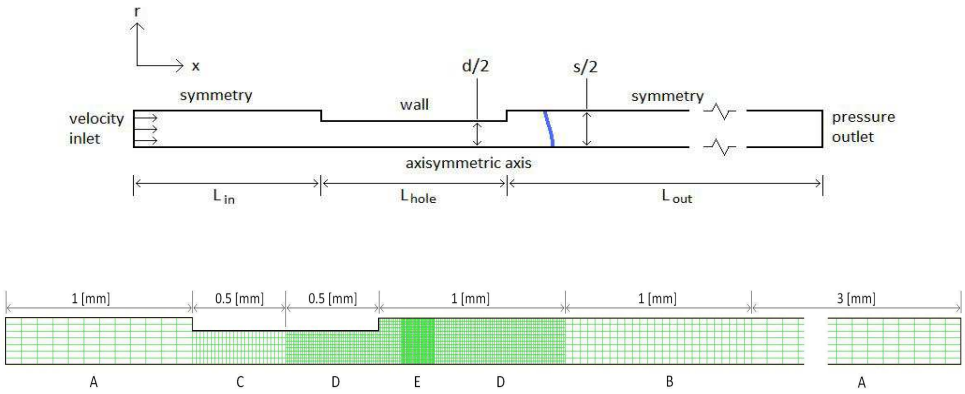

Figure 3.3. Schematic of the computational domain and mesh for the axisymmetric model.

and the burner plate as a wall. The in-flow of the premixed gases is defined as a velocity inlet, where the velocity magnitude and the species mass fractions are defined. The blue line in figure 3.3 (top) represents the approximate position of the flat flame. The exhaust gases leave through the pressure outlet, which is placed sufficiently far from the flame. The length of the computational domain is determined by: the length of the in-flow area $\mathrm{L_{in}}$, the thickness of the burner plate $\mathrm{L_{hole}}$ and the length of the flame/outflow area $\mathrm{L_{out}}$. Typical dimensions are 1, 1 and 5 mm respectively. The computational grids were made in Gambit 2.4.6, which is Fluent's preprocessor for creating the geometry and the mesh. The grid is shown in figure 3.3 (bottom). The grid consists of several sections, labeled A to E, with an increasing level of refinement. Initially, section E has

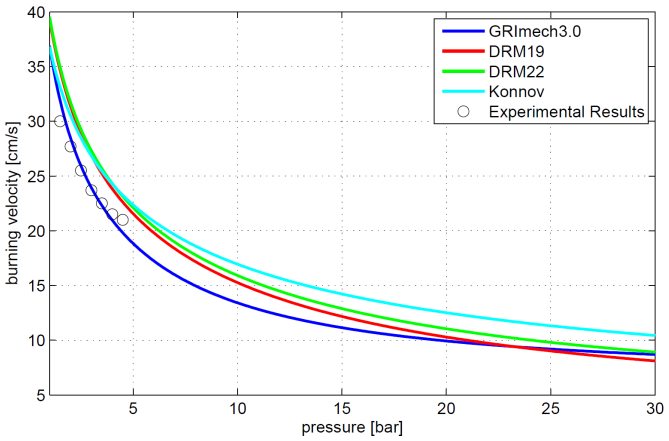

Figure 3.4. Dependence of laminar burning velocity of stoichiometric methane/air mixture on pressure. Experimental results [5] are compared with 1-D numerical simulations using various kinetic models [27, 26, 28]

the same cell dimensions as section D. For several cases, the whole grid was refined in Fluent after the solution was converged. This was done by adaptation of the grid, which creates 4 cells out of one. The solution was then converged again to check that it remains the same. This would show that the used cell dimensions provide a grid independent solution. It was found that the chosen cell dimensions for the grids used in this work are small enough. For all the simulations, the grid was refined in the flame region from D to E, after the solution was converged. The largest gradients occur in this region, so the refinement was used to check that the solution remains grid independent for all cases.

Chemical Reaction Mechanism

In order to perform the detailed simulations, an appropriate chemical reaction mechanism has to be selected. One-dimensional simulations were performed with stoichiometric methane-air flames using four different chemical reaction mechanisms. The pressure was increased from 1 to 30 bar. An overview of the calculated laminar burning velocities, together with the experimental results is presented in figure 3.4. All four mechanisms show a trend where the burning velocity is decreasing non-linearly with increasing pressure.

The GRI Mech 3.0 [27] has 53 species in the scheme and shows the best agreement with the experimental results. Only at a pressure of 4.5 bar the measured burning velocity deviates approximately by 1 cm/s. The mechanism by Kon-

nov [28] is accurate at atmospheric pressure and shows a large deviation from GRI Mech 3.0 for elevated pressures. The DRM19 and DRM22 mechanisms [26] (consists of 19 and 22 species respectively) both show higher velocities at atmospheric pressure (39.3 and 39.6 cm/s respectively). The DRM19 mechanism shows deviations between 7 % and 11 % compared to the GRI Mech 3.0 mechanism for pressures ranging from 1 to 15 bar. For higher pressures the predictions show a better agreement. The velocities calculated with the DRM22 mechanism are slightly higher than those of the DRM19 mechanism over the entire pressure range and therefore deviate more from the GRI Mech 3.0. Although the experimental results show the best agreement with GRI Mech 3.0, the DRM19 mechanism is selected due to lesser number of species for the detailed simulations which ensures faster computations. Before simulating the flame using the detailed DRM19 mechanism, the standard one-step mechanism was also implemented for reasons discussed before. The 2D simulations in the present work predicted the same values of burning velocity as 1D simulations up to a pressure of 12 bar. A validation of the 2D simulations was performed by comparing the experimental results with the predicted laminar burning velocities. A difference of 4 cm/s was observed at 1 bar and 1 cm/s at 4.5 bar.

3.3 Results and Discussion

To determine the curvature and surface area increase of the flame, an indicator for the flame stand-off distance is introduced. The parameter $\delta \mathrm{T_{iso}}$ gives the distance from the burner plate outlet to a certain isotherm with value $\mathrm{T_{iso}}$, and varies from the center boundary to the side boundary, as indicated in figure 3.5. δ_{900} is the parameter used for $\mathrm{T_{iso}} = 900$ K. The center boundary is the axisymmetric axis that is defined through the center of the hole and the side boundary is the symmetry boundary condition that is located above the burner plate. In previous studies (de Goey et al., 1995), the 900 K isotherm has been chosen to determine the curvature, as this is the approximate temperature above which chemical reactions become important. The isotherms for the pressures 1, 5 and 10 bar are illustrated in figure 3.5. The corresponding laminar burning velocities of the three adiabatic cases are used as the inlet velocity. This shows that the flame is flat, when the stand-off distance of the 900 K isotherm is equal along the two boundaries. This is the case at 1 bar and the flame exhibits curvature as the pressure increases. The integration of the 900 K isotherm from center to side boundary and then surface revolution along the center boundary gives the surface area of the curved flame. An increase of the surface area ($\mathrm{S_{incr}}$) is then obtained by comparing it to an ideal flat flame (a circle of diameter 30

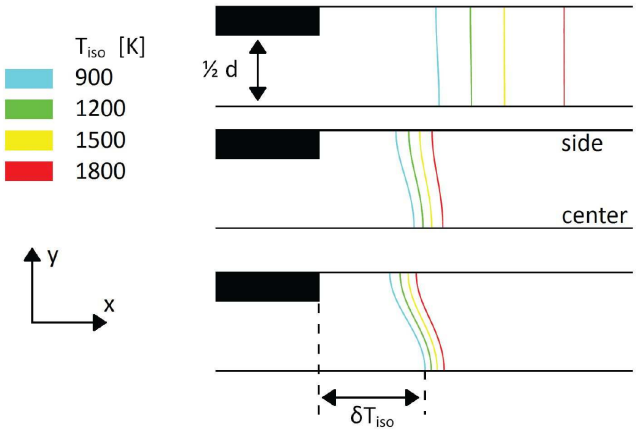

Figure 3.5. $\delta \mathrm{T_{iso}}$ for 1, 5 and 10 bar (top to bottom) of stoichiometric methane-air flame and 300 K (unburnt gas temperature)

mm). The surface area increase according to the 900 K isotherm, is calculated for all the simulations performed with the one-step mechanism and the DRM19 mechanism.

Instead of using the 900 K isotherm to determine the flame curvature, it is also possible to define a different parameter. One of the post-processing options is to present the net reaction rate of methane, $\mathrm{R_{CH_4}}$. This is shown for the simulations at 10 bar in figure 3.6. The curvature of the layer where the reactions take place can also be regarded as a suitable indicator for the flame curvature. The net reaction rate is plotted along the center and the side boundary (figure 3.6). The shift that occurs between the two plots, $\delta_{\mathrm{CH_4}}$ is essentially the same principle as the parameter δ_{900}, used to determine the curvature of the 900 K isotherm. When the flame is entirely flat, the plots are exactly the same and on top of each other. The shift can be measured by determining the curve length between the peaks of the plots.

Simulations using One-Step Mechanism

The surface area increase, $\mathrm{S_{incr}}$ has been calculated according to both the 900 K isotherm and the net reaction rate of methane. The results, using the one-step mechanism and 900 K isotherm ranging from P = 1 to 7 bar, are presented in figure 3.7. The experimentally determined burning velocities [5] were used as the inlet velocity in the models. The results suggest a non-linear increase of $\mathrm{S_{incr}}$ with elevating pressure. The results in figure 3.7 show that the amount

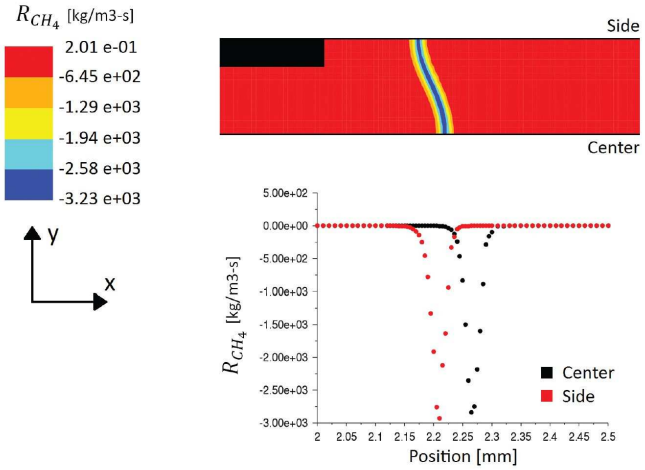

Figure 3.6. Net reaction rate of stoichiometric methane-air flame at 10 bar and 300 K (unburnt gas temperature)

of surface area increase strongly depends on the geometry of the burner plate. The amount of S_{incr} is reduced by a factor of 3 when burner plate (2) (black triangles) with $d = 0.3$ mm, $\chi = 0.63$ is used when compared to burner plate (1) (red diamonds) with $d = 0.5$ mm, $\chi = 0.63$. This reduction is achieved by decreasing the hole diameter from 0.5 to 0.3 mm, while the porosity remains constant. The results from burner plate (3) (blue circles) with $d = 0.3$ mm, $\chi = 0.51$, are compared to burner plate (2) with $d = 0.3$ mm, $\chi = 0.63$ to find the influence of the porosity. The amount of S_{incr} is reduced by a factor of 2, when the porosity is increased from $\chi = 0.51$ to $\chi = 0.63$. The significant increase in porosity is achieved by decreasing the pitch of the burner plate by only 0.04 mm.

Detailed Simulations

The detailed simulations using DRM19 mechanism were performed up to 15 bar and show the surface area increase more clearly in figure 3.8. For 1 and 5 bar, the results from the one-step mechanism are included. This shows the influence of using the detailed reaction mechanism. The difference is small between the DRM19 mechanism and the one-step mechanism. At 5 bar, the surface area increases are 1.7 % and 2.2 % respectively. The simulations at 1 bar show a negligible increase for both cases. This suggests that for further simulations, the one-step mechanism is sufficient to determine the approximate surface area increase. The results at 10 and 15 bar clearly show a non-linear increase of the

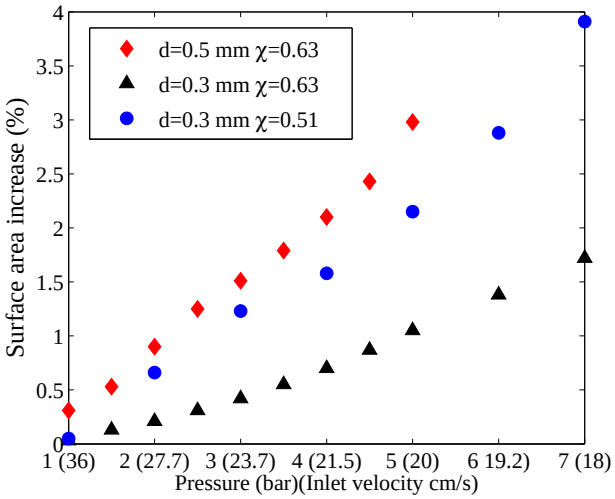

Figure 3.7. Surface area increase of the stoichiometric methane-air flame for the three burner plate models. The inlet velocities mentioned are the experimentally determined laminar burning velocity of stoichiometric methane-air flames at corresponding pressures.

S_{incr} with elevating pressure. The surface area increase determined from the maximum reaction rate of CH_4 shows the same non-linear increase. However, the values are smaller compared to the 900 K isotherm criterion. At 5 bar the S_{incr} is only 0.45 % but it rises quickly to 3.4 % and 11.8 % for 10 and 15 bar respectively.

The detailed species structure of the flat flame is presented in figure 3.9. The profiles of the major species mass fraction along the center and side boundary are compared for the cases at 1 and 10 bar. This shows the influence of the flame curvature and increase in pressure. The dotted vertical blue line represents the location of the burner plate. The case at 10 bar shows the largest difference between both boundaries. This is caused by the large curvature that was already shown in figure 3.5 and 3.6, for the temperature isotherms and the reaction rate of methane. The profiles along the side boundary are shifted towards the burner plate compared to the center boundary. They coincide after the reaction layer, where the flow becomes uniform again and the mixture reaches chemical equilibrium.

The influence of the pressure becomes clear when comparing the two cases of 1 and 10 bar. At elevated pressure, the collision rates of molecules increase, which

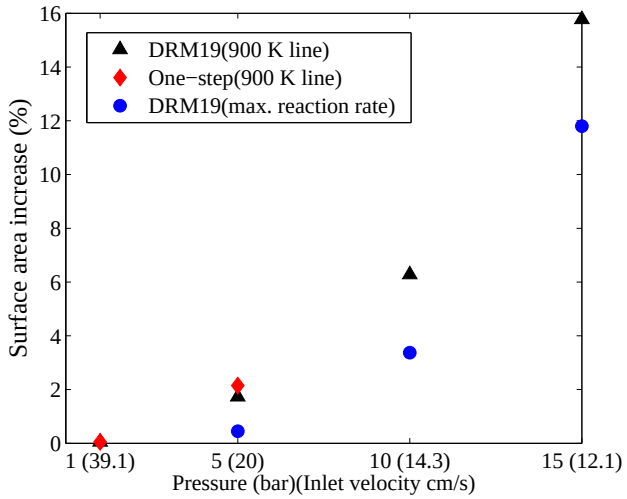

Figure 3.8. Surface area increase of the flame for the burner plate model 3 which resembles the plate used in experiments. The DRM19 mechanism is used for both the criterions namely, 900 K and maximum reaction rate of methane.

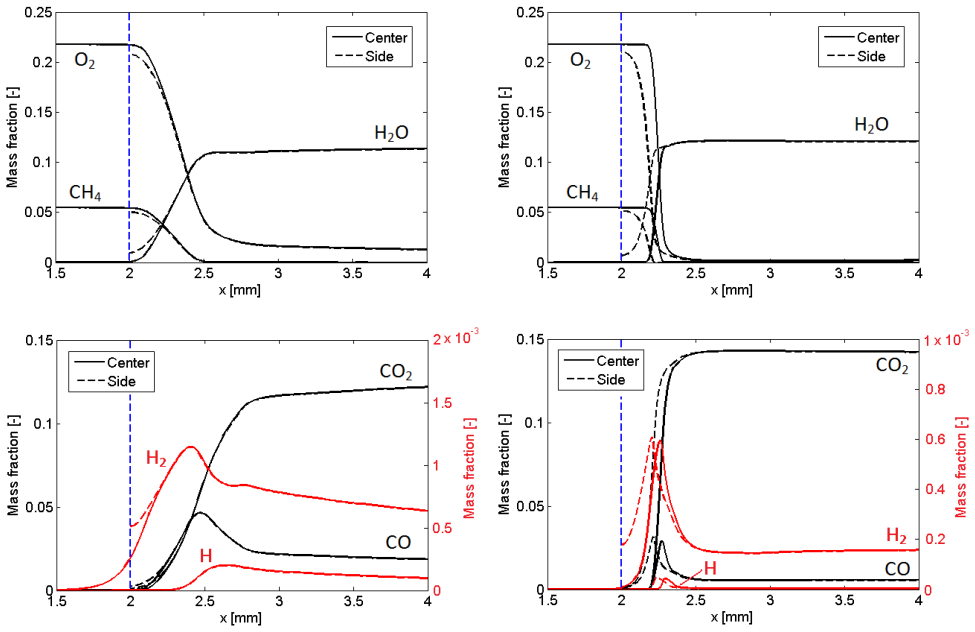

Figure 3.9. Species profiles at (left) 1 bar (right) 10 bar of stoichiometric methane-air flames using DRM19 mechanism for burner plate model 3.

cause the reactions to take place at a higher rate. This decreases the thickness of the reaction layer, which is shown by the steeper mass fraction profiles and the mixture becomes uniform very fast. The maximum mass fractions of H, $\mathrm{H_2}$ and CO are approximately two times lower at 10 bar, which is a result of the high reaction rate. Simulations showed that the maximum reaction rate of methane is approximately 15 times higher at 10 bar compared to atmospheric pressure. Highly mobile hydrogen radicals promote the burning rate of the mixture. It is possible that these radicals recombine at the burner surface, which will influence the measured burning velocity. It can be determined whether there is an increase of this effect with pressure. The main sources of H radicals during the combustion process are the CO oxidation reaction 3.9 and the HCO decomposition reaction 3.10 [29].

$$\mathrm{OH}+\mathrm{CO} \leftrightarrow \mathrm{H}+\mathrm{CO_2} \tag{3.9}$$

$$\mathrm{HCO}+\mathrm{H_2O} \leftrightarrow \mathrm{H}+\mathrm{CO}+\mathrm{H_2O} \tag{3.10}$$

The potential influence of burner surface reactions may take place as the radicals might reach the surface. An experimental study was performed by Hermanns [17] at ambient conditions by using a gold coated burner plate and a conventional brass burner plate. It was observed that the laminar burning velocity was not influenced. In the present work, the species profiles show an increase of $\mathrm{H_2}$ on the burner plate, compared to the center boundary. The H radicals are almost zero at the burner plate and show a peak in the reaction layer. For the cases at 1 and 10 bar, the concentration of H radicals at the burner plate are six orders of magnitude smaller compared to the maximum present in the flame. This shows that the increase in pressure does not influence surface reactions at the burner plate.

To minimize the flame curvature effects, the hole diameter must be reduced and the porosity must be increased. Presently, the holes are drilled in the brass plate and a hole diameter of $\mathrm{d} = 0.25$ mm should be considered as the lower limit. Somers [19] recommended to use porosities higher than $\chi = 0.67$. It was found that the porosity of $\chi = 0.8$ can be considered as an upper limit to avoid corrosion of the burner plate material. The burner plate that is expected to show the least amount of surface area increase, should therefore have a hole diameter of $\mathrm{d} = 0.25$ mm and a pitch of $\mathrm{s'} = 0.29$ mm. This corresponds to a porosity of $\chi = 0.67$. It will also be interesting to perform a study in the future that correlates the surface area increase to corrected laminar burning velocity of a fuel-oxidizer mixture.

Summary

Two-dimensional axisymmetric simulations were performed on stoichiometric methane-air flat flames using three burner plate designs used in the heat flux method at elevated pressures. The surface area increase of the curved flames, compared to a perfectly flat flame is calculated according to the 900 K isotherm and the reaction rate of methane. Both show the same trend in surface area increase with elevating pressure. Three burner plates have been modeled for pressures up to 7 bar with a one-step mechanism. The comparison of these models shows that the surface area increase can significantly be reduced by choosing a smaller hole diameter and larger porosity. The results of the detailed simulations using DRM19 chemical reaction mechanism up to 15 bar show a non-linear increase of the flame curvature with elevating pressure. The surface area increase of the methane-air flame is around 16 % at 15 bar with the burner plate that is used in the current heat flux method experimental setup. This must be reduced by manufacturing a new burner plate with a smaller hole diameter and a larger porosity.

CHAPTER 4

High Pressure Experimental Facility

The experimental tool used in this thesis is explained in chapter 2. This chapter is dedicated in explaining the number of additions made to the basic HFM setup in order to make it functional at elevated pressures. The initial idea of a high pressure system was borrowed from the published work of Kobayashi et al. [30] which uses a nozzle-type burner.

4.1 High Pressure HFM-I

In HFM, heat loss from the flame is compensated by adding heat to the unburnt gas mixture. As the name suggests, the method requires a balance in the heat flux and the most relevant variable in this technique is the burner plate temperature profile. The main principle of the HFM is to stabilize a flat flame with unburnt gas velocity such that the heat loss by the flame is compensated by heat gain by the unburnt gases. When the unburnt gas velocity is higher than the laminar burning velocity (super-adiabatic) the heat gain by the gas is larger than the heat loss from the flame and the center of the burner plate is colder than the edges. The situation is opposite in case of a sub-adiabatic

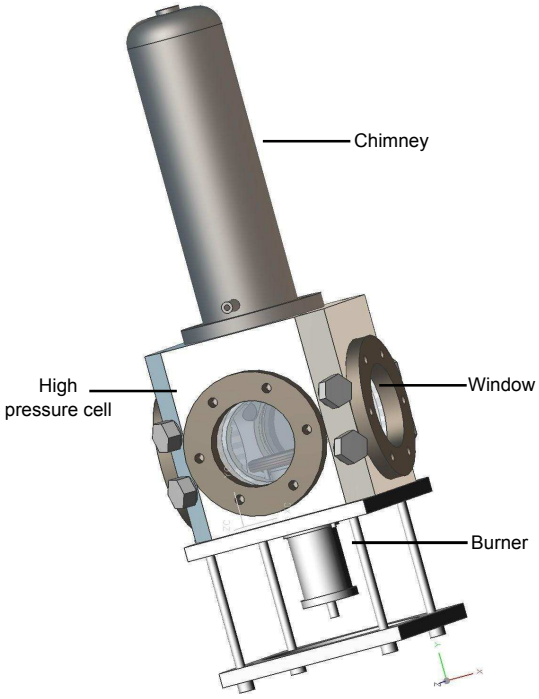

Figure 4.1. High pressure cell assembly rated up to 10 bar (HPHFM-I).

flame. The measurement required in this technique is the temperature profile of the burner plate. In practice, it is difficult to attain a strictly adiabatic flame. The radial profile of temperature in the burner plate close to the laminar burning velocity is fitted by the method of least squares to a parabola. The coefficients of such parabolas are plotted against sub and super-adiabatic flow velocities. The adiabatic state is reached for zero value of the coefficient (flat temperature profile). The procedure for measuring the temperature and evaluating the burning velocity is described in chapter 2 and elsewhere [16].

In this setup, the burner used is exactly the same as described in chapter 2. The burner plate used in this setup has a diameter of 3 cm. The burner is housed in a high-pressure cell made of C45 steel designed for pressures up to 10 bar. A chimney is placed on top through which burnt gases are guided out. A stainless steel connection pipe followed by a needle valve is connected to the exhaust of the chimney. The pressure in the vessel is controlled by this needle valve.

The complete assembly of the high pressure environment is shown in figure 4.1.

The heat flux burner is attached to the bottom of the high pressure cell (HPC) and the chimney is placed on top. The HPC was designed to withstand pressures up to 30 bar. It is essentially a cubic casing with a large hole (diameter 100 mm) on each side of the cube. The four holes on the sides are used to make the vessel optically accessible with Sapphire windows. The casing is made out of C45 steel and it is blued to passivate oxidation. The chamfered edges of the cube contain two smaller holes each. These holes can be used to enter the vessel or to install extra equipment to check the conditions in the HPC. In the current setup, two holes are used. One contains a type T thermocouple to measure the temperature inside and the other one has a pressure transducer to measure the pressure (with a maximum of 7 bar and a sensitivity of 0.05 bar). The chimney is designed for pressures up to 30 bar. It is made out of stainless steel with an outer diameter of 101.6 mm, a height of 480 mm and a wall thickness of 5.6 mm. Inside the chimney there is a gutter to catch the condensed water produced by the combustion. It is connected to the HPC with screws and a Sigraex Hochdruck package ring is placed in between them to make the connection leak tight. This ring can withstand pressures up to 250 bar and temperatures up to 500 °C. The exhaust gases leave the chimney at the top, through a stainless steel Swagelok pipe (diameter 6 mm). At the end of this pipe, a needle valve is installed to control the pressure inside the high pressure environment.

In line with the research for measuring laminar burning velocity at higher pressure, the above mentioned heat flux system (HPHFM-I) was a trial system to assess the parameters that need to be modified in order to obtain a system that can function well at 30 bar. Measurements up to 9 bar were conducted on this system and parallely another system (HPHFM-II) was built keeping in mind the complexities that may appear during high pressure operations. The main issues encountered during the operations of HPHFM-I are listed below:

- The high pressure cell walls heats up fast enough. The exhaust gases within the cell heats up the walls and the burner itself. A cooling system was required where cold air/nitrogen gas could be homogenously circulated. This was implemented in HPHFM-II. The volume of the new high pressure cell is many times higher.

- The burner initially used in HPHFM-I had an electrical heating coil around the burner head to heat up the burner plate to 85 °C. The conduction between the coil, burner head and burner plate was not found to be good. This was reflected in the temperature profile of the burner plate. The flame often could not be stabilized in absence of proper conduction. In

the subsequent design of the burner, heating was implemented through water baths.

- The burner designed and fabricated for HPHFM-II has a burner plate of 2 cm diameter (instead of 3 cm diameter). A smaller flame surface is easier to stabilize due to lower heat release and gas consumption. In a high pressure environment it is important to make sure that an accurate pressure is obtained in order to realize a stable flame.
- HPHFM-II was also equipped with automatic pressure controller rather than manual operation. This reduces much of the physical effort of the user and ensures higher accuracy in pressure. Also, small fluctuations in pressure are minimized to a great extent.
- The entire setup in HPHFM-II including the heat flux burner is capable of handling pressures as high as 30 bar. This helps us in studying flames at conditions relevant for gas turbine operations.

4.2 High Pressure HFM-II

Figure 4.2 gives a schematic of the complete experimental setup for HPHFM-II. The complete assembly of the high pressure cell used in this setup is shown in figure 4.3(a). The front cut section of the system including the burner is shown in figure 4.3(b). The gas flow board consist of three gas lines connected to respective cylinders (air/oxidizer, methane and syngas), buffer vessels, valves and filters. The appropriate amount of fuel and oxidizer is made to flow to the burner through a high pressure line. The line is long enough to ensure that the gases are premixed well before they are burnt. The unburnt gas mixture is maintained at 25 °C by employing a water bath which is connected to the plenum chamber of the burner. An additional water bath is used to heat the burner head to 85 °C. The brass burner plate mounted on the burner head has a diameter of 2 cm. The hole diameter is 0.3 mm, the pitch is 0.4 mm and the thickness of the plate is 1 mm. Six thermocouples of type T (Copper-Constantan) are connected to the burner plate at following radius (mm) - angle (°) positions from the centre: 0 (0°), 2 (330°), 4 (210°), 6 (90°), 8 (270°), 9.8 (150°). Data acquisition is done through a NI 9213 16-channel thermocouple input module.

The high pressure assembly installed in this setup is rated to 30 bar. The burner is connected to the cell from the bottom through a flange which can be bolted. An additional inlet for cold air is provided from the bottom of the cell. The cold pressurized air is first made to pass through layers of soda lime glass balls

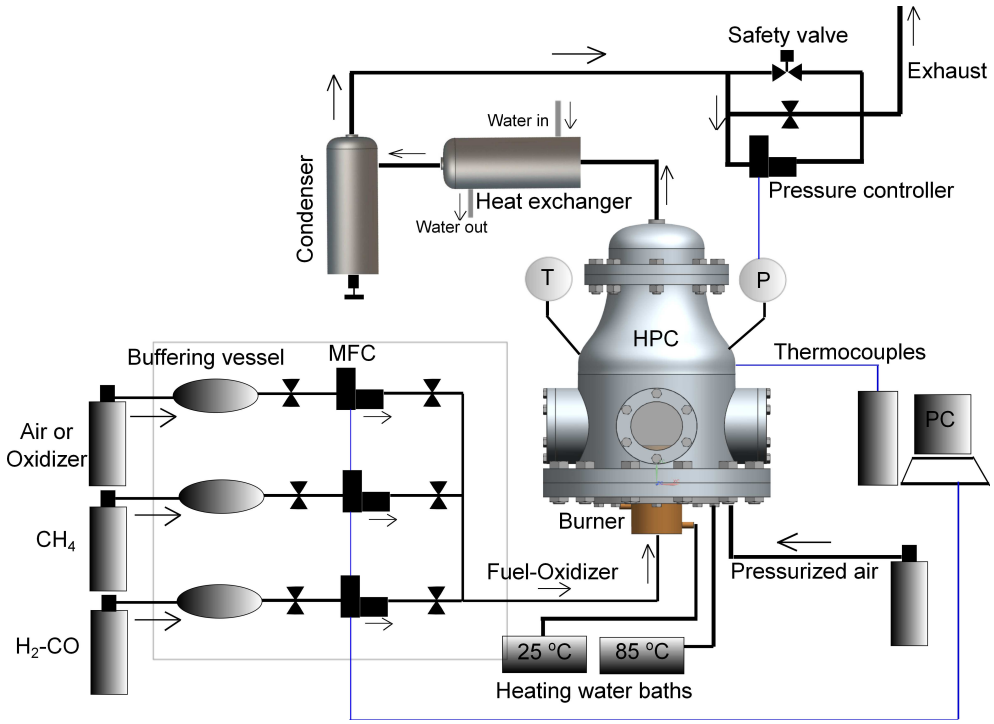

Figure 4.2. High pressure facility equipped with gas flow control board, heat flux system, high pressure cell, heat exchanger, condenser and exhaust line. This facility is rated up to 30 bar.

(diameter 5 mm) to prevent heavy pressure drop. Air is then passed through a concentric ring of a Nickel-Chromium metal foam which is fixed around the burner. This provides conditioned cold air required to cool the hot walls of the high pressure cell.

The high pressure cell includes four high quality quartz windows for optical access. Sensors for pressure and temperature measurement of the cell interior are installed. The Bronkhorst pressure sensor is further connected to a Bronkhorst pressure regulator that regulates the pressure of the cell as per user command. An additional pressure transducer with a dial is installed for visual information. The high pressure cell can be opened also from the top. The top of the cell is further connected to a heat exchanger made of stainless steel. The exhaust gases from the burner are guided through this heat exchanger in order to cool the gases. The water condensed in this process is collected at the bottom of the condenser (stainless steel). The exhaust gases are then guided through the pressure controller and then to the atmosphere. The gases can also be led out

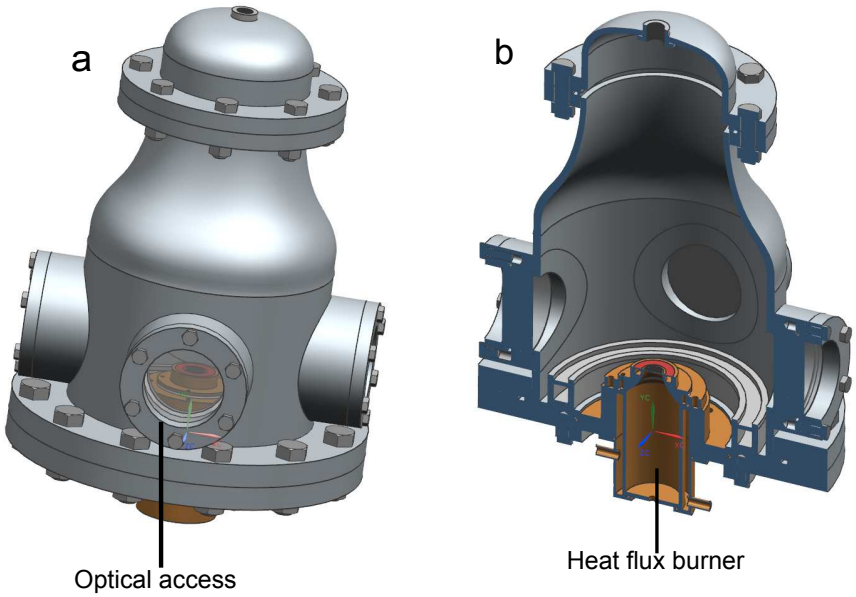

Figure 4.3. 3D model of the high pressure setup rated upto 30 bar (HPHFM-II). (Left) Complete assembly (Right) Front half section view.

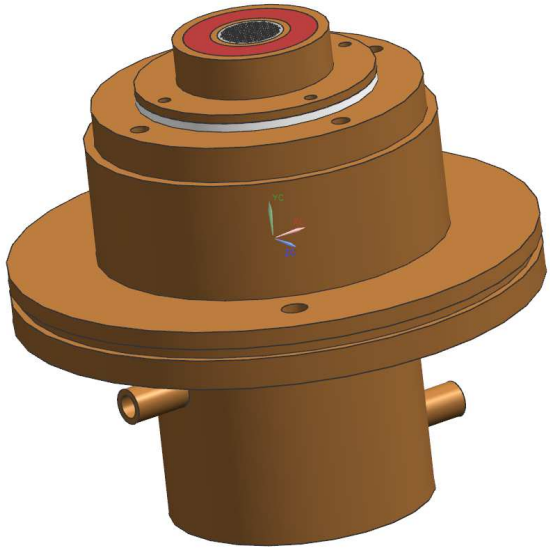

Figure 4.4. High pressure brass burner rated upto 30 bar. The burner houses a burner plate of 2 cm diameter (holes of 0.3 mm diameter, pitch of 0.4 mm, plate thickness of 1 mm).

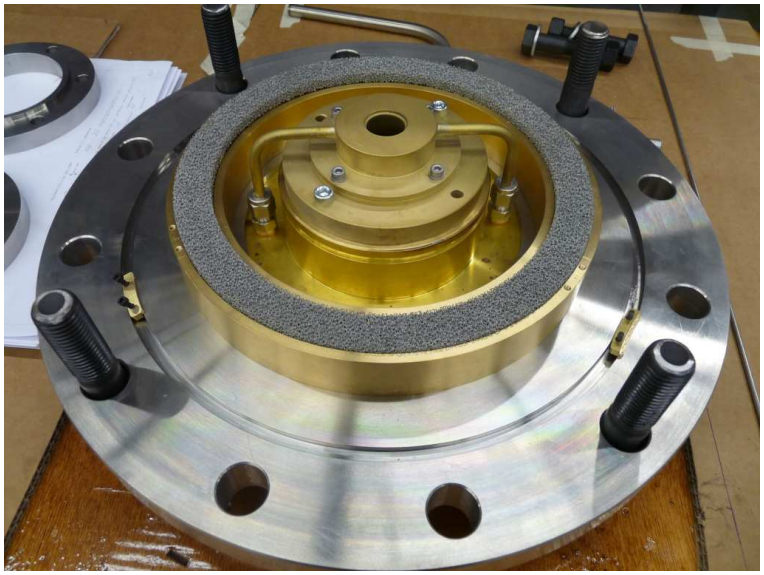

Figure 4.5. Interior of High pressure setup with metal foam ring and burner.

Figure 4.6. A picture of the setup.

through a hand valve (usually closed). A safety valve is installed and fixed at 30 bar in case of excessive pressure buildup. Two pictures of the setup are given in figures 4.5 and 4.6. Important instruments used in this facility are outlined in table 4.1.

Table 4.1. Important instruments used in the high pressure setup-II.

Instrument	Range	Accuracy
Pressure sensor	0.4 - 20 bar(a)	$\pm$0.5 % FS
Pressure controller	2 - 20 bar(a)	$\pm$0.5 % FS
Mass flow controller (H_2/CO)	0.4 - 20 ln/min	0.8 % R + 0.2 % FS
Mass flow controller (CH_4)	0.1 - 5 ln/min	0.8 % R + 0.2 % FS
Mass flow controller (Air/O_2/N_2/He)	3.2 - 160 ln/min	0.8 % R + 0.2 % FS
Pressor gauge	1 - 30 bar(a)	0.1 bar(LC)
Two Temperature sensor	273 - 1200 K	$\pm$ 1 K
Eight Type T thermocouples	273 - 700 K	$\pm$0.1 K
Temperature module NI9213	16-channel	

4.3 Nitrogen Flushing System

Many experiments were focussed at H_2-CO mixtures with compositions 50:50 and 85:15 %. The presence of a highly toxic gas like CO and extremely flammable gas like H_2 makes it important to make the laboratory space safe for the user. To ensure that the gas lines are flushed well before and after experiments, a nitrogen flushing system was installed. The line is also flushed before changing cylinders and before long breaks between experiments. Figure 4.7 shows the complete line used for such a system. The key component used in this installation is the gas panel with four-way valves. The panel connects to the syngas cylinder, nitrogen cylinder, high pressure system and to the atmosphere. Gas detectors were installed in the room with an alarm system.

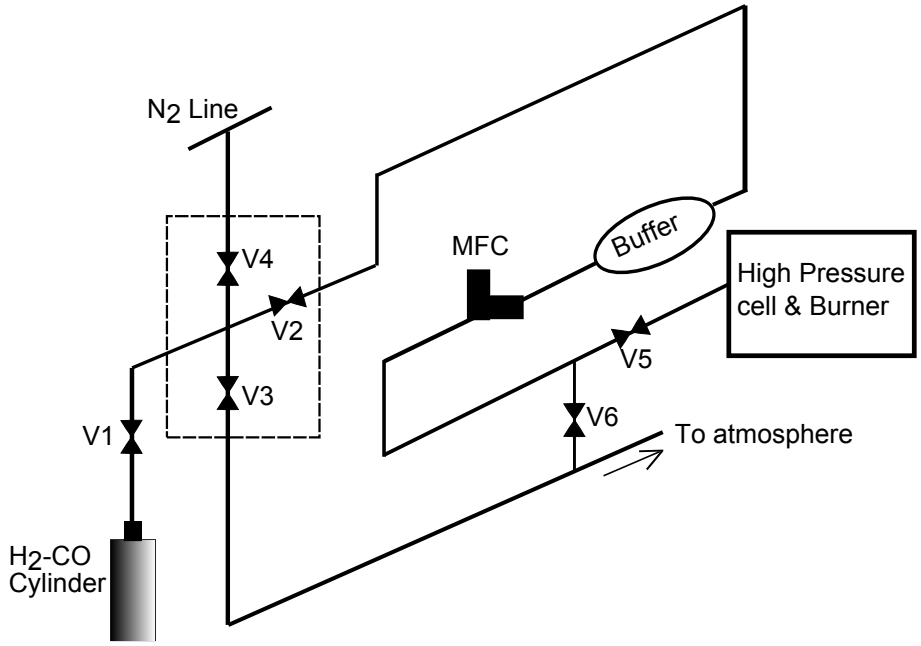

Figure 4.7. N_2 flushing line for H_2-CO gas mixture flushing while cylinder change or shutoff. This ensures laboratory safety.

Summary

The two experimental setups used for high pressure experiments are explained in detail. The heat flux method burners are installed in high pressure environments rated up to 10 bar (setup-I) and 30 bar (setup-II). The results obtained from these setups are discussed in chapters 5 and 6.

CHAPTER 5

Experimental Results: Lower Alkanes

This chapter presents the experimental results at elevated pressures up to 5 atm. The following sections discuss the laminar burning velocities obtained for lower alkane fuels : Methane, Ethane and Propane. In the first section, a literature review of experimentally determined S_L of methane-air mixtures is done. The correlations found in the literature are outlined and analyzed. The S_L obtained in the present work is further used to derive pressure dependent correlations for methane-air mixtures with initial temperature of 298 K. The section following that simply outline the S_L results obtained for ethane and propane for pressure up to 4 atm. [1]

5.1 Methane

Combustion of methane as the main constituent in natural gas has been a key field of research for many years. Methane (or natural gas) is burnt, premixed or non-premixed, in a large variety of conditions: at room and elevated initial

[1] *A part of results shown in this chapter has been published by Goswami et al., Combustion and Flame 160 (2013) 1627-1635.*

temperatures, at atmospheric and elevated pressures. Certain applications like industrial gas turbines require pressures as high as 30 atm. For premixed conditions, the laminar burning velocity (S_L) is a key parameter that governs many properties of combustion. Also, in determining turbulent burning velocities or other flame properties, an accurate correlation of the laminar burning velocity as a function of pressure is essential [30, 31]. In spite of the large amount of research spent on the high pressure dependence of methane - air laminar burning velocity, there still exists a large uncertainty in the data for various reasons. Part of the uncertainty is related to the rather limited accuracy of the high pressure laminar burning velocity measurements so far. The objectives of this work are twofold : (1) to extend the heat flux flat flame method towards elevated pressure (up to 5 atm) and (2) to analyze variation of the pressure exponent β_1 with mixture composition both experimentally and from predictions of two selected chemical reaction mechanisms. As will be shown, the presented data are accurate and in very good agreement with modeling results, which reduces the scatter in the reported data so far and leads to a more accurate pressure dependence. This section is organized as follows: After an in depth literature review of the current knowledge on pressure dependence of the burning velocity today, the extended experimental heat-flux technique will be presented along with measurements and modeling results of methane (CH_4) - air mixtures. The discussion focuses on pressure dependence as a function of equivalence ratio which shows some new elements for further research.

Literature Review

The laminar burning velocity is a fundamental property of each combustible mixture that depends on its composition, initial temperature (T) and pressure (P). The first evidence of the effect of pressure on burning velocity was provided by Ubbelohde and Koelliker [32], who covered the range from 1 to 4 bar. Experimental results accumulated during the years since were often interpreted using power-law pressure dependence

$$\mathrm{S_L} = \mathrm{S_{L0}} \left(\frac{\mathrm{P}}{\mathrm{P_0}}\right)^{\beta_1}, \tag{5.1}$$

where S_{L0} is the burning velocity at reference conditions (usually at 1 atm), and P_0 is the reference pressure. Interpretation of the pressure dependence of the laminar burning velocity using equation 5.1 has its rationale in early theories of flame propagation. The very first thermal theory of Mallard and Le Chatelier [33] considered only heat and mass balance and indicated inverse dependence of S_L with pressure. Jouguet [34], Crussard [35], Nusselt [36], and Daniell [37] developed this theory explicitly introducing an overall reaction rate W'. Zeldovich

and Frank-Kamenetsky [38] further advanced this theoretical approach showing that the mass burning rate $\mathrm{m'} = \rho\ \mathrm{S_L}$ is proportional to the square root of the overall reaction rate $\mathrm{W'}$. Since $\mathrm{W'}$ is proportional to $\mathrm{P^n exp(-E_a/RT)}$, where n is the overall reaction order, the mass burning rate shows a power exponent dependence of $\mathrm{n/2}$. The power exponent β_1 is therefore equal to $\mathrm{n/2-1}$, which is 0 for bimolecular reactions and -0.5 for first order reactions. This consideration is still often used for interpreting changes of the overall reaction order with pressure, e.g. [39, 40].

Another type of the pressure dependence correlation,

$$\mathrm{S_L} = \mathrm{S_{L0}}\,[1+\beta_2\ \log(\frac{\mathrm{P}}{\mathrm{P_0}})] \tag{5.2}$$

was first proposed by Agnew and Graiff [41] with the value β_2 = -0.206 for a stoichiometric methane - air mixture. Sharma et al. [42] interpreted their measurements using equation 5.2 and presented coefficients β_2 for several equivalence ratios (ϕ) from 0.8 to 1.2 , all close to -0.2. Iijima and Takeno [43] derived a similar correlation with the parameter β_2 linearly dependent on the stoichiometry. Bose et al. [44] suggested discrete coefficients β_2 similarly to their earlier study [42]. Equations 5.1 and 5.2 are in fact related through series expansion as was noticed by Dahoe and de Goey [45], although the values of β are not equal.

An entirely different correlation

$$\mathrm{S_L} = \mathrm{S_{L0}}\ \exp\,[\mathrm{b}(1-(\frac{\mathrm{P}}{\mathrm{P_0}})\,\mathrm{x})] \tag{5.3}$$

was proposed by Smith and Agnew [46]. Since the parameters b and x were found to be dependent on the composition of the oxidizer and the burning velocity at reference conditions, respectively, it was not attempted by others except by Konnov et al. [18] for sub-atmospheric methane + hydrogen + air flames.

Other empirical correlations describing pressure and temperature dependence of the burning velocity were proposed as well, since it was recognized early that the power exponent β is different at different pressures, initial temperatures and varies with mixture composition. Babkin and Kozachenko [47] performed extensive studies of methane - air flames covering a wide range of equivalence ratios, initial temperatures and pressures. They demonstrated that the power exponent β decreases with the increase of pressure within the range from 1 to 8 atm, while in the range from 8 to 70 atm the exponent is almost constant. It has its maximum value in near-stoichiometric mixtures decreasing towards lean

and rich mixtures.

Even after this seminal study [47], correlations in the form of equation 5.1 or 5.2 are often used, knowing that the power exponent β_1 or coefficient β_2 does not have a constant value. Table 5.1 summarizes experimental data and empirical expressions for the power exponent β_1 (equation 5.1), while Table 5.2 summarizes these for the coefficient β_2 (equation 5.2) at fixed temperature close to 298 K in methane + air flames. Andrews and Bradley [48] reviewed available experimental data before 1972 and proposed the correlation $\mathrm{S_L}\ 43\ \mathrm{P}^{-0.5}$ cm/s (where pressure, P is in atm) for stoichiometric mixtures at pressures above 5 atm. Kobayashi et al. [49] accepted the same power exponent for an equivalence ratio of 0.9 in their analysis of high-pressure turbulent flames. This value was also confirmed experimentally for stoichiometric flames up to 100 atm [50]. Summarizing their own [51] and other data available, Rallis and Garforth [52] suggested to consider three pressure ranges as listed in Table 1 with β_1 = -0.51 above 3 atm. Hill and Hung [53] found a value of -0.299 for β_1 in stoichiometric mixtures between 1 and 8 atm. Stone et al. [54] proposed for stoichiometric methane - air flames from 0.5 to 10.4 bar an empirical correlation with the power exponent, β_1= -0.297, in accordance with Hill and Hung [53]. When other mixture compositions were taken into account the correlation β_1 = -0.314 + 0.608 (ϕ - 1) was derived. Stone et al. [54] found favorable agreement with Iijima and Takeno [43] who used equation (2), at some conditions around 5 atm. Gu et al. [55] performed their experiments in three mixtures and derived distinct power exponents for lean, stoichiometric and rich flames, while Elia et al. [56] proposed a single value, applicable also for diluted mixtures.

Dahoe and de Goey [45] reviewed and interpreted available experimental data using equation 5.1 and 5.2. In the range from 1 to 10 atm they found that for a stoichiometric mixture, the power exponent β_1 in equation 5.1 has a value of -0.41, but it can vary between -0.2 and -0.6. For equation 5.2 the coefficient β_2 has a value of -0.28, but it can vary between -0.15 and -0.4. From the analysis of the thin-flame model of flame propagation in closed vessels, Dahoe and de Goey [45] also concluded that the values of β in equation 5.1 or 5.2 should be decreasing functions of equivalence ratio from lean (0.7) to rich (1.4) mixtures. This contradicts the observations of Babkin and Kozachenko [47] and other works mentioned above. Recent studies of Liao et al. [57] and Halter et al. [58] confirmed that the power exponent β_1 has its maximum value in near-stoichiometric mixtures, decreasing towards lean and rich mixtures.

Variation of the power exponent β_1 with pressure and mixture composition was confirmed by the detailed kinetic modeling of methane flames as well. Tsatsaro-

Table 5.1. Selected experimental data and empirical expressions for the power exponent β_1 (equation 5.1) at fixed temperature close to 298 K in methane + air flames.

T [K]	P [atm]	ϕ	Correlation	$\beta_1(\phi{=}1)$	Ref
323-473	1-8	0.6-1.4	Discrete values	-0.270	[47]
	8-70			-0.430	
300	5-90	1		-0.500	[48]
298	0.6	1		-0.120	[59]
	4			-0.51	
298	0.6	1		-0.145	[52]
	0.6-3			-0.265	
	3-10			-0.510	
300-500	1-8	1		-0.299	[53]
300	0.5-5	0.6-1.4			[39]
298	0.05-20	0.7-1.3	Discrete values	-0.500	[60]
295-454	0.5-10.4	0.6-1.4	-0.314+0.608(ϕ-1)	-0.297	[54]
300-400	1-10	0.8-1.2	Discrete values	-0.374	[55]
298-550	0.75-70	0.8-1.2		-0.435	[56]
300	1-20	0.7-1.4			[40]
298	1-10	0.7-1.4	-0.461-0.107(ϕ-1)	-0.410	[45]
300-400	0.5-1.5	0.6-1.4	$-0.92\phi^2+2\phi-1.4$	-0.398	[57]
298	1-5	0.7-1.2	Discrete values	-0.480	[58]
298-498	1-5	1		-0.37	[61]
300-850	1-15.2	0.5-1.2	$-0.7\phi^2+1.4\phi-1.1$	-0.400	[62]
300-950	1-11	0.6-1.3			[63]

nis [59] found that calculated burning velocities at pressures below 60 kPa show a much lower pressure exponent β_1 = -0.12, which differs significantly from the calculated power exponent of -0.51 at pressures greater than 4 atm. Egolfopoulos and Law [39] compared their measurements with model predictions and found that the overall reaction order n (and consequently power exponent β_1) decreases with increasing pressure and also for lean and rich mixtures. Shebeko et al. [60] reported calculated power exponents β_1 for several lean flames averaged over a wide range of pressures (0.05 - 20 atm). Rozenchan et al.

Table 5.2. Selected experimental data and empirical expressions for the coefficient β_2 (equation 5.2) at fixed temperature close to 298 K in methane + air flames.

T [K]	P [atm]	ϕ	Correlation	$\beta_2(\phi{=}1)$	Ref
300	0.5-20	1		-0.206	[41]
300-600	0.5-4	0.8-1.2	Discrete values	-0.195	[42]
291-500	0.5-30	0.8-1.3	-0.42-0.31(ϕ-1)	-0.420	[43]
300-520	2-6	0.85-1.3	Discrete values	-0.202	[44]
298	1-10	0.7-1.4	-0.36-0.0554(ϕ-1)	-0.280	[45]

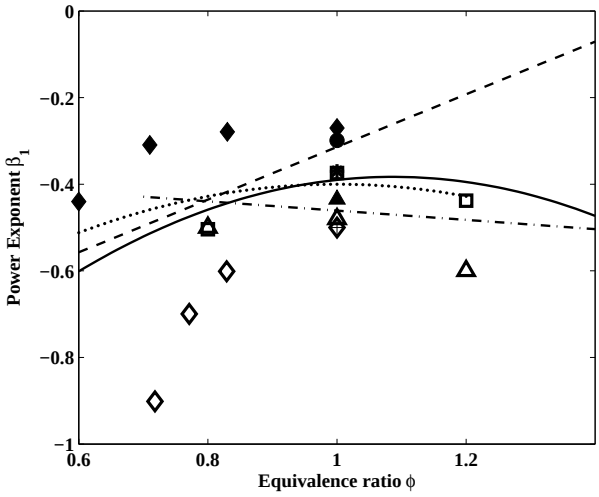

Figure 5.1. Variation of the power exponent β_1 (equation 5.1) with equivalence ratio at elevated pressures. Solid diamonds: [47], squares: [55], circle: [53], open triangles: [58], solid triangle: [56], cross: [48], open diamonds: [60], star: [61], solid line: [57], dashed line: [54], dash-dot line: [45], dotted line: [62]

[40] extended the study of Egolfopoulos and Law [39] towards higher pressures and demonstrated that the overall reaction order for different equivalence ratios exhibits a non-monotonic behavior with minimal values around 4 - 5 atm. Ouimette and Seers [62] used GRI Mech 3.0 [27] for burning velocity calculations and suggested a parabolic function of equivalence ratio for the power exponents β_1. Most recently Bougrine et al. [63] attempted several models, chose GRI Mech. 3.0 and performed extensive modeling of methane + hydrogen + air flames. Their empirical multi-parameter correlation is difficult to interpret or compare with equation 5.1 or 5.2.

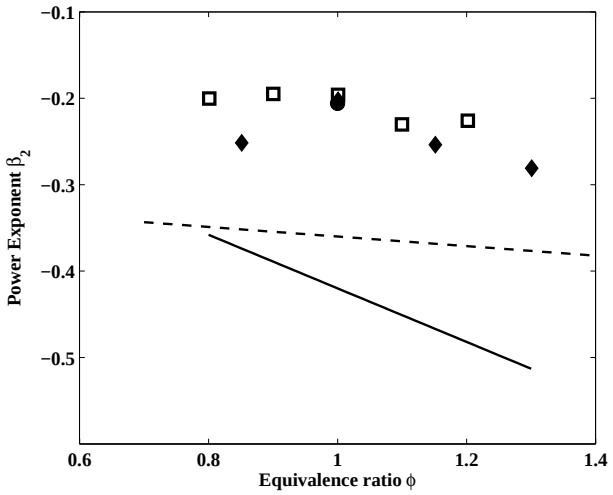

Figure 5.2. Variation of the coefficient β_2 (equation 5.2) with equivalence ratio at elevated pressures. Circle: [41], diamonds: [44], squares: [42], solid line: [43], dashed line: [45]

Figure 5.1 illustrates significant spread of the available experimental data and empirical expressions for the power exponent β_1 (equation 5.1), while figure 5.2 illustrates these for the coefficient β_2 (equation 5.2) at fixed temperature close to 298 K in methane - air flames. The data (symbols) and empirical expressions (lines) relevant to pressures above 1 atm are shown since the focus of the present study is on variation of the pressure exponent at elevated pressures. Besides the variation of the power exponent with pressure its determination could be complicated by the development of cellularity at higher pressures [40] or by the lack of stretch correction in earlier experimental studies.

Results and Discussion

The in-house laminar code CHEM1D [19] is used for modeling a 1D combustion process for the determination of the laminar burning velocity. CHEM1D solves a set of equations describing the conservation of mass, momentum, energy and chemical components for chemically reacting flows. More description of this code is given in chapter 7. The two reaction mechanisms used in this work are GRI Mech 3.0 [27] and USC Mech II [64]. The former was optimized to model natural gas combustion, including NO formation and reburn chemistry in the range of pressures from 10 Torr to 10 atm. It has been used over the years

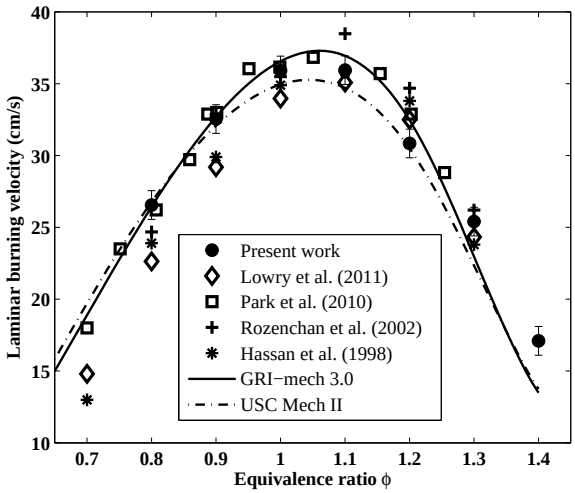

Figure 5.3. Comparison of laminar burning velocities of methane - air mixture at atmospheric pressure.

and has been successful in delivering good results for natural gas and methane. USC Mech II kinetic model is a reaction mechanism relevant mainly to high-temperature oxidation of hydrogen, carbon monoxide and C1-C4 hydrocarbons. It has been developed on the basis of, among other sub-models, GRI Mech 1.2 and 3.0. Validation tests for laminar burning velocities were limited to 1 atm [64]. However, recent work of Park et al. [6] validates this mechanism for pressure up to 4 atm for methane - air flames.

Experiments were performed from $\mathrm{P} = 1$ to 5 atm and for $0.8 < \phi < 1.4$ where ϕ is the equivalence ratio. The error estimate for laminar burning velocity (listed in appendix A) associated with this technique was less than 0.8 cm/s [16, 65]. Errors associated with equivalence ratio were less than 0.025 for all experiments. A complete summary of the measurement data is given in Table A1 in appendix A. Comparison with experimental results of Park et al. [6], Rozenchan et al. [40], Hassan et al. [66] and Lowry et al. [67] and numerical simulation using GRI Mech 3.0 and USC Mech II are presented in figure 5.3 for atmospheric pressure. Good agreement is seen in general including the kinetics.

Figure 5.4 shows the dependence of $\mathrm{S_L}$ for $0.6 < \phi < 1.4$ at selected pressures up to 5 atm. For comparison, experimental data from literature [6, 40, 49, 55, 66, 8] have been included together with predictions of GRI Mech 3.0 and USC Mech II. Both mechanisms are efficient in capturing the behavior of $\mathrm{S_L}$.

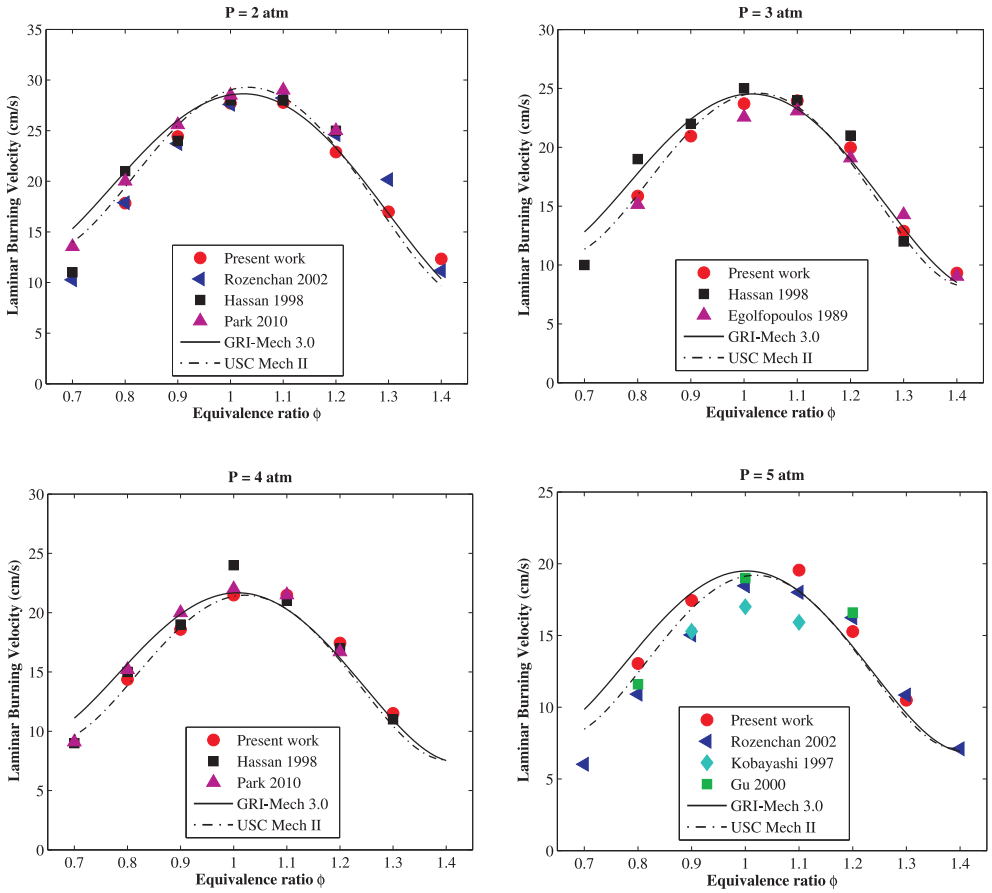

Figure 5.4. Comparison of laminar burning velocities of methane-air mixture from experimental results at 2, 3, 4 and 5 atm as function of equivalence ratio with literature [6, 40, 49, 55, 66, 8] and simulations [27, 64]

USC Mech II uses certain reaction rate constants from GRI Mech 3.0 and still shows cases with a significant divergence from GRI Mech 3.0. The fact that this mechanism is tuned for high temperature applications makes it behave differently.

To analyze the apparent pressure dependence, measured burning velocities of methane - air flames at different equivalence ratios were first plotted on a logarithmic scale as shown in figure 5.5. This should also be mentioned that $\mathrm{P} = 1.5$ atm was close to the lowest pressure achievable at the present setup even with completely opened needle valve (figure 4.1); accurate pressure regulation therefore was problematic near $\mathrm{P} = 1$ atm. The measurements at 1 atm have been performed on a burner without the high pressure cell. On a logarithmic

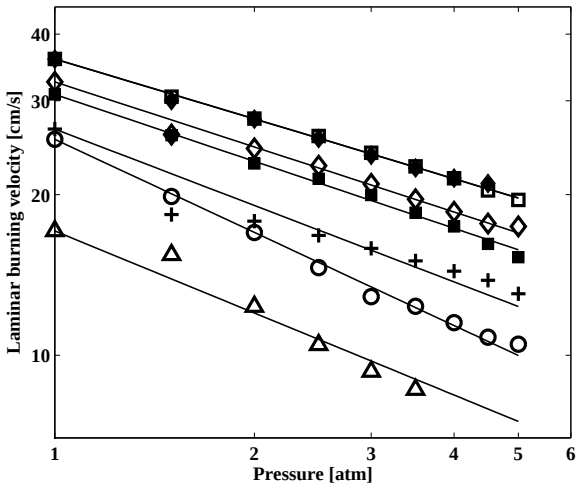

Figure 5.5. Laminar burning velocities of methane-air mixture at different equivalence ratios. Crosses: ϕ=0.8, open diamonds: ϕ=0.9, solid diamonds: ϕ=1.0, open squares: ϕ=1.1, solid squares: ϕ=1.2, circles: ϕ=1.3, triangles: ϕ=1.4.

scale, the most frequently used power-law pressure dependence (equation 5.1) should become a straight line. This is indeed observed for all equivalence ratios with minor deviations at $\phi = 0.8$ and 1.4 and pressure of 1.5 atm. Slowly burning very rich and very lean flat flames are weak and could be easily affected by the ambient air entrainment as was demonstrated and discussed elsewhere [68]. In view of this, the flame can experience very small pressure fluctuations at 1.5 atm since large amount of gases escape the system (accounted by larger error bars in figure 5.6). Residuals calculated as the difference between experimental values and best-fit power law dependencies (straight lines in figure 5.5) were all smaller than 1 cm/s at a pressure of 2 atm and higher.

Calculations performed using GRI Mech 3.0 [27] and USC Mech II [64] have also been processed to derive power exponents β_1 (equation 5.1). Although the modeling results plotted on a logarithmic scale look quite linear, careful analysis shows that they do not exactly follow equation 5.1. This is in line with earlier observations [39, 40], which demonstrated that the overall reaction order decreases with the pressure increase from 1 to 5 atm. On the other hand, residuals defined as the difference between calculated values and best-fit power law dependences do not exceed 0.8 cm/s in this pressure range.

The power exponents β_1 (equation 5.1) derived from the present experiments

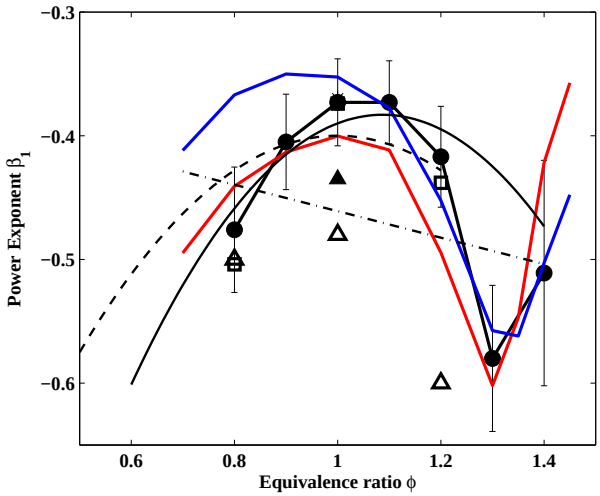

Figure 5.6. Variation of the power exponent β_1 (eq. 5.1) with equivalence ratio at elevated pressures for methane-air mixture. Open squares: [55], open triangles: [58], solid triangle: [56], star: [61], black solid line: [57], dash-dot line: [45], dashed line: [62]. Circles: present work. Red line : GRI Mech 3.0, blue line: USC Mech II

are compared with the selected literature data in figure 5.6. In this graph the older measured values for which no stretch correction was implemented [47, 48, 59, 52, 53, 54] are not shown; also removed were calculated values from [60], since the model employed in that work was not validated elsewhere. Also shown are values of the power exponents derived from the modeling using GRI Mech 3.0 and USC Mech II.

Both the power exponents obtained experimentally and derived using two kinetic models show parabola-like variation with equivalence ratio from moderately lean to moderately rich mixtures in qualitative agreement with the literature [47, 55, 57, 58, 62]. The difference between calculations using GRI Mech 3.0 and USC Mech II is minor in rich flames, increasing toward lean flames. This observation is consistent with figure 5.4, where burning velocities calculated using these two models remain close in rich flames with increasing divergence in lean flames with the pressure increase.

Remarkable non-monotonic behavior of the power exponent β_1 as a function of ϕ (figure 5.6) is found in the very rich flames around equivalence ratio of 1.4. This was not reported in the earlier modeling studies [39, 40] since their analysis was restricted to $\phi = 1.2$ and lower. Babkin and Kozachenko [47]

mentioned irregular variation of β_1 in very rich mixtures with ϕ from 1.3 to 1.4 without specifying it. Close inspection of the raw results presented in [47] shows that in these flames the power exponent first decreases with the pressure increase and then increases again. This was observed by Rozenchan et al. [40] for the equivalence ratio $\phi = 1.2$ at pressures above 5 atm which have not been covered in the present study.

The anomalous behaviour of the power exponent β_1 for very rich mixtures is obviously related to the anomalous behaviour of the power exponent α_1 in the empirical relation $\mathrm{S_L} = \mathrm{S_{L0}}(\mathrm{T}/\mathrm{T_0})^{\alpha_1}$ describing temperature dependence of the laminar burning velocity. Detailed kinetic modeling of methane - air flames showed parabola-like variation of α_1 with equivalence ratio from moderately lean to moderately rich mixtures with sudden change around $\phi = 1.4$ [69]. The non-monotonic behavior of α_1 was then confirmed experimentally [70]. In very rich mixtures methane chemistry is largely different from that of leaner flames. Seshadri et al. [71] in their asymptotic analysis attributed this change to the competition of reaction $CH_3 + CH_3 = C_2H_6$ dominating in very rich flames with reaction $CH_3 + H + M = CH_4$ acting as major radical consumption mechanism elsewhere. Konnov [69] demonstrated that several reactions sensitive with respect to the laminar burning velocity change their sensitivity sign at around $\phi = 1.4$. In very rich flames, a similar analogy may be possible for pressure modifications also and hence, kinetic analysis of such behaviour can be important.

Species profiles and reaction fluxes of CH_4/air mixture were analyzed using GRI Mech 3.0 [27]. Figure 5.7 represents the fluxes of pressure dependent reactions $CH_3 + H (+M) = CH_4 (+M)$ (A) and $CH_3 + CH_3 (+M) = C_2H_6 (+M)$ (B) and $CH_3 + O = CH_2O + H$ (C) at 1 and 5 atm for $\phi = 1$, 1.2 and 1.4. Species profile of CH_3 is included on the secondary y-axis. Reactions A, B and C dominate the consumption of CH_3 which is an important radical in methane oxidation. The present analysis is in line with the discussion of Seshadri et al. [71] at atmospheric pressure. From stoichiometric to rich regime (ϕ=1.4), at $\mathrm{P} = 1$ atm, reaction C that leads in consuming CH_3 at $\phi = 1$ loses to reactions A and B at $\phi = 1.4$. Rate of reaction B increases and soon is in the order of reaction A since more CH_3 radicals are produced in rich mixtures. In case of 5 atm, the flux evolution of reaction C qualitatively remains the same. However, the rate of consumption of CH_3 through reaction B changes by a small amount when compared to reaction A from ϕ=1 to ϕ=1.2 until the rate of B begins to increase rapidly at $\phi = 1.4$. The mole fraction of CH_3 at 5 atm increases until ϕ=1 and subsequently decreases at ϕ=1.4.

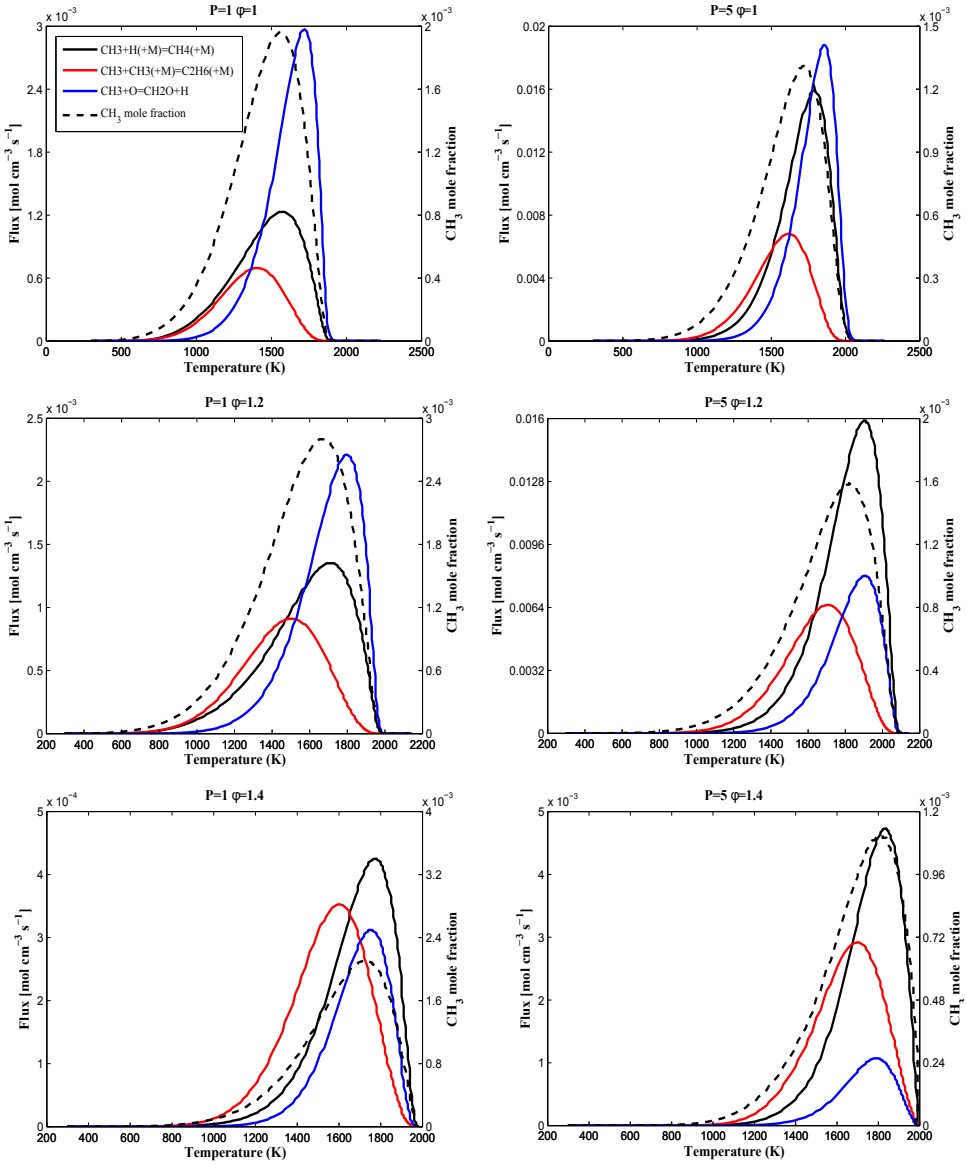

Figure 5.7. CH_3 mole fraction and CH_3 consumption by reactions $CH_3 + H\ (+M) = CH_4\ (+M)$ (A) and $CH_3 + CH_3\ (+M) = C_2H_6\ (+M)$ (B) and $CH_3 + O = CH_2O + H$ (C)

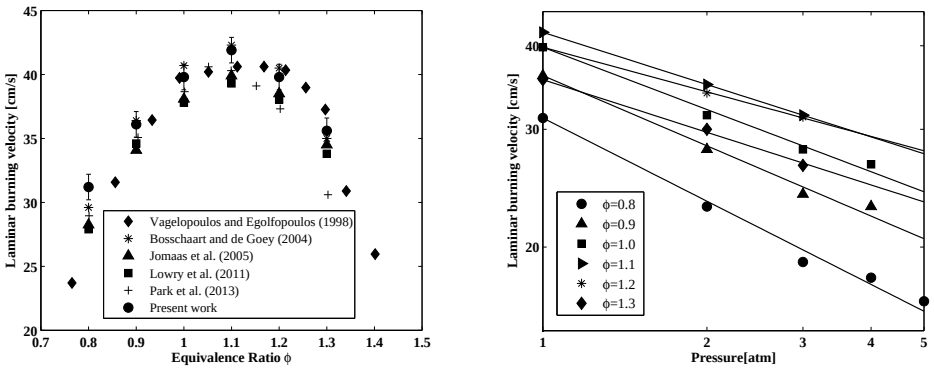

Figure 5.8. Laminar burning velocity of ethane-air mixture at (left) atmospheric pressure compared with literature results [72, 73, 74, 67, 75] and simulation using GRImech 3.0 [27] and (right) elevated pressure.

5.2 Ethane and Propane

Ethane and propane exist in significant shares in natural gas compositions that vary according to applications. Measuring laminar burning velocity of these fuels at higher pressure are relevant for deriving correlations and validating mechanisms that are applied in industrial environments. In continuation to the study of methane-air mixtures at pressures up to 5 atm, a similar and brief study of correlating pressure and laminar burning velocity on ethane (C_2H_6)-air and propane (C_3H_8)-air mixtures is conducted. S_L of these mixtures are measured for varying equivalence ratio ($0.8 < \phi < 1.3$). Figure 5.8 represents the measured values of ethane-air flames at atmospheric and elevated pressure. The atmospheric pressure measurements are compared with literature results [72, 73, 74, 67, 75]. Measurements at $\phi = 0.8$ were extended up to 5 atm. For stoichiometric and $\phi = 0.9$ flames, results could be obtained up to 4 atm. For the rest of the equivalence ratios stable flames could be found only up to 3 atm. In a consolidated representation shown in figure 5.8 (right) linear dependence of S_L on pressure is observed on a log-log scale.

Figure 5.9 (left) presents the measurement results for propane-air mixtures for ϕ 0.8 to 1.3 at atmospheric pressure. A comparison with the literature studies [72, 73, 74, 67] is also presented. High pressure measurements up to 4 atm are shown in figure 5.9 (right). The power exponents for equation 5.1 derived based on experimental results of ethane-air and propane-air flames are presented in figure 5.10 together with those from methane-air experiments. The variation in the values of the power exponents with respect to equivalence ratio show that

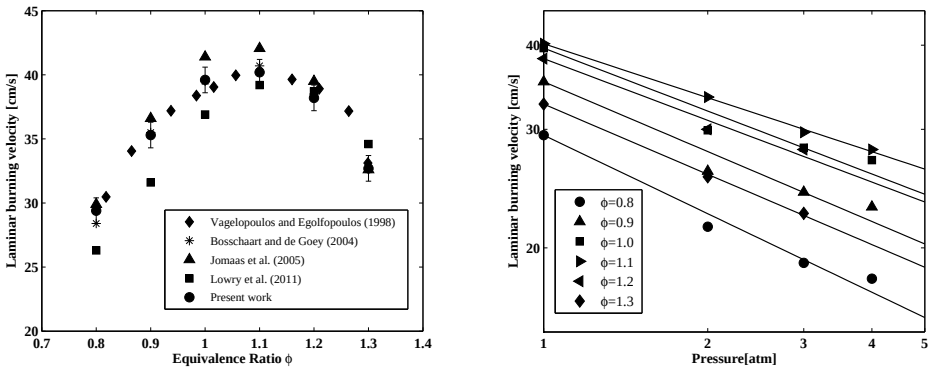

Figure 5.9. Laminar burning velocity of propane-air mixture at (left) atmospheric pressure compared with literature results [72, 73, 74, 67] and (right) elevated pressure.

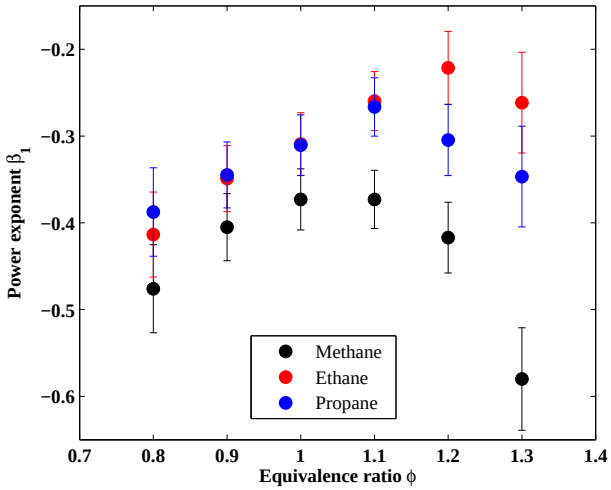

Figure 5.10. Variation of the power exponent β_1 (eq. 5.1) with equivalence ratio at elevated pressures for CH_4-air, C_2H_6-air and C_3H_8-air mixtures.

the pressure dependence of all the three mixtures first increase with ϕ and then decrease after $\phi = 1.2$.

Summary

The capability of the Heat Flux Method (HFM) to accurately measure stretchless adiabatic laminar burning velocities has been demonstrated for elevated pressures up to 5 atm, for a range of equivalence ratio from 0.8 to 1.4. The methane/air flames were stabilized in a high pressure environment with zero net heat loss. Comparisons with several literature sources (experiments) show good agreement at atmospheric and elevated pressure. From literature it was concluded that many of the pressure-laminar burning velocity correlations reported used stretched laminar burning velocity results and show wide discrepancies. Based on the present burning velocity measurements, power-law pressure dependence for equivalence ratio from 0.8 to 1.4 are presented and analyzed. Correlations from numerical simulations using two widely used chemical reaction mechanisms, GRI Mech 3.0 and USC Mech II are also presented and compared. The mechanisms exhibit very similar trends as the experiments, indicating that the new power exponent β_1 narrow down the earlier scatter in the literature to a more reliable range. The proposed power exponent β_1 shows a non-monotonic behaviour at equivalence ratio around 1.4 in experiments and simulations. Through species and reaction flux analysis it was observed that CH_3 consumption through various reactions remain pressure dependent and show non-monotonic behaviour at equivalence ratio around 1.4. Further measurements were performed for ethane - air and propane - air mixtures for equivalence ratio from 0.8 to 1.3 for pressures up to 4 atm. Correlations for laminar burning velocity determination are provided for both the mixtures.

CHAPTER 6

Experimental Results: Syngas Mixtures (H_2/CO/N_2)

This chapter is dedicated to presenting the results from laminar burning velocity experiments for syngas and H_2-rich syngas at elevated pressure. In the present study, the end goal is to develop an improved kinetic mechanism that is appropriate in predicting lean syngas combustion at high pressure. In doing so, such a mechanism will be validated against experimental results obtained by the heat flux method and by other experiments from the literature (using different methods). The description of the improved kinetic scheme is discussed in chapter 7. [1]

6.1 Syngas Combustion

Experimental data (S_L) for lean syngas/H_2-rich syngas mixtures at elevated pressure are scarce in literature. In the recent work of Sun et al. [7] high pressure laminar flame speed measurements are reported to validate a chemical reaction mechanism for H_2-CO mixtures using a dual-chamber apparatus that

[1] *The results shown in this chapter have been published by Goswami et al., International Journal of Hydrogen Energy 39 (2014) 1485-1498.*

generates an outwardly propagating premixed flame. The experiments were however, reported mostly for rich mixtures with 1% H_2 to 50 % H_2 in the fuel mixture. A study of Natarajan et al. [1] uses a conical flame for determining S_L at elevated pressure and temperature for similar fuel mixtures. Burke et al. [4] used the outwardly propagating flame technique to detemine mass burning rates for 50 % and 10 % H_2 in the H_2-CO fuel mixture with an equivalence ratio of 2.5. In the most recent work of Krejci et al. [76] and Kéromnès et al. [77], constant volume cylindrical vessels are used to determine S_L of H_2-CO mixtures. The reported results are mostly for 50 % and higher CO concentration in the fuel mixture.

The heat flux method was initially applied to CH_4-air flames up to 5 atm [5] as discussed in the previous chapter. The results agreed well with reported data available in the literature. To proceed with H_2-CO mixtures, a number of additions had to be made in order to ensure accuracy and safe working environment. Since these mixtures contained CO, special attention was paid towards the safety aspects including a detection system and well tested high pressure lines. In addition, a special N_2-flushing line was introduced to keep the fuel line flushed when not in use. This ensured that no harmful gases could leak into the laboratory. In addition to this, it was also observed that CO when stored in iron or nickel based cylinders or stainless steel flow lines, some of the gas converts into compounds like carbonyls [22]. When the mixture is lighted, the flame emits a pale, off-white color. This indicates that the mixture is not pure anymore. Hence, special care was taken to install brass and copper lines. High purity of the gases was ensured before the experiments. It was also ensured that all the components could withstand pressures as high as at least 10 bar. Mass flow controllers were calibrated before performing experiments.

Experiments were focused on 50:50 % H_2-CO, 85:15% H_2-CO and 85:15% H_2-N_2 mixtures. In industrial conditions, these mixtures are burnt with air. This results in very high burning velocity. However, the heat flux method is best operational with a burning velocity not higher than 80 cm/s with the dimensions of the plate perforations mentioned in chapter 3 [23]. With flows higher than 80 cm/s, the flame may not be flat anymore. The outlet length of unburnt gas mixture individual jets increases and creates curved flames. This effect is likely to increase even at elevated pressure since length scales decrease. The burner plate hole diameter and the distance between the holes play an important role and has been reduced for that matter [23]. Furthermore, the oxidizers are diluted with inert gases to obtain lower burning velocity which suits the burner plate used in the experiments. Table 6.1 summarizes all the experiments that were performed for the present work. The error involved in these experiments

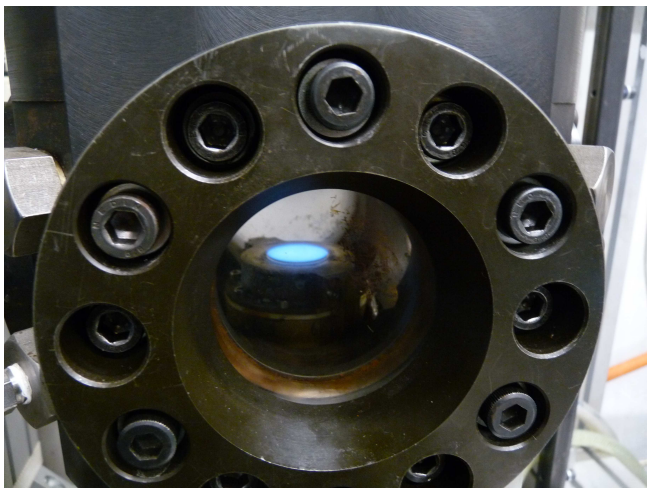

Figure 6.1. A typical H_2-CO flame in a high pressure environment.

are listed in appendix A.

Table 6.1. Measurement conditions for syngas/H_2-rich syngas mixtures.

Fuel	H_2-CO (50:50 %)	H_2-CO (85:15 %)	H_2-N_2 (85:15 %)
Oxidizer	Air O_2/N_2 (15:85 %) O_2/N_2 (10:90 %) O_2/He (10:90 %) O_2/He (12.5:87.5 %)	 O_2/N_2 (15:85 %) O_2/He (12:88 %)	 O_2/He (12.5:87.5 %)
ϕ	0.6 - 1.0	0.5-0.7	0.5
T (°C)	25	25	25
P (atm)	1 - 9	1 - 10	1 - 10

Figure 6.1 shows a flame enclosed in the high pressure system. A flame from the heat flux method is one-dimensional and does not exhibit any kind of instability/disturbance. Initially, the burner head was heated with an electrical heater [5]. With each experiment, special attention was paid to ensure proper conduction of heat from the heater to the burner head. In the absence of proper conduction, acoustical instabilities were observed in the flame. Therefore, a new burner design was proposed and implemented in the present experiments where the electrical heater was replaced by water bath heater which ensured better

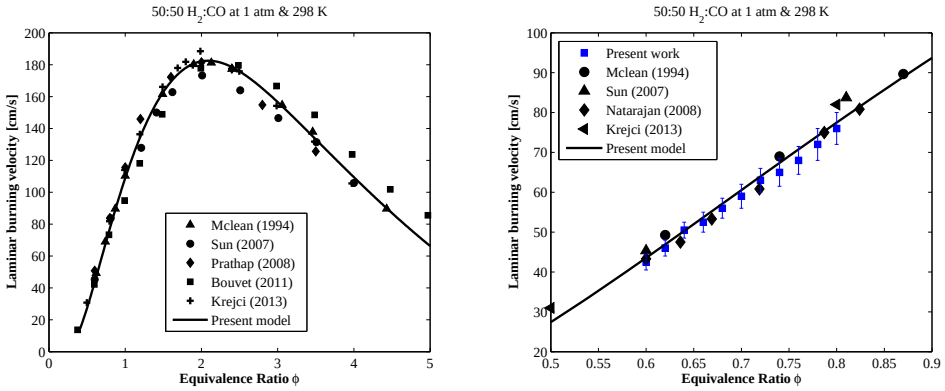

Figure 6.2. Laminar burning velocity of 50:50 % H_2-CO/Air mixture at atmospheric pressure and 298 K. (Left) Symbols: Experimental data from literature [78, 7, 79, 80, 76]; (Right) Symbols: Experiments from present work and literature [78, 7, 1, 76] Line: Simulation using present model

heat conduction.

6.2 Experimental Results

H_2-CO mixtures were introduced to the heat flux method system first at atmospheric conditions. Figure 6.2 (left) shows the variation of laminar burning velocity of 50:50 % H_2-CO and air mixture at 1 atm for a wide range of equivalence ratios (0.5 to 5). Experimental results are from [78, 7, 79, 80, 76]. Using a close-up view of the lean side of the mixture, results from the present work is shown in figure 6.2 (right). The results are well in agreement with the literature data [78, 7, 1, 76].

For pressures greater than 4 atm, the flame with the O_2-N_2 oxidizer shows cellular/structural instabilities due thermo-diffusive and hydrodynamic instabilities (see figure 6.3 (left)). Due to the low mixture Lewis number, the flame exhibits such a behaviour at higher pressure. A similar behaviour has been reported by Natarajan et al. [1] and Sun et al. [7].

The experimental results reported in figures 6.4 - 6.8 show a decrease in laminar burning velocity with the increase in pressure. Figure 6.4 (left) depicts the results of 50:50 % H_2-CO flames for pressures up to 5 atm with diluted oxidizers. With similar concentration of O_2 in both oxidizers and leaner mixtures of O_2-He, large differences are noticed in the laminar burning velocity. Diluent impact

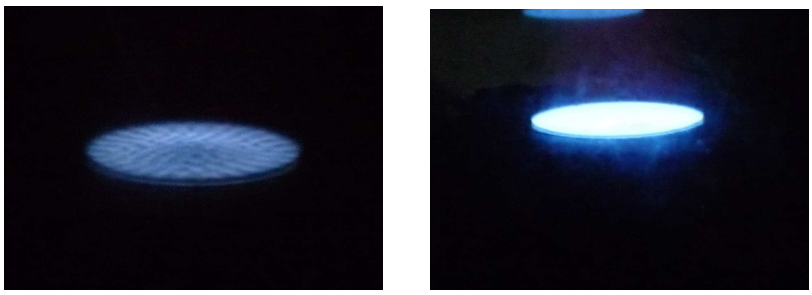

Figure 6.3. (Left) Structural instability in 50:50 % H_2-CO flame with O_2-N_2 at 5 atm. (Right) 50:50 % H_2-CO flame with O_2-He at 8.5 atm and ϕ=0.6.

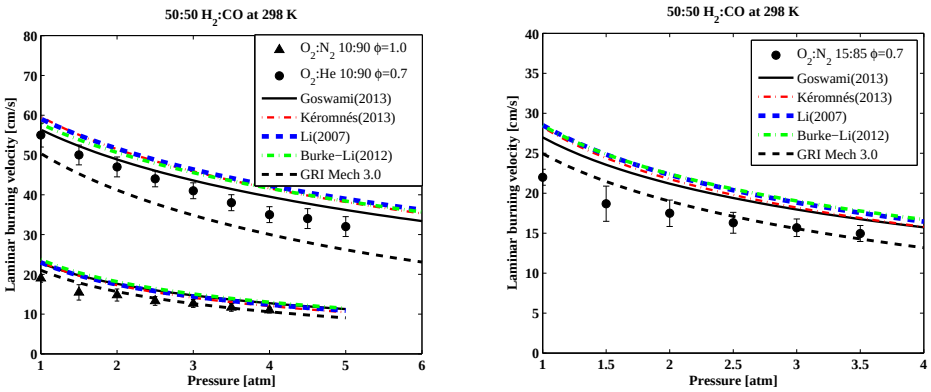

Figure 6.4. Laminar burning velocity of 50:50 % H_2-CO mixture. (Left) Symbols: Experiments- Triangles: with O_2-N_2 (10 % O_2) at $\phi = 1.0$ and Circles: O_2-He (10 % O_2) at $\phi = 0.7$. (Right) Symbols: experiments- O_2-N_2 (15 % O_2) at $\phi = 0.7$. Lines: Simulation using present model (black), Li et al. [82] (blue), Kéromnès et al. [77] (red), Burke et al. [83] (green) and GRI Mech 3.0 [27] (dashed black).

on laminar burning velocity has been well described by Galmiche et al. [81]. A lower heat capacity and resulting higher thermal diffusivity of helium compared to nitrogen results in higher laminar burning velocities. Laminar burning velocity of 50:50 % H_2-CO and 15:85 % O_2-N_2 for pressure up to 4 atm and $\phi = 0.7$ are shown in figure 6.4 (right).

With time these experiments were repeated to gain experience and stability in operation. Since it was observed that the most stable and flat flames were obtained with O_2-He oxidizer, the rest of the measurements were carried out at different proportions of this oxidizer. Moreover, the objective of the experiment was to reach lean conditions so as to validate the proposed kinetic scheme.

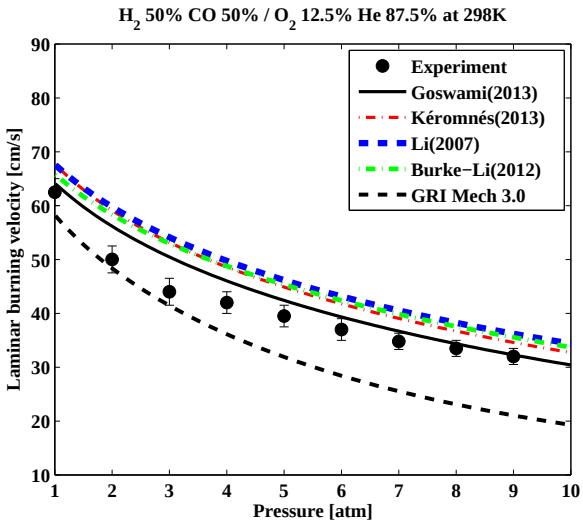

Figure 6.5. Laminar burning velocity of 50:50 % H_2-CO mixture with O_2-He (12.5 % O_2) at $\phi = 0.6$. Symbols: Experiments. Lines: Simulations - present model (black), Li et al. [82] (blue), Kéromnès et al. [77] (red), Burke et al. [83] (green) and GRI Mech 3.0 [27] (dashed black).

With an oxidizer mixture of 12.5 % O_2 and the rest being helium, 50:50 % H_2-CO flame were obtained at $\phi = 0.6$ up to a pressure of 9 atm as shown in figure 6.5. The picture in figure 6.3 (right) shows a 50:50 % H_2-CO flame at 8.5 atm in a slightly super adiabatic state. The flames were highly sensitive to variations in velocity/heat flux as the pressure was increased. Change in gas velocity by 1 - 1.5 cm/s from the adiabatic state showed non-flat structures (super adiabatic) or moved closer to the burner plate, thereby increasing the plate temperature (sub adiabatic) considerably.

Figures 6.6 and 6.7 show laminar burning velocity results of 85:15 % H_2-CO flames. During these measurements an equivalence ratio of 0.5 was achieved with O_2-He oxidizer mixture up to a pressure of 10 atm.

The continuous black line in the above comparisons (figures 6.2, 6.4 - 6.8) represents the predictions of the proposed model [84]. The details of the model are discussed in the following chapter. The CHEM1D laminar flame code is used to simulate these 1-D flames. A brief description of this code is also given in Chapter 7. Recent models from literature are also presented for comparison [82, 77]. Model prediction using the proposed kinetic scheme in the present work agree well with the experimentally determined results. Models from Li et

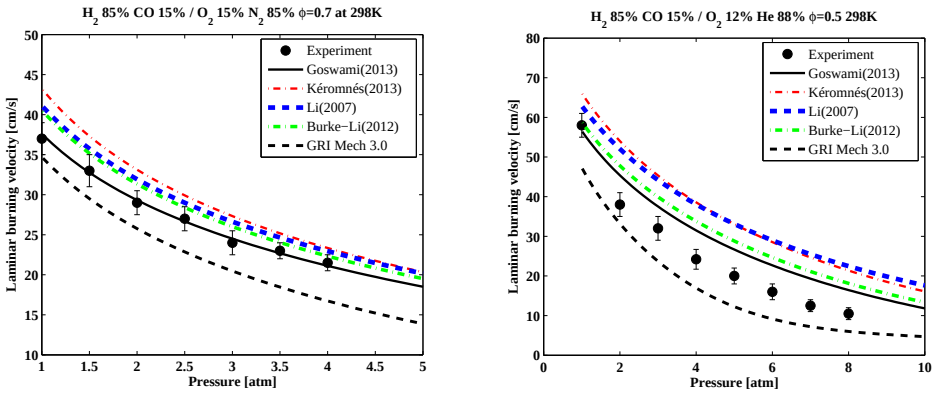

Figure 6.6. (Laminar burning velocity of 85:15 % H_2-CO mixture with (Left) O_2-N_2 (15 % O_2) at $\phi = 0.7$. (Right) O_2-He (12 % O_2) at $\phi = 0.5$. Symbols: Experiments. Lines: Simulations - present model (black), Li et al. [82] (blue), Kéromnès et al. [77] (red), Burke et al. [83] (green) and GRI Mech 3.0 [27] (dashed black).

al. [82] and Kéromnès et al. [77], in general, over-predict the measured results, more evidently for 85:15 % H_2-CO mixtures. For the same mixture at $\phi = 0.5$ (figure 6.6 (right)), the models from the literature over-predict S_L by 20 cm/s. The proposed model shows better agreement even though a difference of ~ 6 cm/s still exists. This difference can be attributed to the uncertainties in the kinetic model. The subsequent sections discuss the proposed kinetic model and comparisons with experimental data from literature.

Figure 6.7 (left) depicts the variation of S_L of 85:15% H_2-CO (burnt with 11:89% O_2-He) with pressure obtained experimentally up to 5 atm and equivalence ratio (ϕ) of 0.6. The comparison with the mechanisms reveal that the models over-predict the experiments except GRI Mech 3.0 which under-predicts all the experiments. Similar trend of under-prediction by GRI Mech 3.0 was also observed recently by Burke et al. [4]. The reason for the disparity of GRI Mech 3.0 in this case is obvious since the optimization of this mechanism was specifically done for natural gas mixtures and not for syngas mixtures. A kinetic study by Burke et al. [85] also demonstrated the substantial impact of H_2/O_2 subset of GRI Mech 3.0 when compared to the subset provided by Davis et al. [86] for predictions at elevated pressures.

Qualitatively, the mechanisms from Goswami et al. [84] and Burke et al. [83] predict better than others. Similar predictions are observed in figure 6.7 (left) and 6.8 where H_2-CO and H_2-N_2 mixtures are burnt in O_2-He (12.5% O_2) at $\phi = 0.5$ and initial temperature of 298 K up to a pressure of 10 atm. The

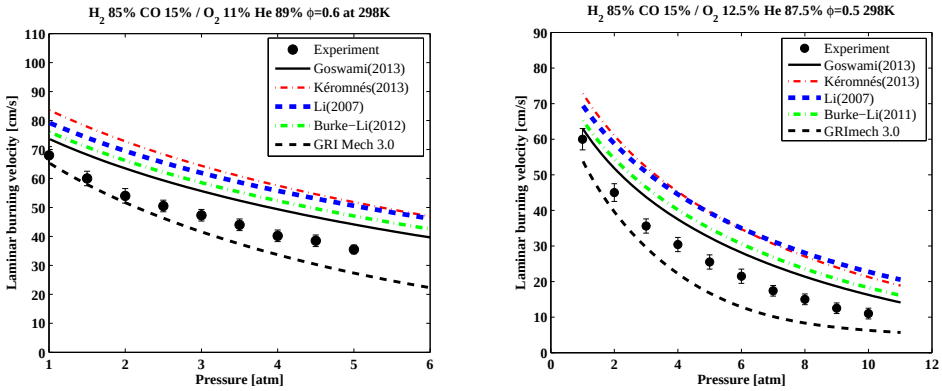

Figure 6.7. Laminar burning velocity of 85:15 % H_2-CO (Left) O_2-He (11 % O_2) at $\phi = 0.6$ (Right) O_2-He (12.5 % O_2) at $\phi = 0.5$. Symbols: Experiments. Lines: Simulations - present model (black), Li et al. [82] (blue), Kéromnès et al. [77] (red), Burke et al. [83] (green) and GRI Mech 3.0 [27] (dashed black).

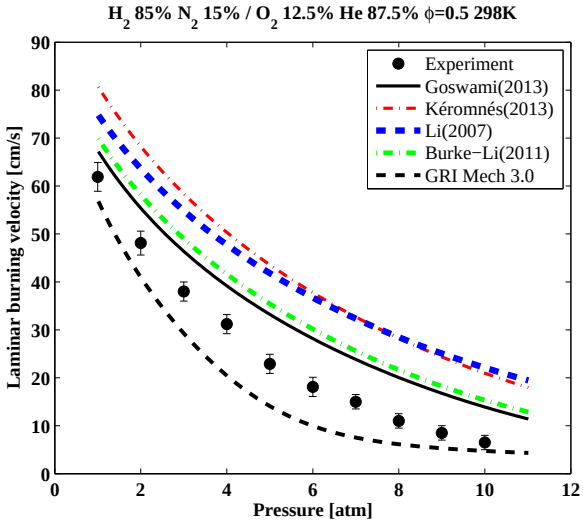

Figure 6.8. Laminar burning velocity of 85:15 % H_2-N_2 with O_2-He (12.5 % O_2) at $\phi = 0.5$. Symbols: Experiments. Lines: Simulations - present model (black), Li et al. [82] (blue), Kéromnès et al. [77] (red), Burke et al. [83] (green) and GRI Mech 3.0 [27] (dashed black).

adiabatic flame temperature calculated using CHEM1D is around 1500 K for the former mixture. The burning velocities obtained for N_2 diluted mixture are lower than the CO added mixture as expected. It is noteworthy, at this point, that the chemical reaction mechanisms used in the present work and available in the most recent literature are not sufficient in predicting such lean high-H_2 syngas mixtures burning velocities. This suggests a further analysis of the reactions involved in such combustion processes. This discussion is made available in the following chapter.

6.3 General Discussion

The effect of pressure on flames is the main objective of this study. From numerical and experimental point of view, many observations with laminar burning velocity were made for varying pressures. Chapters 3, 5 and 6 discuss the effect of pressure varying conditions of equivalence ratio, fuel mixtures and oxidizer compositions. It is interesting to note that the flames exhibit this dependence and therefore in this section, an attempt is made to consolidate such observations. Flames experience many effects once it is subjected to elevated pressure. The increase in densities and rise in burning rates make the combustion process rapid with higher heat release. Due to higher collision rates between molecules the reaction zone begins to thin down. More pronounced effects of diffusion and flow are observed. Lean mixtures of fuels like H_2 when burnt in air experience structural instabilities due to low mixture Lewis number. The Lewis number defines the effect of thermal diffusivity and mass diffusivity of a mixture. With the increase in pressure, the hydrodynamic instabilities are significant since diffusive-thermal effects weaken. In the present study, experiments using the heat flux method were successful from atmospheric pressure to 10 atm. The stabilization of syngas flames with high amount of H_2 was challenging at high pressure for a number of reasons. These flames were diluted with N_2/He in order to reduce the burning velocities. The most important condition of interest was to follow the flame at $\phi = 0.5$ since this condition was not reported in the literature. At 10 atm, the velocities were close to 5-10 cm/s which was very low to continue for even higher pressure.

The advantages of having an adiabatic flat and stretchless flame contributes a lot to this method. From chapter 3, one can conclude that the burner plate dimensions play an important role in stabilizing a flat flame. In the high pressure experiments involving syngas mixtures it was noticed that the plate temperatures were sensitive enough to change in gas velocities (parabolic temperature

profiles were seen). This indicates the uniformity of the flame. In case of lower alkane-air mixtures, where the flame temperatures were high (around 2200 K), stabilizing high pressure flames beyond 5 atm was difficult. This effect can be attributed to the dimensions of the current burner plate. In the future, an interesting study can be to introduce a plate with smaller hole diameter and higher porosity and study the flame at higher pressures. In the present analysis of error estimations of the high pressure experiments it was concluded that the uncertainties decrease with increase in pressure. The contributing parameters for error in the measurements are as follows:

- Flow rates: At higher pressures, the burning rates are higher and therefore the flow rates are high. Hence, uncertainties in the MFCs are higher at higher pressure.
- Equivalence ratio: The relative error in ϕ is given by the sum of relative errors from each mass flow controller.
- Pressure: The accuracy of the pressure sensor determines the uncertainty in the chamber pressure. As the pressure was increased, the error due to pressure decreases. The pressure sensor used in HPHFM-II was more accurate than the one in HPHFM-I.
- Temperature: This component does not change for these experiments as the unburnt gas mixture is always maintained at 298 K.
- Unburnt gas velocity: This error is calculated by the contribution of flow rates, pressure, temperature and area. The effective error decreased with increase in pressure.
- Scatter in thermocouples: The thermocouples show higher sensitivity at high pressures. With increase in pressure, flames experience higher heat release. The plate temperature profile was therefore more sensitive to such flames. This reduced the scatter in thermocouples.

Summary

Stretchless adiabatic laminar burning velocities are determined for lean syngas (50:50 % H_2-CO, 85:15 % H_2-CO and 85:15 % H_2-N_2) mixtures in combination with a variety of oxidizer compositions using the heat flux method. Experiments at atmospheric pressure agreed well with recent results from literature. Experimental results were obtained for pressures up to 10 atm and initial temperature of 298 K for a range of equivalence ratios from 0.5 to 1 at 298 K. An updated H_2-CO kinetic scheme is proposed (in the next chapter) that includes recently

evaluated rate constants from literature. Model validation is performed using results from present experiments at atmospheric and elevated pressure.

CHAPTER 7

Chemical Reaction Mechanism for Syngas Mixtures

Chemical kinetics is the branch of chemistry that deals with rate of chemical reactions. In combustion modeling one of the most important input is the chemical reaction mechanism or kinetic scheme. A kinetic scheme lists all the important chemical reactions involved in the combustion process of a fuel. The species conservation equation (also discussed in chapter 3 given by equation 3.4) requires the details of the rate of each reaction based on which the simulation proceeds. In this chapter, a chemical reaction mechanism is presented for syngas mixtures that perform well at atmospheric and elevated pressures. The comparison of this scheme with experimental results from this thesis are presented in the previous chapter. [1]

7.1 Chemical Reaction Mechanism

The rate of the reaction $\mathrm{k_r}$ is defined by the modified Arrhenius equation given by

[1] *The results shown in this chapter have been published by Goswami et al., International Journal of Hydrogen Energy 39 (2014) 1485-1498.*

$$k_r = A_p T^n \exp(-E_a/RT), \tag{7.1}$$

where A_p, n and E_a are temperature dependent rate parameters, T is the temperature and R is the gas constant. A detailed description of rate law, reaction order, temperature and pressure dependence of rate coefficients can be found in the thesis of Heghes¸ [87]. A standard format called the CHEMKIN format is followed internationally to define kinetic scheme files. In this chapter, the original mechanism of Konnov [88] is updated with a few new rate constants suggested in the literature. The CO sub-mechanism is added from the version 0.6 of Konnov [28]. The new proposed mechanism is specially validated against high pressure experimental data obtained and reported in the previous chapter. Readers are requested to refer back to chapter 6 for comparisons of the proposed model (also referred as Goswami(2013)) with four mechanisms reported in the literature. The details of the present kinetic model is presented in this chapter.

7.2 Literature Review

Substantial progress is made in accurate determination of elementary reaction rates and thermodynamic properties as well as in the measurement of the integral combustion characteristics such as burning velocities and ignition delays. This has stimulated the development of several detailed kinetic mechanisms for the combustion of hydrogen and carbon monoxide mixtures [86, 89, 90, 82]. Davis et al. [86] used the H_2-CO sub-mechanism of the GRImech 3.0 as a starting point and demonstrated that the optimization of this model can bring very good agreement with the experiments chosen as targets. However, the authors did not include self-reactions between HCO radicals which act as chain-termination in HCO + HCO = CH_2O + CO and HCO + HCO = CO + CO + H_2. If these missing reactions have sensitivities comparable with reactions which are present in the model of Davis et al. [86], then the rate constants derived during optimization of the incomplete reaction set could be misleading. The mechanism was further refined by Sivaramakrishnan et al. [91] to improve its agreement with oxidation experiments at intermediate temperatures and very high pressures. Zsely et al. [89] revised the H_2-CO reaction set of the Leeds methane oxidation mechanism [92] using the latest CEC evaluations [93]. Particular attention in the work of Zsely et al. [89] was paid to the uncertainties of the modeling caused by the uncertainties in the rate constants. Updates of the H_2-CO sub-mechanism were made by Saxena and Williams [90] and good agreement of the modeling with laminar burning velocities and igni-

tion delay mostly at atmospheric pressures was demonstrated. Li et al. [82] presented detailed kinetic mechanism for CO, CH_2O, and CH_3OH combustion which included their H_2/O_2 sub-mechanism [94]. They recommended two new rate constants for H_2-CO sub-mechanism. Sun et al. [7] developed an updated kinetic mechanism meant to predict flame speeds at higher pressure with the modification in one of the reaction rate constants.

Saxena and Williams [90] restricted the range of applicability of their model to temperatures above 1000 K. The range of experimental conditions covered by the mechanism of Li et al. [82] was stated as from 298 to 3000 K. This does not mean, however, that this model is applicable at low temperatures encountered at atmospheric chemistry of H_2-CO system. For example, the effect of pressure on the key reaction between CO and OH, well established at low temperatures was not present in the combustion mechanisms cited above. Sivaramakrishnan et al. [91] argued that the addition of a high pressure channel forming HOCO adduct followed by its subsequent decomposition to CO_2 + H, could not improve the agreement of their modeling with experiments performed in the range from 1000 to 1500 K. On the other hand, Fulle et al. [95] demonstrated that at 819 K, the pressure dependence of the reaction between CO and OH becomes notable at about 10 atm and higher. The lowest temperature accessible in experiments on syngas ignition was about 600 K [96]. Correct modeling of these experiments therefore requires incorporation of the pressure-dependent rate constant forming HOCO adduct. Moreover, the chemistry of H_2-CO oxidation is the core of any detailed reaction mechanism for combustion modeling including those developed for self-ignition and oxidation of hydrocarbons at intermediate ($\sim$ 600 K and higher) temperatures. This means that proper extension of the H_2-CO oxidation mechanism down to these temperatures requires bridging a gap between combustion and atmospheric chemistry.

The most recent experimental data from literature suggest that the recent kinetic mechanisms for H_2-CO combustion require modification. Natarajan et al. [1] performed a study that included measurement of laminar flame speeds of H_2-CO mixtures at elevated pressures, preheat temperatures and lean conditions that are relevant to gas turbine combustors. Over prediction of the temperature dependence of the flame speed for medium and high H_2 content syngas was reported for mechanisms by Davis et al. [86] and Li et al. [82] at very lean conditions. This effect is higher at atmospheric pressure than at high pressures. They cited that errors might be due to the 'low temperature' reactions that become important when temperatures of unburnt gases are increased. Burke et al. [4, 85] performed various experiments on $H_2/CO/O_2$/diluents fuels for wide range of equivalence ratio, flame temperatures and pressure. Disagreement

with model predictions of many mechanisms [86, 90, 88, 7, 82, 27, 64, 97] was reported. A modification to several rate constants of reactions in H_2 mechanism is suggested and published recently [83].

Among the recent work in analyzing ignition delay times predicted using kinetic models is from Mittal et al. [98] where experimental data from rapid compression machine for higher pressures (up to 50 bar) and temperature range of 950 to 1100 K was used in evaluating the mechanism by Davis et al. [86]. They reported discrepancy in the predictions and recommended revision of the rate constant of CO + HO_2 reaction. With a modification in the rate constant of the same reaction, Walton et al. [99] compared experimental data to the modified version of the mechanism by Davis et al.[86] and reported good agreement but emphasizes that it overpredicts the activation energy. The difference was attributed to the large uncertainty involved in the above reaction. Sivaramakrishnan et al. [91] performed experiments on shock tube for pressure 21-500 bar and temperature range of 1000-1500 K for stoichiometric and lean H_2-CO mixtures. Peterson et al. [96] analyzed ignition delay data and showed that at lower temperatures models do not match experiments to a large extent and reported that the differences remain more at lower temperatures than at higher pressures. Recent work of Krejci et al. [76] presents ignition delay and burning velocity measurements at elevated pressure and temperature. It was reported that at low temperatures and high pressure (more than 12 atm) ignition delay time does not change with an increase in CO in the H_2-CO mixture. An updated version of the O'Connaire mechanism [97] is made available by Keromnes et al. [77] with the inclusion of CO subset and few modifications in H_2 subset. The model is validated with a number of shock tube and rapid compression machine experiments at high pressure. This mechanism is used for comparisons in the present work.

7.3 Kinetic Modeling

The in-house laminar code CHEM1D [19] was used for modeling a 1-dimensional free flame for the determination of the flame temperatures and laminar burning velocity. CHEM1D (described in appendix B) solves a set of equations describing the conservation of mass, momentum, energy and chemical components for chemically reacting flows. It uses an exponential finite-volume discretization in space and non-linear differential equations are solved with a fully implicit, modified Newton method along with a complex transport model. An adaptive gridding procedure is also implemented to increase accuracy in the flame

front by placing almost 80% of the grid points in the area with the largest gradients. Thermodynamic data used are all from the database of Burcat and Ruscic [100]. The governing equations and numerical scheme is explained in the following section.

Many studies have been conducted in the past to analyze the hydrogen flame structure and kinetic pathways (section 7.2). Reaction numbering corresponds to the list given in Table 7.1 which outlines the chemical scheme proposed in the present work. It is known that CO - O_2 mixtures without hydrogen-containing additives react very slowly since oxidation includes only two steps CO + O_2 = CO_2 + O (25) and CO + O (+M) = CO_2 (+M) (22). In the presence of traces of hydrogen, water or hydrocarbons, the chain process develops fast with participation of H, OH, and HO_2 radicals and the CO oxidation proceeds mainly through reactions CO + OH = CO_2 + H (23) and CO + HO_2 = CO_2 + OH (26). With 50 % CO or less in the fuel mixture, the process is dominated by hydrogen chemistry. In such a case, the consumption of H, OH and HO_2 show a large influence especially at elevated pressure [4]. The original Konnov mechanism [88] is tested at elevated pressures in a few studies and reported insufficient [4, 85]. The mechanism is updated in the present work with some modifications, taking into account recently evaluated kinetic data for combustion modeling. The CO reaction set is included from Konnov 0.6 version [28] for hydrocarbons with few modifications which are discussed later in this section. Reaction flux, species flux and sensitivity analysis of lean H_2-CO mixtures were performed using the proposed kinetic model at elevated pressure to identify important reactions.

Figure 7.1 represents the rate of important reactions in H_2-CO chemistry in the lean regime through a combustion process at different pressures and H_2 addition. The plots come in assistance in representing the competing pathways for high pressure kinetics of the chain branching reaction H + O_2 = OH + O (8) and the pressure dependent reaction H + O_2 (+M) = HO_2 (+M) (5) at ϕ = 0.5 and adiabatic flame temperature of 1500 K at pressure 1, 5 and 10 atm for different H_2-CO mixtures. Reaction 8 moves ahead of 5 with an increase in H_2 concentration in the fuel mixture at atmospheric pressure, however, not considerably. With an increase in pressure, HO_2 production is found to be important in all cases. The fuel mixture without CO concentration sees highest HO_2 production due to higher availability of H_2O as the third body.

HO_2 radical fraction changes steep gradients as suggested by figure 7.2 with pressure (1, 5 and 10 atm at ϕ = 0.5 and adiabatic flame temperature, T_f of 1500 K). The rate constants of both reaction 5 and 8 need proper treat-

Table 7.1. Reactions and rate constants of the proposed H_2/CO kinetic mechanism, $k_r = A_p T^n \exp(-E_a/RT)$. Units in cm^3 mol s cal K.

No.	Reaction	A_p	n	E_A	Reference
1a	H+H+M=H_2+M	7.00E+17	-1.0	0	[101]
	H_2/0.0/ N_2/0.0/ H/0.0/H_2O/14.3/ CO/3.0/ CO_2/3.0/				
1b	H+H+H_2=H_2+H_2	1.00E+17	-0.6	0	[101]
1c	H+H+N_2=H_2+N_2	5.40E+18	-1.3	0	[101]
1d	H+H+H=H_2+H	3.200E+15	0.0	0	[101]
2	O+O+M=O_2+M	1.000E+17	-1.0	0	[102]
	O/28.8/ O_2/8.0/ N_2/2.0/H_2O/5.0/				
3	O+H+M=OH+M	6.75E+18	-1.0	0	[103]
	H_2O/5.0/				
4a	H_2O+M=H+OH+M	6.06E+27	-3.312	120770	[1]
	H_2O /0/ H_2/3/ N_2 /2/O_2 /1.5/ CO_2 /4/				
4b	H_2O+H_2O=H+OH+H_2O	1.00E+26	-2.44	120160	[1]
5a	H+O_2(+M)=HO_2(+M)	4.66E+12	0.44	0	[104]
	LOW /5.70E+19 -1.4 0/				
	TROE /0.5 100000 10/				
	H_2O/0.0/ O_2/0.0/ H_2/1.5/CO_2/2.4/ He/1.0/ Ar/0.0/				
5b	H+O_2(+Ar)=HO_2(+Ar)	4.66E+12	0.44	0	[104]
	LOW /7.43E+18 -1.2 0/				
	TROE /0.5 10 100000/				
5c	H+O_2(+O_2)=HO_2(+O_2)	4.660E+12	0.44	0	[104]
	LOW /5.69E+18 -1.094 0/				
	TROE /0.5 100000 10/				
5d	H+O_2(+H_2O)=HO_2(+H_2O)	9.060E+12	0.2	0	[105]
	LOW /3.67E+19 -1.0 0/				
	TROE /0.8 10 100000/				

No.	Reaction	A	n	E_A	Reference
6a	OH+OH(+M)=H_2O_2(+M)	1.00E+14	-0.37	0	[88, 93]
	LOW /2.38E+19 -0.8 0 /				
	TROE /0.5 100000 10/				
	H_2O/0.0/				
6b	OH+OH(+H_2O)=H_2O_2(+H_2O)	1.00E+14	-0.37	0	[106, 93]
	LOW /1.45E+18 0.0 0/				
	TROE /0.5 100000 10/				
7	O+H_2=OH+H	3.82E+12	0.0	7948	[93]
		+8.79E+14	0.0	19170	
8	H+O_2=OH+O	1.04E+14	0.0	15286	[107]
9	H_2+OH=H_2O+H	2.14E+08	1.52	3450	[93]
10	OH+OH=H_2O+O	3.34E+04	2.42	-1930	[93]
11	HO_2+O=OH+O_2	1.63E+13	0.0	-445	[108]
12	H+HO_2=OH+OH	7.08E+13	0.0	295	[109]
13	H+HO_2=H_2+O_2	1.66E+13	0.0	823	[109]
14	H+HO_2=H_2O+O	1.45E+12	0.0	0	[93]
15	H_2+O_2=OH+OH	2.04E+12	0.44	69155	[110]
16	HO_2+OH=H_2O+O_2	2.89E13	0.0	-500	[93]
		+9.27E+15	0.0	17500	
17a	HO_2+HO_2=H_2O_2+O_2	1.03E+14	0.0	11040	[111]
		+1.94E+11	0.0	-1409	
17b	HO_2+HO_2(+M)=H_2O_2+O_2+M	6.84E+14	0.0	-1950	[112]
18	H_2O_2+H=HO_2+H_2	1.70E+12	0.0	3755	[93]
19	H_2O_2+H=H_2O+OH	1.00E+13	0.0	3575	[93]
20	H_2O_2+O=HO_2+OH	9.55E+6	2.0	3970	[113]
21	H_2O_2+OH=HO_2+H_2O	2.00E+12	0.0	427	[114]
		+1.70E+18	0.0	29400	

No.	Reaction	A	n	E_A	Reference
22	CO+O(+M)=CO_2(+M)	1.80E+10	0.0	2384	[115]
	LOW /1.55E+24 -2.79 4190/				
	H_2/2.5/ H_2O/12/ CO/1.9/CO_2/3.8/ Ar/0.87/				
23	CO+OH=CO_2+H	2.23E+05	1.90	-1160	[82]
24	CO+OH(+M)=HOCO(+M)	1.20E+07	1.83	-236	[116]
	LOW /7.20E+25 -3.85 1550.0/				
	TROE/0.6 10.0 100000.0/				
	H_2/2.5/ H_2O/12/ CO/1.9/CO_2/3.8/ Ar/0.87/				
25	CO+O_2=CO_2+O	2.50E+12	0.0	47800	[102]
26	CO+HO_2=CO_2+OH	1.15E+05	2.278	17545	[7]
27	HCO+M=H+CO+M	4.80E+13	0.0	15760	[106]
	H_2/2.5/ H_2O/6.2/ CO/1.875/CO_2/3.75/ Ar/1.0/				
28	HCO+H=CO+H_2	9.00E+13	0.0	0	[106]
29	HCO+O=CO+OH	3.00E+13	0.0	0	[106]
30	HCO+O=CO_2+H	3.00E+13	0.0	0	[106]
31	HCO+OH=CO+H_2O	1.00E+14	0.0	0	[106]
32	HCO+O_2=CO+HO_2	2.71E+10	0.68	-471	[106]
33	HCO+HO_2=CO_2+OH+H	3.00E+13	0.0	0	[113]
34	HCO+HO_2=CO+H_2O_2	3.00E+12	0.0	0	[113]
35	HCO+HCO=CH_2O+CO	2.70E+13	0.0	0	[117]
36	HCO+HCO=H_2+CO+CO	3.00E+12	0.0	0	[113]
37	HOCO(+M)=H+CO_2(+M)	1.74E+12	0.307	32930	[118]
	LOW /2.29E+26 -3.02 35070/				
	H_2/1.5/ H_2O/0.0/ O2/0.0/ Ar/0/				
38	HOCO+OH=H_2O+CO_2	1.60E+13	0.0	560	[119]
39	HOCO+O_2=HO_2+CO_2	1.38E+10	0.842	160	[120]

ment as is suggested in various literature sources (discussed below). Among other competing pathways H + HO_2 set, reaction 12 (H + HO_2 = OH + OH) shows very high contribution in OH production which in turn assists reaction 8. Higher sensitivity of reaction 8 can be attributed to this reason. It has been reported in earlier studies that reaction 8 in all cases remains the most sensitive reaction. The reaction 13 (H + HO_2 = H_2 + O_2) contributes uniformly in all cases when compared to other reactions. Sensitivity of reaction 36, namely CO + OH = CO_2 + H remains high with a gradual decrease in H_2-rich fuel mixtures.

In general, it is apparent from figure 7.3 (left) that all reactions involving H, OH and HO_2 contribute significantly to the performance of the mechanism and the combustion process. The kinetic behavior of mixtures containing a CO mole fraction more than 50 % in the fuel mixture is expected to affect the oxidation of both H_2 and CO. HCO production from various pathways (through H and OH) contribute towards CO oxidation. Higher OH concentration reacts with both CO and H_2 and oxidize to stable species. However, at elevated pressure, HO_2 gets consumed to obtain HCO which in turn oxidizes directly or eventually to CO_2. With lower concentration of CO, this pathway becomes less important. Figure 7.3 (right) presents the sensitivity of laminar burning velocity to the rate of reactions for 85:15% H_2-CO mixture with O_2-He oxidizer (12.5% O_2) for pressure 1, 5 and 10 atm and $\phi = 0.5$. Among the most important reactions is H + O_2 = OH + O (8) which shows high sensitivity to changes in pressure. Reaction O + H_2 = OH + H (7) shows significant sensitivity but remains unaffected by increase in pressure. CO oxidation reaction CO + OH = CO_2 + H (23) also exhibits sensitivity of the order of other important reactions. The present and earlier studies [4] suggest, through flux analysis of species, that reaction H + O_2 (+M) = HO_2 (+M) (5) contributes significantly in the lean mixture regime. The production and consumption of important intermediate species such as H, OH and HO_2 depend on this reaction. The sensitivity increases by 11.5 times from 1 atm to 10 atm which is highest among all the reactions presented in figure 7.3 (right). This reaction is also one of the major heat release reactions in the early part of a H_2 flame [1]. The consumption of H becomes competitive between reactions 5 and 8 as observed [84] when initially 8 is slightly ahead of 5, but eventually, with increase in pressure 5 dominates every reaction that consumes H. The increase in pressure brings along higher densities and collision rates (stronger kinetics) thereby reducing the thickness of the reaction layer. Subsequent production of HO_2 and OH completes the pathway in assisting oxidations processes. Excess of O_2 in a lean mixture makes it also a major contributor in reactions R1 and R3 which suggests more competition.

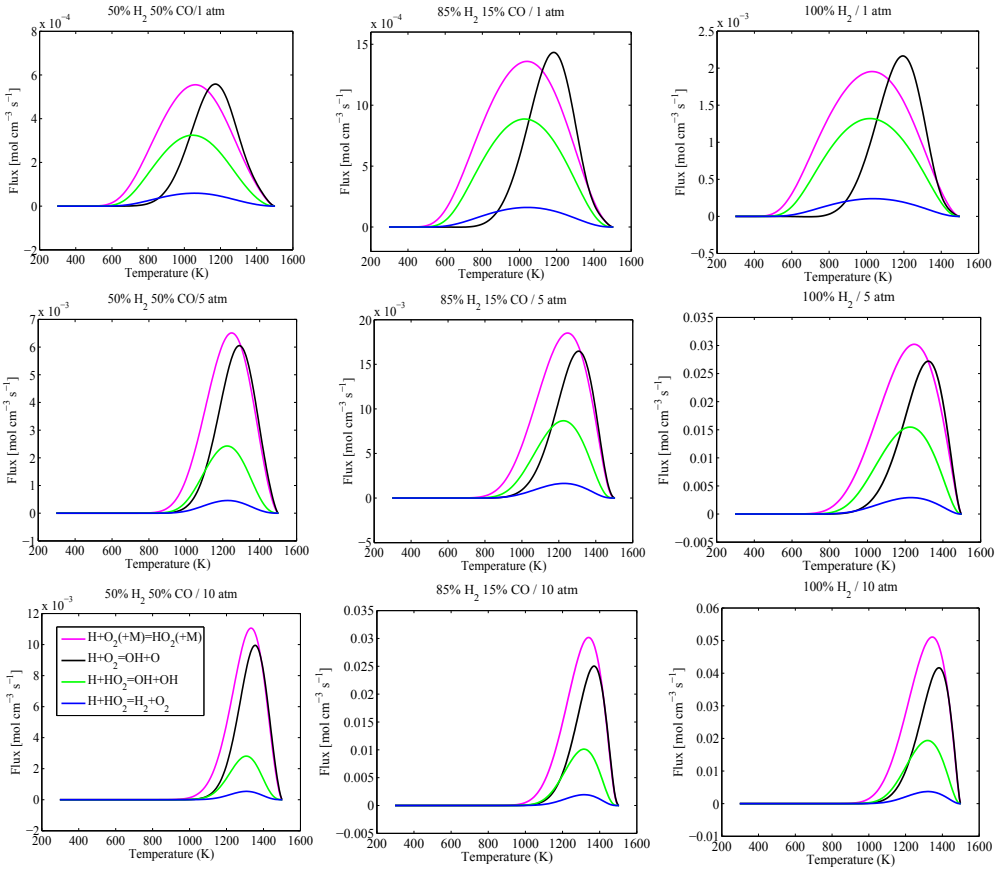

Figure 7.1. Comparison of rate of reactions for $H_2/CO/O_2$/He flames at P = 1, 5, 10 atm , ϕ=0.5 and $T_f \sim$ 1500 K.

The rest of this section outlines the rate constants modified to the original mechanism. In proposing the updated scheme no attempt is made in adjusting the rate constants to fit the experimental data. Adjustment of rate constants to fit experimental data distorts the original fit/derivation proposed for the individual reactions.

From the above analysis it is apparent that further discussion is required in assessing the rate constant for reaction 5, H + O_2 (+M) = HO_2 (+M). In addition to this, the third body efficiencies also play a major role in this reaction. When compared to gases like N_2, Ar and He, the larger molecules such as H_2O and CO_2 are more efficient. Therefore, being one of the most important reactions in $H_2/O_2/CO$ chemistry, a few research studies have been reported in the recent literature. The experimental and modeling studies by

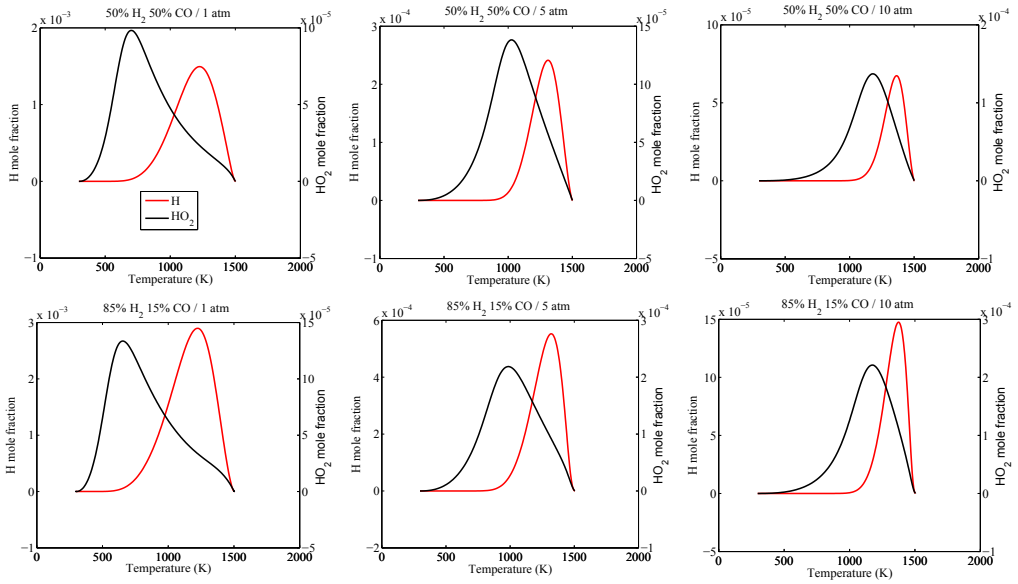

Figure 7.2. Comparison of H and HO_2 mole fraction for $H_2/CO/O_2$/He flames P = 1, 5, 10 atm , ϕ=0.5 and $T_f \sim 1500$ K.

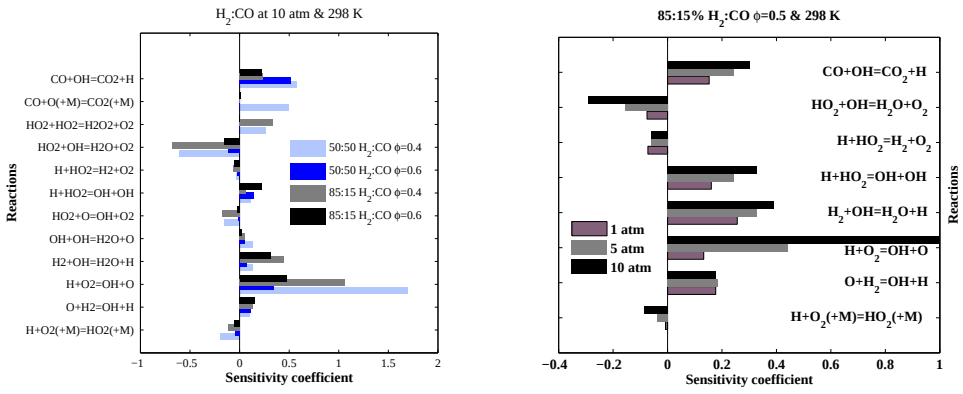

Figure 7.3. Sensitivity of laminar burning velocity of lean (left) 50:50 % and 85:15 % H_2-CO flame to reaction rates at 10 atm and (right) 85:15 % H_2-CO flame at 1, 5 and 10 atm.

Troe [104], Michael et al. [121], Fernandes et al. [122] and Bates et al. [105] have reported rate constants of reaction R1 over a range of 300 - 2000 K. Their recommendations are used in the most recent kinetic models [83, 77, 84] used in the present work. In the work of Burke et al. [4], the authors discuss the range of efficiencies and their uncertainties suggested in the literature. In their subsequent work [83], the rate constant of reaction R1 among others was analyzed and modified according to the recommendations mentioned above. The lean mixtures of pure H_2 (H_2/O_2/He) (0.3 ϕ 0.85) were predicted well. However, the mechanism [83] still shows discrepencies in predicting the experiments reported in the present work shown in chapter 6 (figures 6.4 - 6.8). The recommendations of Troe [104] and Bates et al. [105] are used in the proposed model.

The rate constant of reaction 7, $O + H_2 = OH + H$ has been reviewed a number of times and has been of great experimental interest. Due to its variation at high and low temperature and also its high significance in hydrogen chemistry, the rate constant finds significant importance in the hydrogen mechanism. This reaction is one of the pathways to the formation of OH that in turn gives a path to NO formation through thermal NO_x mechanism. In the work of Baulch et al. [93], a review has been performed ever since 1972 including Cohen and Westberg [101] and Tsang and Hampson [113]. The mechanism of Konnov [88] adopted the rate constant derived by Sutherland et al. [123] which extrapolates even to high temperatures (1700-3500 K). In the present mechanism, a slightly improved value of Baulch et al. [93] is adopted that also fits low temperature data.

The reaction $H + O_2 = OH + O$ (8) signifies chain branching and the production of OH radicals which are of importance to hydrogen combustion and NO_x chemistry. Various experiments have been performed to determine the rate constant of this reaction but only at temperatures greater than 500 K. Low temperature experiments have not been possible resulting in prohibition of consistent results over a sufficiently wide temperature range. Baulch et al. [93] reviewed data from a number of sources, mostly shock tube experiments, for pressure up to 4 bar. In the review, experimental and simulation results of Hwang et al. [124] are highlighted and the rate constant is defined by a non-Arrhenius expression for a temperature range of 950 - 3100 K. A recent study of Hong et al. [107] proposes an Arrhenius fit which has been applied in the present model. The reported rate constant is derived from absorption measurements over a range of 1100 - 3370 K. This recommendation is used in almost all the recent kinetic schemes [83, 77, 84]. This modification improved the capability of these mechanisms which is reported in their respective work.

A number of studies are available for lower temperatures in the literature and hence evaluations of rate constants for reactions H + HO_2 = OH + OH (12) and H + HO_2 = H_2 + O_2 (13) have been accepted. However, at higher temperatures the data are scarce. Mueller et al. [109] performed flow reactor studies and determined the rate constants of the above reactions for a range of temperatures and pressures. They inferred with a compilation of data depicting the kinetic response of the $H_2/O_2/N_2$ mixture to the changes in pressure (up to 100 atm) and stoichiometry with new explosion limit data. As per their conclusions, the reaction HO_2 + H = H_2 + O_2 shows high sensitivity towards lean conditions and is more important than the other competing reactions. The rate constants recommended by Mueller et al. [109] have been included in the present mechanism. The third possible route, HO_2 + H = H_2O + O has not been included in many previous studies due to its large uncertainty in the rate constant due to the slow nature of the reaction. The recommendation of Baulch et al. [93] is included in the present study.

The peculiarities of the rate constant of reaction 22, CO + O (+M) = CO_2 (+M) were analyzed in a number of studies [116, 125, 102, 126]. Allen et al. [115] proposed to combine the low-pressure rate constant expression from Westmoreland et al. [126] fit to a modified Arrhenius form and Troe's [116] high-pressure rate constant using a Lindemann fit [125]. Warnatz et al. [127] modified the recommended low-pressure rate constant of Warnatz [102] within 1000 - 3000 K by multiplying it with a factor of 1.34. Davis et al. [86] evaluated the uncertainty factor of this rate as 2, and in the optimization procedure proposed to multiply the rate constant of Allen et al. [115] by a factor of 0.76. In the present work the expression of Allen et al. [115] was adopted with the uncertainty factor of 2.

Temperature and pressure dependence of the rate constant of reaction 23, CO + OH = CO_2 + H was a subject of many experimental and theoretical studies. Experimental studies and reviews prior to 2004 were summarized by Baulch et al. [93]. Rate constants derived by Troe [128] were largely based on the experiments of Fulle et al. [95]. They have been accepted as recommendations by Baulch et al. [93]. The formation of the intermediate species HOCO and hence, pressure and temperature dependence is argued by Troe [128]. Li et al. [82] also acknowledges this fact and determined a rate constant by fitting experimentally measured rate constants available in literature by the method of least squares. The expression of Li et al. [82] has been adopted in this study.

The rate constant of the pressure-dependent reaction CO + OH (+M) = HOCO (+M) (24) was derived based on Troe [116] and proceeds mainly at low tem-

peratures [82]. CO concentration is also influenced by reaction 26, CO + HO_2 = CO_2 + OH. Kim et al. [129] and Tsang and Hampson [113] suggested rate constants that were reported by Sivaramakrishnan et al. [91] to have higher uncertainty. This reaction is important during the chemical induction period as it has significant heat release at that stage. Through experimental studies Mittal et al. [98] suggested the use of a revised lower value than Baulch et al. [93], especially for temperatures around 1000 K. Sun et al. [7] performed calculations based on ab initio theory and canonical transition state theory to determine the reaction rate constant which has been used in the present study.

Decomposition of formyl radical in HCO + M = H + CO + M (27) is the main pathway to generate CO at high temperature. Timonen et al. [130] studied the reaction of HCO with four molecules as a function of temperature in a tubular reactor and determined their rate constants. Study by Li et al. [82] inferred that the rate is two times lower than that of Timonen et al. [130]. Zhao et al. [131] showed that the reaction is most sensitive to certain temperature ranges. Li et al. [82] recommended a weighted least square fitting to all the experimental data available in the literature and yielded a new correlation. Baulch et al. [132] reviewed the rate constants prior to 1992 and recommended a value which is being used in the present study.

Reaction 32, HCO + O_2 = CO + HO_2 has a rate constant based on the reviews and evaluations of Baulch et al. [93]. Reaction between hydroperoxy radical and formyl radical HCO + HO_2 = CO + H_2O_2 (34) has not been studied experimentally. Tsang and Hampson [113] estimated the total rate constant with a high uncertainty of a factor of 5 and this value is included in the present model. The second channel (34) was assumed minor with a rate 10 times smaller.

Self-reaction between HCO radicals includes two channels HCO + HCO = CH_2O + CO (35) and HCO + HCO = CO + CO + H_2 (36). In the majority of kinetic studies reviewed by Baulch et al. [93], these channels were indistinguishable and an overall rate constant within 230 - 1000 K was given with an uncertainty factor of 1.6 at 300 K rising to 2 at 1000 K. Friedrichs et al. [117] assumed reaction (35) as the major channel and demonstrated that at temperatures below 820 K concentration time profiles of HCO are affected by this reaction. Therefore, it should be considered in the kinetic models developed for these intermediate temperatures. In the present study, the temperature-independent rate constant of Friedrichs et al. [117] is used for reaction (35).

Reaction HOCO (+M) = H + CO_2 (+M) (37) derives its rate constant from Larson et al. [118]. This reaction proceeds as an intermediate to reaction (24).

The reaction is temperature dependent over a narrow range of 200 - 360K. The rate constant of reaction HOCO + OH = H_2O + CO_2 (38) has never been measured. Yu et al. [119] performed ab initio dynamic calculations of the thermal rate constant from 250 to 800 K. Due to some uncertainty of the calculations at temperatures around 400 K, the rate constant was approximated in the present work by a simple Arrhenius expression listed in Table 7.1 with an estimated uncertainty factor of 2. The rate constant of reaction HOCO + O_2 = HO_2 + CO_2 (39) was measured only at room temperature [133, 134, 135]. Poggi and Francisco [136] performed ab initio calculations and found a calculated barrier of an adduct formation with eventual dissociation into products of 1.6 kcal/mol. Yu and Muckerman [120] extended these calculations using a direct dynamic method and calculated thermal rate constant from 200 to 1000 K. The value obtained at room temperature was in good agreement with available measurements. In the present work the results of Yu and Muckerman [120] were approximated by the non-Arrhenius expression shown in Table 7.1. The uncertainty factors of this reaction were evaluated as 2 taking into account experimental scattering and the uncertainty of the modeling of Yu and Muckerman [120].

7.4 Model Validation using Literature Results

After validating the proposed kinetic mechanism with new measurements as discussed in the previous chapter, the scheme was further validated using experimental data available in the recent literature. In general, the scheme is observed to be performing well against all the cited experiments.

Laminar burning velocity

Experimental results of lean H_2-CO mixtures at elevated pressures are scarce in literature. In view of the applicability of the proposed model, the validations were carried out with CHEM1D at all conditions. Figure 7.4 shows the variation of the laminar burning velocity of H_2-CO mixtures with respect to equivalence ratio at 5 atm and 298 K. The proposed model agrees well with the experimental data of Kéromnès et al.[77], Sun et al. [7] and Tse et al. [10]. Figure 7.5 depict various H_2-CO flames at 10 atm from Sun et al.[7] and Natarajan et al.[1]. The model predicts well especially in the lean region. Experimental mass burning rates [83, 4, 85] for high pressure H_2 and syngas flames at various oxidizer compositions (varying flame temperature) are compared with the modeling in figure 7.6. The predictions are made at 298 K and up to a pressure of 25 atm using the present model. For varying oxidizer compositions, the present model agrees well with the experimental results.

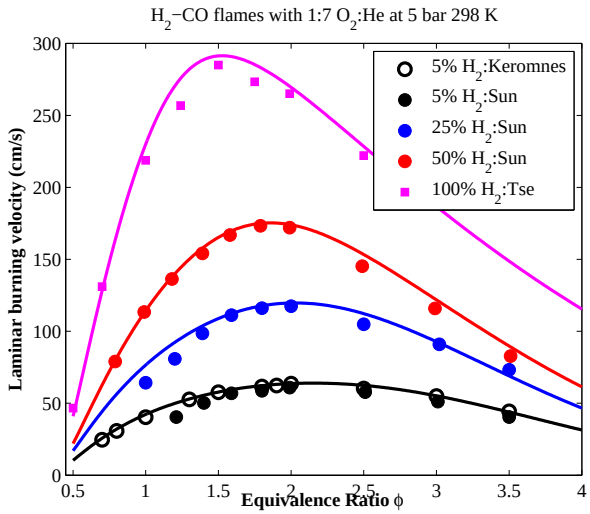

Figure 7.4. H_2-CO flame at 5 atm. Symbols: Experiments [7, 77, 10]. Lines: Present model

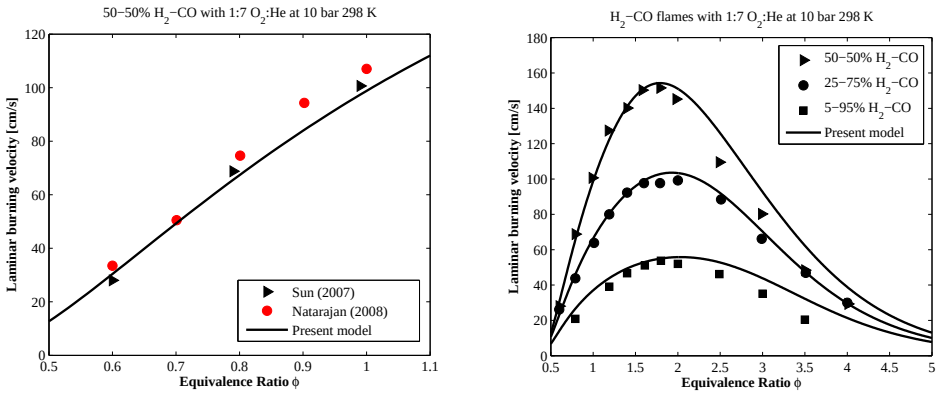

Figure 7.5. 50-50% H_2-CO flame at 10 atm. Symbols: Experiments (left) [7, 1];(Right) [7]. Lines: Present model

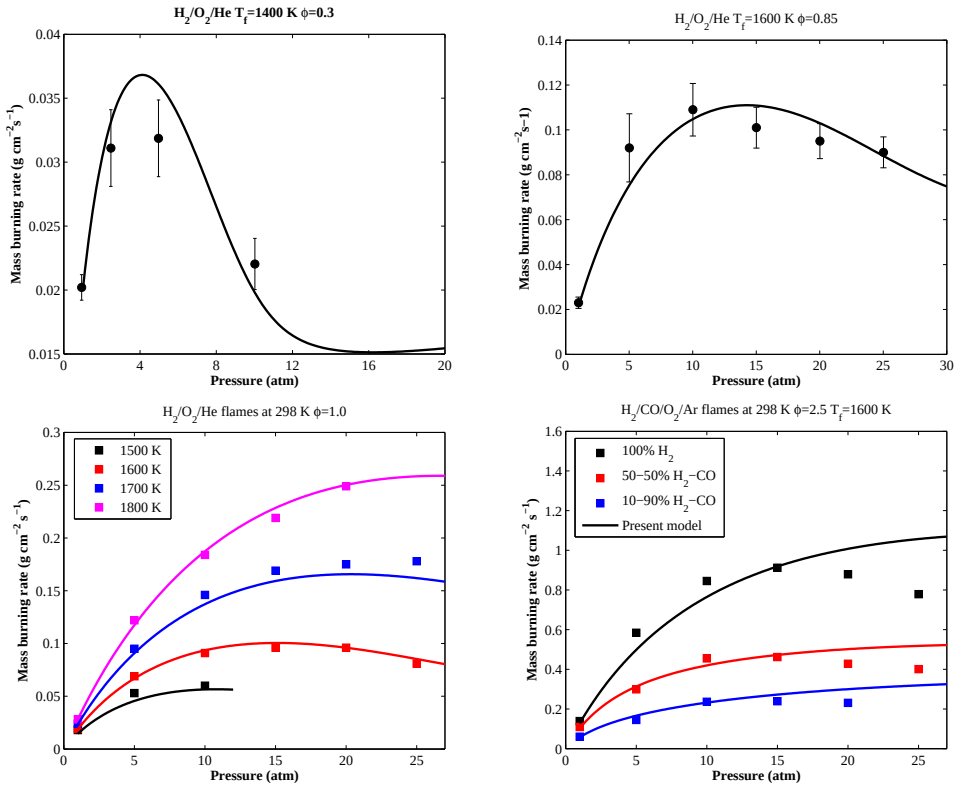

Figure 7.6. $H_2/CO/O_2/He/Ar$ flames; Symbols: Experiments [83, 4, 85]. Lines: Present model

Ignition delay time

Shock tube simulations were performed using a code written by Kazakov [137] as constant pressure adiabatic processes. Figures 7.7 and 7.8 show the variation of ignition delay time with inverse temperature for different $H_2/CO/ O_2/N_2/Ar$ mixtures at 1, 4 and 16 atm obtained by Kéromnès et al. [77]. The ignition delay time defined in the measurements is the time difference between the initiation of the system by the reflected shock wave and the occurance of the OH* maximum. In the modeling, the exact criteria cannot be reproduced as the excited species are not included in the mechanism. Identical delay is defined in the simulations when the pressure gradient reaches the maximum value. Kéromnès et al. [77] also highlight the fact that the OH* peak is very close to the pressure peak for H_2-CO mixtures for CO concentration less than 50 %. With higher amounts of CO, a broad OH* signal is obtained. For this reason, the ignition delay time in figure 7.8 (right) is underpredicted in highly (CO) diluted mixture. In general, the present model agrees well with

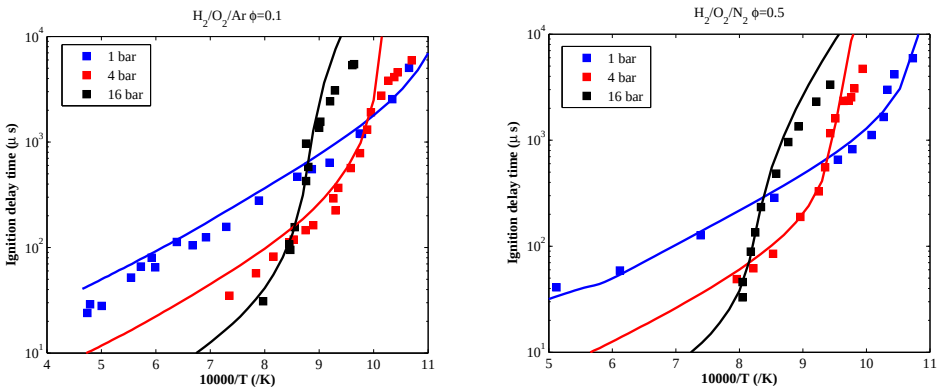

Figure 7.7. $H_2/O_2/Ar/N_2$ mixture, ϕ=0.1 and 0.5 ; Symbols: Experiments [77]. Lines: Present model

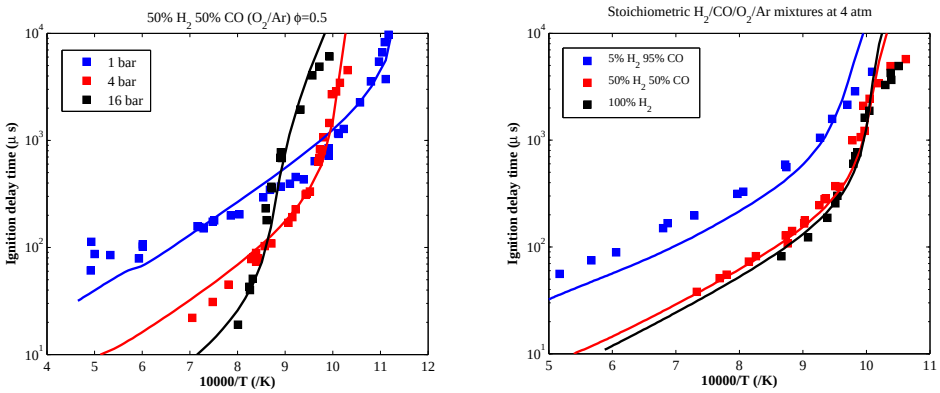

Figure 7.8. (left)50% H_2 50%CO O_2/Ar mixture, ϕ=0.5. (right) Different $H_2/CO/O_2/Ar$ mixtures at ϕ=1.0 and 4 atm; Symbols: Experiments [77]. Lines: Present model

the experimental data. It is also noticed that the ignition delay time does not depend on CO dilution for 50:50 % H_2-CO and lower. This is because of the rapid oxidation of CO.

Species profiles

Flow reactor measurements are simulated using constant pressure adiabatic processes in SENKIN code [138] to validate the species profiles. The time axis was shifted as practiced commonly [88, 97, 109, 83] in order to match the calculated data at a reference point of 50 % consumption of the major reactant. Measurements from Mueller et al. [109] are predicted well by the proposed

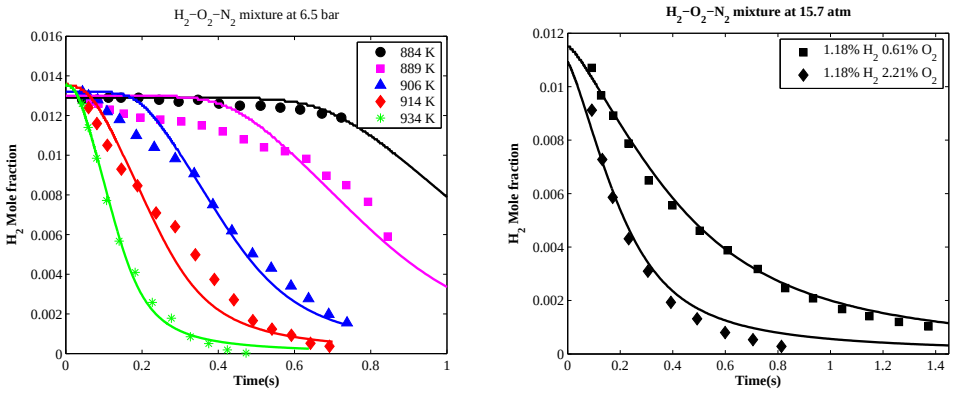

Figure 7.9. $H_2/O_2/N_2$ mixture at 6.5 atm and 15.7 atm. Symbols: Experiments [109]. Lines: Present model

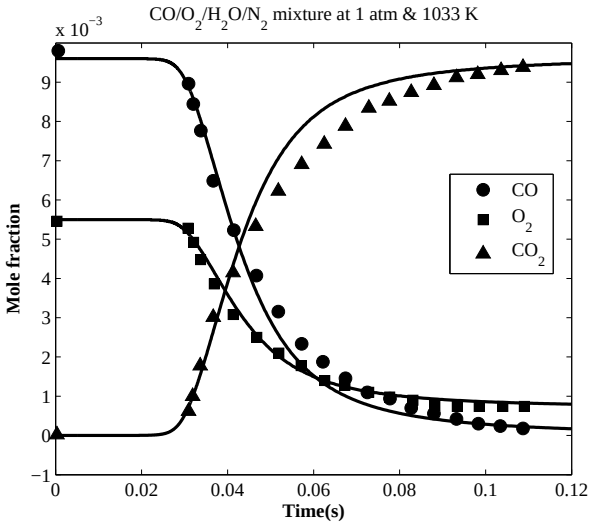

Figure 7.10. $CO_2/O_2/H_2O/N_2$ mixture at 1 atm and 1033 K. Symbols: Experiment [139]. Lines: Present model

model. The comparisons are shown in figure 7.9 for 6.5 atm and 15.7 atm at various temperatures. Figure 7.10 depicts experimental CO, O_2 and CO_2 profiles in flow reactor with $CO(0.96)/O_2(0.55)/H_2O(0.56)/N_2(97.93)$ at 1 atm and 1033 K from Yetter et al. [139]. The proposed kinetic model follows the species profiles closely.

The present validation was also extended to species profiles of burner stabilized flames. The structure of a stoichiometric H_2 (10 %) - O_2 (5 %) - Ar (85 %)

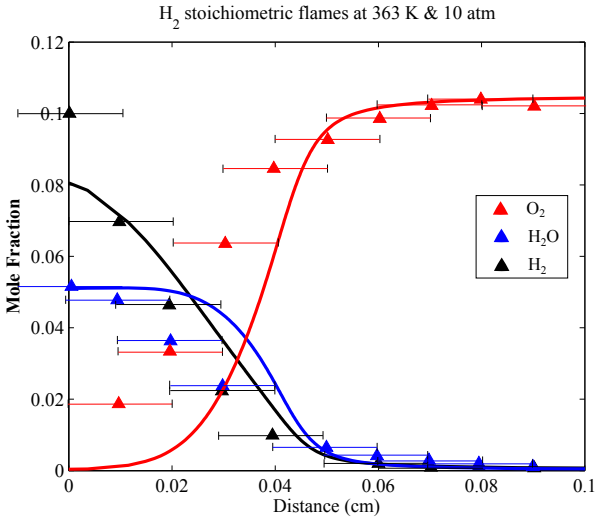

Figure 7.11. $H_2/O_2/Ar$ flame at 10 atm and 363 K. Symbols: Experiment [140]. Lines: Present model (black-H_2; red-O_2; blue-H_2O).

burner stabilized flame was experimentally studied by Paletskii et al. [140] at 1 and 10 atm and initial temperature 363 K using molecular beam inlet mass-spectrometric probing. The study was performed with a spatial resolution of 0.1 mm. At 10 atm, the flame added a further complication of smaller chemical reaction zone (0.7 mm). The agreement between the computed concentration profiles using the present model at 10 atm with the experimental results is satisfactory as shown in figure 7.11. A possible reason for this deviation can be that the concentrations measured using the probe that have limited spatial resolution (0.1 mm) are spatially averaged values. This uncertainty is shown by the spatial error bars in the plot. Also, from a previous assessment [141], it was established that the effect of probe intrusion on burner stabilized flames generate uncertainties up to $\pm$200 K for measured temperature profiles which might lead to deviations as shown in figure 7.11 especially for H_2 and O_2 species profiles.

Summary

An updated H_2-CO kinetic scheme is proposed that includes recently evaluated rate constants from literature. Model validation is performed using results from present experiments (in the previous chapter) and from the literature at atmospheric and elevated pressures. At conditions of high pressure and lean combustion, reactions H + O_2 = OH + O and H + O_2 (+M) = H_2 (+M)

compete the most when compared to others. Reaction H + HO_2 = OH + OH contribute to OH production, however, less at high pressure conditions. At higher CO concentrations and leaner mixtures important role of reaction CO + OH = CO_2 + H is observed in subsequent oxidation of CO. It is demonstrated that the proposed model agrees well with the experimental results obtained in the present study and results from literature for lean as well as rich mixtures at elevated pressures. The model performs better than the ones available in the literature at higher pressures.

CHAPTER 8

Thermographic Phosphor Technique in HFM

The heat flux method distinguishes itself from other methods, like the closed vessel or counter flow methods, because of its relatively simple working principle and the small amount of post-processing. The method is based on the creation of an adiabatic flame by using a specially designed burner. Whether this adiabatic state is achieved or not, is indicated by the temperature profile over the burner plate. The accurate measurement of this temperature distribution is a key factor in the method and this is currently done with the use of eight thermocouples which are spread over the plate. Although the accuracy of the heat flux method is very good compared with other methods [8, 10, 1], there is some room for improvement with respect to the burner plate temperature measurement. This leads to the goal of this chapter: the improvement of the accuracy of the heat flux method by the application of a thermographic phosphor technique.

Thermographic phosphor (TP) measurements are based on the temperature dependent emission of a phosphorescent material. This material is coated on the surface of interest and is then excited with use of light from, for example, a laser system. The method is non-intrusive and it enables the measurement

of the temperature on the entire surface. The temperature measurement of the burner plate is therefore assumed to be more accurate with use of the TP technique than with thermocouples. Whether that is the case or not is investigated in this chapter. Therefore, the technique is implemented in the heat flux method and measurements with methane - air flames are performed.

8.1 Thermographic Phosphor Technique

Given the potential problems with the thermocouples it is assumed that the heat flux method could be improved by replacing them by a different temperature measurement technique. In this thesis, we chose to use a thermographic phosphor (TP) technique. This is an optical method, based on the temperature-dependent emission spectra of phosphorescent materials. Li et al. [142] first introduced the idea of implementing this technique in the heat flux method and our project is focused on the extension of it. Phosphorescence is a type of luminescence: the emission of light by a material. In order to understand this phenomenon, a brief overview of the physical properties of luminescence is given. It deals with the possible energy levels in molecules and the effect of absorption of energy. The theory helps to understand the working principle of the specific measurement method adopted here, the so called spectral ratio method.

Physical properties of luminescence

In order to understand the method which is used for measuring the temperature of the burner plate, a brief discussion of the physics behind phosphorescence is given. Khalid and Kontis [143] give a clear overview of the phenomena that occur during the excitation of molecules and the emission of photons which might follow afterwards. This work is focused on luminescence in molecules. In the case of thermophosphors which are used in temperature measurements, however, phenomena are somewhat different and more complex. Although the theory explained here is not complete, it helps to understand the global physics behind luminescence.

The theory behind luminescence is based on the quantum mechanical description of the internal energy of a molecule. According to this description, a molecule can only have certain discrete energy levels. These are for a large part defined by the electronic state the molecule is in. The electronic states, however, are further split into a number of vibrational and rotational states, characterized by the quantum numbers n, v and J respectively. The total

internal energy, $\mathrm{E(n,\upsilon,J)}$, depends on the combination of these quantum numbers and the possibilities can be drawn in a Jablonski energy level diagram, as shown in figure 8.1. The energy difference between two electronic states is larger than those between two successive vibrational states, while the difference between two rotational levels is even smaller. The rotational levels are not shown in figure 8.1, because they are too close to each other. Besides that, most of the thermophosphors are combinations of single atoms in a host lattice, for which the rotational energy is of no relevance. The state of a molecule can further be defined by its spin (singlet state S or triplet state T), which is also shown in the Jablonski diagram.

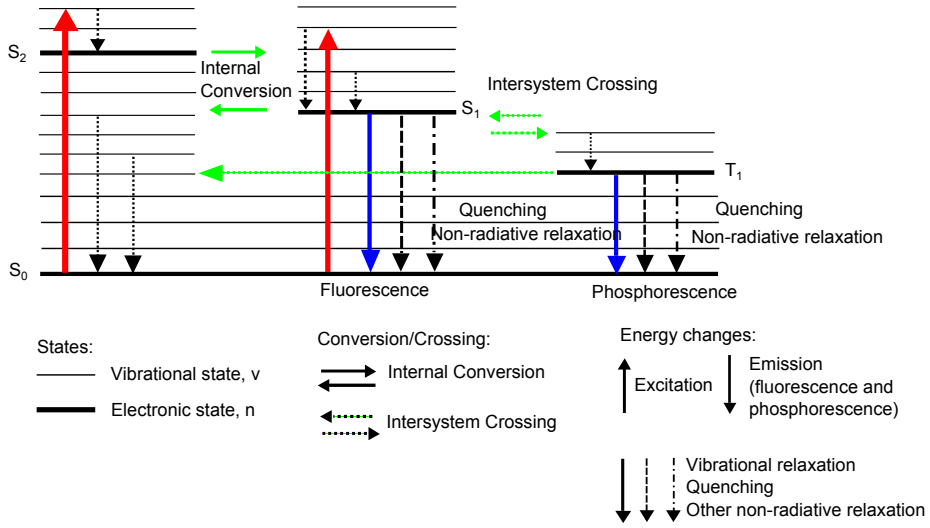

Figure 8.1. Different electronic and vibrational states a specific molecule can be in. Possible luminescence processes are indicated by arrows with a solid shaft. [143]

Molecules usually are in the electronic ground state. But even in the ground electronic state, different vibrational states can be occupied and the distribution over these states depends on the temperature. At higher temperatures, the internal energy of molecules is larger and more of the higher energy levels are populated. The distribution over these states can be estimated with the Boltzmann distribution, using the same three quantum numbers n,υ and J:

$$\mathrm{N(n,\upsilon,J)} = \frac{\mathrm{g_{n\upsilon J}\exp\{-E(n,\upsilon,J)/k_B T\}}}{\mathrm{Z(T)}}\mathrm{N_0}\,, \tag{8.1}$$

with

$$\mathrm{Z(T)} = \sum \mathrm{g_{n\upsilon J}\exp\{-E(n,\upsilon,J)/k_B T\}} \tag{8.2}$$

In these equations, $\mathrm{N(n,}\upsilon\mathrm{,J)}$ [-] is the amount of molecules in a specific state, $\mathrm{N_0}$ [-] the total amount of molecules, $\mathrm{g_{n\upsilon J}}$ [-] the degeneracy factor of each energy level, $\mathrm{E(n,}\upsilon\mathrm{,J)}$ [J] the specific internal energy of a given state, $\mathrm{k_B}$ [J $\mathrm{K^{-1}}$] the Boltzmann constant, T [K] the temperature, and $\mathrm{Z(T)}$ the partition function. Equation 8.1 shows that the amount of molecules in a specific state, $\mathrm{N(n,}\upsilon\mathrm{,J)}$, mainly depends on the temperature and the internal energy of that state.

Although the Boltzmann distribution describes the general energy distribution of molecules in equilibrium, it is possible to excite molecules from the ground electronic state (S_0) into higher states (S_1, S_2). This is caused by external influences, for example due to the absorption of energy in the form of photons. All of the excited molecules, however, will eventually relax back into the ground state again. This can happen through various processes, for example by emission of photons equal to the energy-level difference between two states, energy transfer via quantized vibrational exchange (phonons) in a lattice or by other complex energy transfer mechanisms.

The possible transitions that are shown in figure 8.1, are:

- *Vibrational Relaxation:* Molecules which are excited into higher vibrational states within an excited electronic state (for example $\mathrm{S_1}\,^{\upsilon 2}$) loose energy as heat after relaxation into the lowest vibrational energy level ($\mathrm{S_1}\,^{\upsilon 0}$). For embedded atoms, this can be seen as vibrations occurring in the crystal lattice.

- *Internal Conversion:* If the lowest vibrational level of an excited state is sufficiently close to a higher vibrational level of a lower electronic state, vibrational relaxation can occur between these two levels (for example $\mathrm{S_2}\,^{\upsilon 0}$ to $\mathrm{S_1}\,^{\upsilon 5}$). Again, energy is lost as heat.

- *Fluorescence:* During fluorescence, a radiative transition from a higher electronic state into a lower one is made by emitting a photon. The energy of the photon equals the energy difference between the two states.

- *Quenching:* Energy is transferred to a nearby molecule during a transition from a higher state into a lower state. No photon is emitted during this process.

- *Intersystem crossing:* During inter-system crossing, a transition from $\mathrm{S_1}$ to $\mathrm{T_1}$ (or vice versa) takes place. This requires a change in electron spin and it has generally a low probability of occurrence. Impurities in the crystal structure, however, can increase this probability. Since the

molecule has not yet returned into the ground state, the following possibilities might subsequently occur:

- *Phosphorescence:* This is a radiative transition from T_1 to S_0, and the emitted photon has the same energy as the energy difference between the two states. This process is a so called forbidden transition and the chance of occurrence is low. Therefore, the process is typically slower than fluorescence.
- Quenching (also from T_1 to S_0) and other non-radiative transitions.
- *Delayed fluorescence:* Inter-system transition back to S_1, where the entire process of relaxation starts again.

Concluding from the descriptions above, the internal energy of molecules takes on discrete values and can be characterized with the three quantum numbers n, υ and J. At a given temperature, the Boltzmann distribution can be used to make an estimation of the population in each state. The absorption of photons, however, can increase the internal energy of the molecule for a short period of time. Absorption can only take place if the energy of a photon equals the energy difference ΔE between two allowed energy levels of a molecule in order to fulfill the energy conservation principle. The difference in energy, ΔE, is defined as [144]:

$$\Delta\mathrm{E} = \mathrm{E}(\mathrm{n}', \upsilon', \mathrm{J}') - \mathrm{E}(\mathrm{n}'', \upsilon'', \mathrm{J}''), \tag{8.3}$$

in which quantum numbers denoted with ' stand for the higher energy state (after absorption of a photon) and quantum numbers denoted with " for the lower energy state (before absorption of a photon).

The energy of a photon is given by:

$$\mathrm{E}_{\mathrm{photon}} = \mathrm{h}\nu = \frac{\mathrm{hc}}{\lambda}, \tag{8.4}$$

in which h [Js] represents Planck's constant, ν [s^{-1}] the frequency, c [m/s] the speed of light, and λ [m] the wavelength. Absorption on a particular transition can take place if $\Delta\mathrm{E}$ (for example between two vibrational states in two different electronic states) equals $\mathrm{E}_{\mathrm{photon}}$. This is, however, not the only requirement. A lot of selection rules have to be met for a transition to be allowed. This decreases the amount of possible photon energies that can be absorbed by a specific material, which makes the absorption spectrum a characteristic material property.

After absorption of a photon, the molecule is in an excited state and can relax back into the ground state by one or more of the earlier mentioned processes. Not all of these processes, however, have the same timescale. Vibrational relaxation for example occurs very quickly after the absorption of a photon (order of picoseconds (10^{-12} s)), such that most of the excited molecules will fall back into the ground vibrational state of the excited electronic state before any radiative emission occurs. Radiative emission is much slower (typically around 10^{-8} s) and therefore usually starts from the ground vibrational level of the excited state. This effect explains the red-shift of the emitted photons compared to the absorbed photons. The emitted photons have a lower energy than the absorbed ones, and therefore, according to equation 8.4, a larger wavelength.

The process of absorption and emission of photons is the basis of the thermophosphor technique. In our specific measurement a material is used in which phosphorescence occurs due to impurities in a crystal lattice and of which the emission shifts with temperature. The working principle of this so called spectral ratio method is explained in the next section.

Spectral ratio method

As mentioned before, molecules can absorb and release photons. Absorbed photons must have the same energy as the difference between two possible energy states of the molecule and therefore only specific transitions can be made. After the excitation, the molecule emits a new photon and returns into the ground electronic state. This emission is usually red-shifted and characteristic for a type of molecule. Besides that, the emission spectrum can be temperature dependent, partly because of a difference in population of energy levels at different temperatures [145]. This effect is described with the Boltzmann distribution of equation 8.1. The exact theory behind the shift in wavelength, however, is still under discussion.

The temperature dependence of the phosphorescence emission spectrum is the key factor of the thermophosphor method used for this thesis, the so called spectral ratio method. Usually the spectrum shifts into a specific direction, which is illustrated in figure 8.2. This figure shows two emission spectra of a ZnO:Zn phosphor powder, which is excited by a 355 nm laser. The horizontal axis represents the wavelength, while the vertical axis represents the intensity of the specific emission. The peak at 355 nm, as well as the second harmonic of the laser light at 532 nm, are reflections of the laser and do not originate from the emission of the phosphor powder. The band near 390 nm and the very broad one centered around 510 nm, however, are characteristic for ZnO:Zn.

Besides that, one can see the red shift of the center wavelength of the 390 nm wavelength band with increasing temperature.

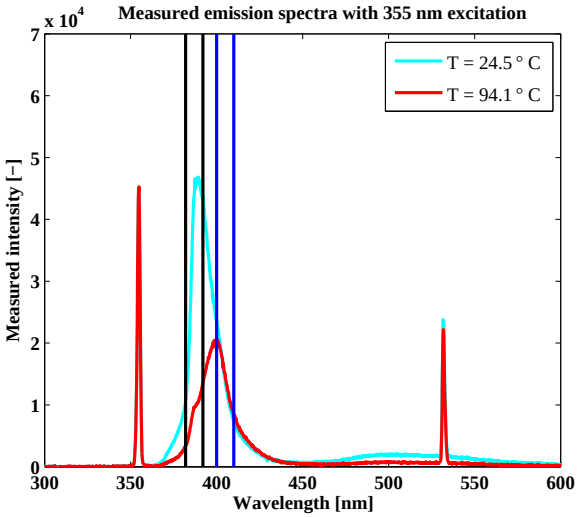

Figure 8.2. The emission spectrum of ZnO:Zn which is excited with a 355 nm laser. Two curves are drawn for two different temperatures and the shift in emission wavelength is clearly visible. The blue and black lines indicate the limits of two different band pass filters [146].

Besides the emissions of the phosphor, four lines are drawn in figure 8.2. They represent the limits of two band pass filters which are centered around 385 nm and 405 nm. These filters transmit light with wavelengths within the narrow band, while they block light with wavelengths lower or higher than the limits. Figure 8.2 is used to explain the working principle of the spectral ratio method.

In the spectral ratio method, two separate measurements of the phosphorescence intensity at a specific temperature are involved, each of them using a different spectral filter. During such a measurement, only a specific narrow wavelength band of the emission is transmitted by the filter. The intensities in the individual measurements are thus, due to the use of two different filters, not equal and the relative signal strength depends on the details of the spectrum. As the emission spectrum changes with temperature, another set of measurements at a different temperature would result in a different value for the ratio between both intensities. The ratio and temperature can thus be related to each other and the resulting calibration curve can be used for measurements at unknown temperatures. To illustrate this effect, the simulated ratios that

belong to the spectra and filters drawn in figure 8.2 are shown in table 8.1.

Table 8.1. Effect of filtering two different emission spectra of ZnO:Zn at different temperatures (from figure 8.2). The ratio between the filtered images is temperature dependent.

T [°C]	Intensity after filter of 385 nm [-]	Intensity after filter of 405 nm [-]	Ratio $\frac{I_{405nm}}{I_{385nm}}$[-]
24.5	$3.57 \cdot 10^5$	$1.33 \cdot 10^5$	0.37
94.1	$8.67 \cdot 10^4$	$1.39 \cdot 10^5$	1.59

Pros and cons of the thermophosphor technique

In the sections above, the spectral ratio method was explained and some important advantages over other temperature measurement techniques can be found from its characteristics. There are few problems with the thermocouples that are presently used in the heat flux burner. They disturb the flow and only provide point measurements. The thermophosphor measurement, in contrast, allows to measure a surface in two dimensions without disturbing the flow, as the method is non-intrusive. A thermophosphor is coated onto the surface of interest and measurements are performed with a camera, not making any contact with the surface. There are other temperature measurements that could be used, but most of them are affected by the environment during a combustion process. Infrared Spectroscopy (IR) for example is a high-quality optical temperature measurement method, but the presence of the flame on top of the burner plate would disturb the measurement.

Besides the advantages of the method, there are also some disadvantages which have to be taken into account. First of all, many phosphors show little shift in the emission spectrum with changing temperature. The sensitivity is therefore not very high and the choice for a specific phosphor is mainly based on the sensitivity to the temperature in the range of interest.

The values of the calculated ratios are not only dependent on the material, but also on the process conditions. Different filters, larger grain sizes of the phosphor powder or differences in laser power might result in different ratios for one specific temperature. This means that the calibration curve has to be made for a specific set of process conditions and has to be renewed if for example a

new phosphor layer is applied.

The fact that two identical images have to be made which are filtered separately makes the measurement setup somewhat complicated. The images preferably must be taken simultaneously, to make sure that the conditions do not change. This means that two cameras are required, or otherwise a stereoscope has to be used. This is a device that can split an image into two identical images before it reaches the camera.

At last, the temperature measurement is performed on the phosphor powder itself and not on the surface underneath. The assumption is made that the temperature of the surface equals that of the phosphor layer, but in case of a thick layer or quickly changing temperatures, this assumption may not be valid anymore.

A possibly more sensitive type of the thermographic phosphor technique is the luminescence lifetime method, which is often used for point measurements. Many phosphors are available to be used in combination with this method and the sensitivity is very high. Fuhrmann et al. [147] compared both types of thermographic phosphor techniques in combination with the phosphor Mg_4FGeO_6 and concluded that the lifetime method was more accurate. It was investigated whether this technique could be used for the heat flux measurements, but some problems were seen. In order to do a two dimensional measurement, a high-speed camera is needed. The phosphor which is chosen in our measurements (see next section) can be used in combination with both methods, but the lifetime of its phosphorescence is very short. A camera whose speed is high enough to perform proper measurements with was not available, but it remains an option to be further investigated in the future.

Choice of a proper phosphor

Before being able to use the spectral ratio method for temperature measurements as explained in the previous section, a proper phosphor has to be chosen. Phosphors are usually ceramic powders doped with some kind of rare-earth metal [142]. Many different types are available, each with its own specific properties. This section describes which phosphor is chosen for our measurements and also highlights its characteristics.

The choice for a specific phosphor is based on its optical properties. Because it was decided to use the spectral ratio method, the emission peak of the chosen phosphor must shift with temperature. Besides that, this temperature dependency must be present in the region of interest, known to be within 80 and

120°C. Aldén et al. [148] reviewed many possible phosphors, resulting in the plot in figure 8.3. This graph includes phosphors which can be used in combination with the spectral ratio method, as well as phosphors which are suitable for lifetime measurements. Their sensitivity to temperature changes is related to the slope of the graph: the sensitivity is large if the absolute slope of the graph is large.

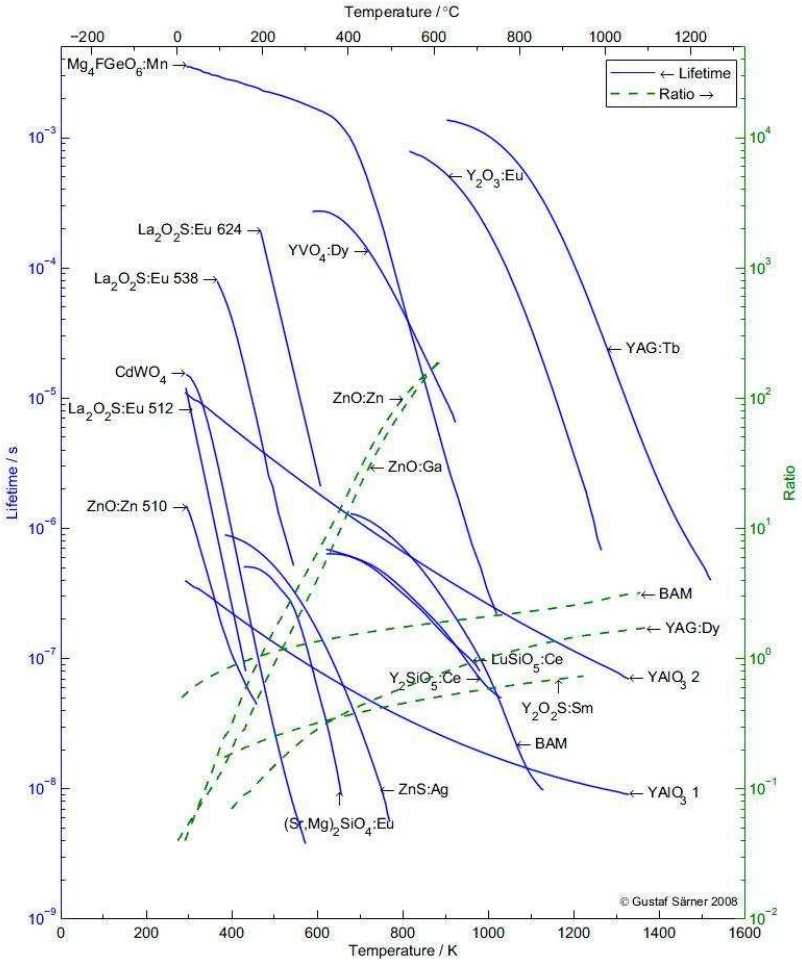

Figure 8.3. Overview of phosphorescent properties of several materials. Some of them are suitable for decay-time measurements, while others can be used in combination with the spectral ratio method. The slope of the curves indicate their sensitivity to temperature changes, and is therefore an important parameter in choosing a phosphor [148].

One can see in figure 8.3 that ZnO:Zn and ZnO:Ga are most sensitive in the

temperature range of interest in combination with the spectral ratio method. Both of them are further investigated by Särner [149]. ZnO:Zn is a little more sensitive to changes at lower temperatures and is therefore chosen for our measurements on the heat-flux burner. The ZnO:Zn powder used was ordered from Phosphor Technologies Ltd (UK) [150], in powder form with an average grain size of 3.5 μm. Its properties are described in more detail in the next section.

Properties of ZnO:Zn

ZnO:Zn is a zinc oxide crystal with oxygen deficiencies. The oxygen vacancies are replaced by zinc atoms, filling up the crystal structure. This material is often used in several devices, like in LED's, displays, thin-film solar cells and as nano-structure gas sensors [148]. The material can be excited in several ways, for example with the use of a 355 nm laser or with electrons using cathodoluminescence [151]. This excitation will lead to photon emission and the spectrum shows two peaks: a short living peak in the UV range (near 390 nm) and a broad peak near 510 nm. The latter is often used in displays, where its green color is used for producing images. In the present experiments, however, the UV peak is the most interesting. It is a very short living emission (a few nanoseconds) and the center wavelength shifts with temperature.

The specific structure and composition of the zinc oxide determines the optical properties of the material. The visible green emission originates from native defects in ZnO and oxygen deficiencies. An increase in oxygen concentration towards stoichiometry therefore leads to a decrease in visible emission intensity [151, 152]. The peak can even disappear completely using specific process conditions in which there is little chance of defect formation in the crystal [153]. The characteristics of the UV emission also depend on the crystal structure of the zinc oxide. This emission is caused by several impurities and structural effects in the lattice, for example due to radiative transitions from a defect band to the valence band [154]. Therefore, each sample of ZnO can, due to differences in process conditions during the manufacturing, differ in its actual structure and therefore emit light with different wavelengths. Also grain sizes play an important role in the central position of the UV emission peak. Due to all of these effects, the wavelength of the maximum intensity of the UV emission at room temperature can vary between for example 362 nm in nanoclusters [153] towards 390 nm in commercially available powders [149].

During annealing, the structure of zinc oxide can be altered. Atoms gain energy during this process to rearrange in the lattice, which decreases the amount of impurities. This leads to a narrower and more intense emission band in the UV

range [152]. On the other hand, if the annealing process takes too long, new defects can occur which behave as non-radiative recombination centers and decrease the emission. Therefore, an optimum annealing time and temperature exist. The visible green emission can also be altered during the annealing process. Depending on the environment, oxygen can be captured or released from the structure and the intensity of the green emission changes as a result of the oxygen concentration in the zinc oxide [154].

From these characteristics of zinc oxide, one can imagine that the process conditions during the manufacturing of the material are of great importance for the resulting optical properties of the phosphor. The formation of zinc oxide crystals is quite complex and depends on many variables. This means that a suitable composition has to be chosen for a specific application. A large amount of green emission is required if zinc oxide is used in displays, while a large amount of UV emission is preferred in temperature measurements using the spectral ratio method. The optimal composition in both cases will differ and it is important to choose the correct one. Samples might differ from batch to batch and in our specific case of the temperature measurements, this means that a calibration curve has to be composed each time a new sample or coating is used.

The temperature dependent shift of the UV emission peak is used to measure the surface temperature of the burner plate. This spectral ratio method has many advantages over other techniques, but also has some disadvantages. For doing two dimensional measurements, it might be the most straightforward and easy to perform method, but the sensitivity is somewhat lower than for most lifetime methods. ZnO:Zn, however, shows quite a strong spectral temperature dependency, comparable to some phosphors used for the lifetime method. Although the long living green emission might spoil the measurement, it usually has quite a low intensity that can be coped with by using short camera gating times. But this emission peak can also make life easier. Although its maximum does not shift with temperature, its lifetime does [148]. This means that the visible emission can be used for decay-time measurements, and once a coating is made, both options can still be chosen. For sure this is only possible if the crystal structure is in such a condition that both peaks appear with sufficient high intensity.

8.2 Optical Setup

The optics in the setup are of great importance for the results of the measurements. The beam is broadened with a concave lens to illuminate the entire

burner plate surface. Besides that, an optical setup is built to regulate the laser power. During experiments, it was noticed that the timing of the arrival of the laser pulse is unstable if the laser is not operated at its optimal settings, at which the laser power is at its maximum. It is therefore not possible to regulate the laser power with the control of the laser itself, and therefore the setup of figure 8.4 was designed.

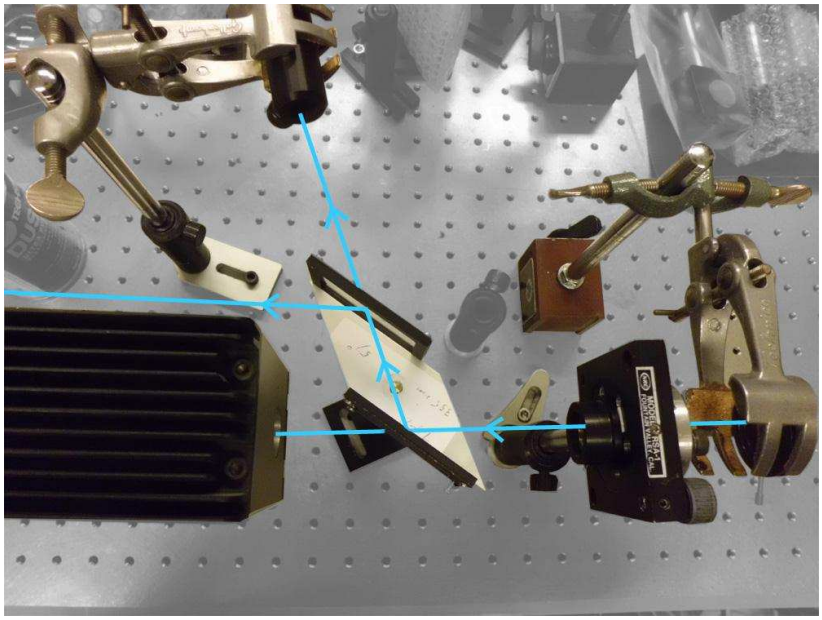

Figure 8.4. Optical setup to regulate the laser intensity. The beam comes in from the right, passes a diaphragm, half-lambda plate and two polarization-dependent mirrors. A part of the beam is reflected, the other parts are caught by the two beam dumps.

The laser beam (355 nm), which comes in from the right, is directed through a diaphragm and a half-lambda plate. By rotating the optical axis of the plate, the polarization of the light is rotated too. This can be adjusted continuously. The beam with the new polarization is then reflected by two parallel mirrors, of which the reflection depends on the polarization of the light. Part of it will be transmitted, and this light is caught by beam dumps. The remaining part of the beam is reflected by the mirror and continues its way to the burner head. The amount of reflected light depends on the polarization of the beam after it passed through the half-lambda plate and can therefore be chosen to be between almost 100% and hardly anything.

Another problem which was encountered during measurements, was the fact that the homogeneity of the profile of the beam is very poor, even if the laser runs at maximum power. Because we had no access to high quality optics to homogenize the profile, a simple but surprisingly well-working solution was found. A piece of scotch-tape was placed in the beam, which made it more diffused. The diffused beam was then sent through a concave lens to broaden it and finally reflected towards the burner head with a mirror.

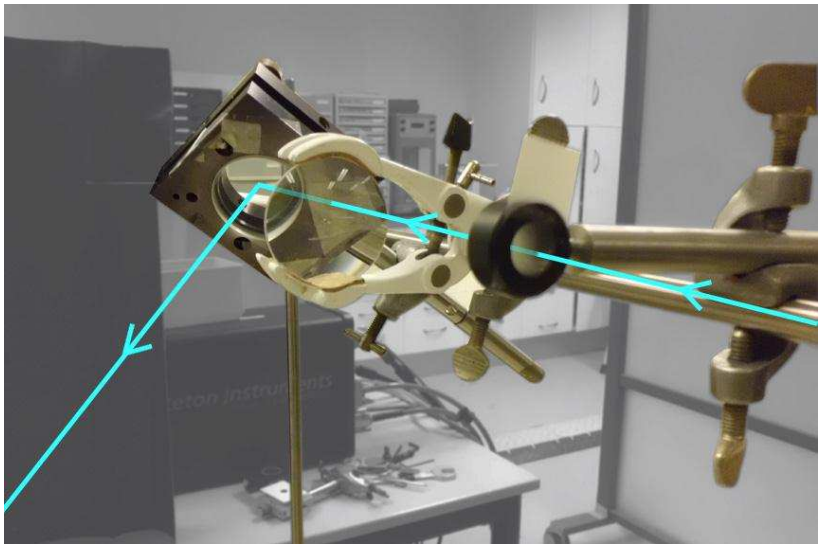

Figure 8.5. Optical setup to homogenize the laser beam. The beam travels through a piece of scotch-tape, is then broadened and finally reflected towards the burner head.

Stereoscope

A stereoscope is a device which can split an image in two identical images. A commercially available version is shown in figure 8.6. The main parts of this stereoscope are the two mirrors under an angle of 45 degrees and a prism. Rays from an object in front of the stereoscope will fall symmetrically on both sides of the stereoscope and pass through one of the openings. Due to the reflection on the mirrors and the prism, the separated rays form two identical images on the objective of the camera. If two different filters are placed in front of the openings, the resulting images can be used in combination with the spectral ratio method.

The type of stereoscope that is shown in figure 8.6 is commercially available and can be ordered from several suppliers. They are, however, quite expensive

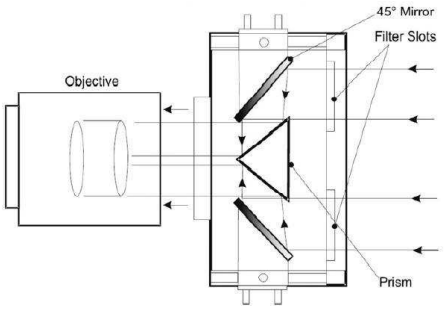

Figure 8.6. The working principle of a commercially available stereoscope [148].

and therefore, it was decided to design one in-house. Since, it seemed quite complex from a mechanical point of view to build one like shown before, a different design is chosen. Instead of using mirrors to reflect rays of light, a prism is chosen to refract them.

Chosen filters

The spectral ratio method is based on comparing two identical images which are filtered on different wavelengths. There is a large range of possible filters that can be used, each of them with their own advantages and disadvantages. This section deals with the decisions which are made while choosing the two filters for the temperature measurements.

Filters are used to transmit or block emitted light with specific wavelengths. There are many filters available, with different wavelength dependent properties. Two common filters are band pass filters and edge filters. A band pass filter transmits light within a specific, rather small, range of wavelengths. Light with wavelengths outside this band will be blocked. An edge filter transmits light with wavelengths larger than a limit value. A schematic representation of both filter types is shown in figure 8.7. In these graphs, the transmittance of the filter (vertical axis) is plotted against the wavelength (horizontal axis).

The filters that are used for the temperature measurements on the heat flux burner have to transmit at least part of the phosphorescence emission. This limits the amount of possible filters. Furthermore, the reflected laser light of 355 nm has to be blocked. Preferably, also the second harmonic reflection of the laser at 532 nm should be filtered out, just like the emission of radicals in the methane-air flame. The intensities of these two emissions, however, are relatively low and can also be suppressed with short exposure times of the camera.

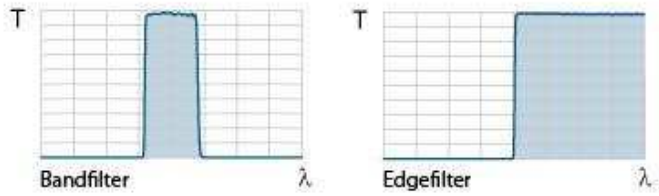

Figure 8.7. Schematic representation of a band pass filter and an edge filter. The transmittance is plotted versus the wavelength.

The emission of the ZnO:Zn phosphor (after excitation with laser light of 355 nm) has a peak near 390 nm, which shifts a little with increasing temperature. This temperature dependency can be seen in figure 8.8. The figure also shows the emission peak near 510 nm. The spectrum of ZnO:Zn reduces the possible filters to a range between approximately 380 nm and 420 nm. From the suppliers Edmund Optics and Semrock, a set of filters is chosen which are used for further investigations. These filters are shown in table 8.2.

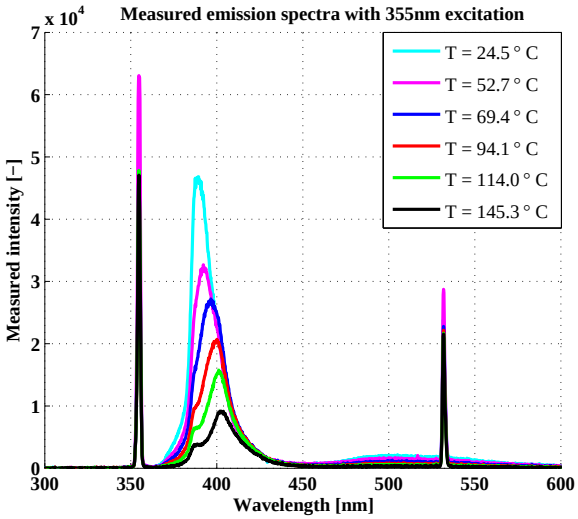

Figure 8.8. Measured emission spectra of ZnO:Zn after excitation with laser light of 355 nm. [146]

The spectra shown in figure 8.8 and the properties of the filters in table 8.2 are used to choose the best combination of filters. To do so, a Matlab script is written in which a summation is performed over all transmitted wavelengths, multiplied with the corresponding emission intensity. This is done for each

Table 8.2. Possible filters with their properties.

Type of filter	Center wavelength [nm]	Edge [nm]	Brand
Band pass filter	387 ± 5.5		Semrock
Band pass filter	390 ± 5		Edmund
Band pass filter	405 ± 5		Semrock
Band pass filter	410 ± 5		Edmund
Band pass filter	415 ± 5		Edmund
Band pass filter	420 ± 5		Edmund
Broadband filter	435 ± 20		Edmund
Edge filter		400	Edmund
Edge filter		420	Edmund

filter and for each emission spectrum. The ratio between these values is calculated for possible filter combinations and plotted as function of temperature. It was noticed that the results of these simulations will differ from the final measurements, because the time-dependency of the emission intensity and the influence of the laser power is not taken into account. Nevertheless, this simulation provides some basic knowledge of the relative sensitivity of these sets of filters. A high sensitivity to temperature is related to a large slope in the ratio versus temperature plot and this is used as a criterion to choose the best set of filters. The absolute value of the slope should be as high as possible in the region of interest: between 80 and 120°C. The overall best set at higher temperatures is the combination of a 387 nm band pass filter with a 400 nm edge filter. Besides that, the temperature dependence of the ratio is quite linear for this set of filters, which gives a constant sensitivity over the entire range. The combination of the 390 nm and 420 nm band pass filters has a higher temperature dependency in the lower temperature range, but the slope is not linear and it decreases at higher temperatures. The use of two band pass filters would be preferred, because they filter out the 510 nm long living emission peak of ZnO:Zn, as well as the second harmonic laser reflection and some of the emissions of the flame. These effects, however, can also be dealt with by using short exposure times of the camera. Therefore it is suggested to use the 400 nm edge filter anyway. Unfortunately due to some problems during ordering the filters, a band pass filter of 387 nm (± 5.5 nm) and an edge filter of 420 nm was received.

8.3 Results

Heat flux measurements are performed with use of the standard method, as well as with the new thermophosphor method. The burner plate for the thermophosphor measurements is an old type with a thickness of 2 mm, holes of 0.5 mm in diameter and a pitch of 0.7 mm, which was airbrush coated with the ZnO:Zn powder. The use of an old type of plate instead of one with smaller holes makes it easier to align the recorded images during post-processing. Four thermocouples were attached to the plate, spread over different angles and radii. Measurements were performed with the use of a Nd:YAG laser with frequency tripling (355 nm), with an average power of 1.4 W. A study on the influence of the gate delay between the Q-switch of the laser and the start of the record of images demonstrated that there is a relatively large range of delays that result in similar measured intensity ratio values. A setting within this range was chosen for our measurements. Furthermore, the stereoscope with the band pass (387 $\pm$ 5.5 nm) and edge (420 nm) filters was mounted in front of the camera. In order to suppress the background intensity, a short gate width of 5 ns was chosen, in combination with a gain of 100 [-]. 25 Accumulations were used to average out the noise from the camera and several background images were made. In order to make a second flat field for possible wavelength dependencies in the pixels of the CCD-chip, an image was made at a constant plate temperature of 21°C.

The thermocouple values were first used to make a calibration curve between temperature and calculated ratio values. This curve is shown in figure 8.9 (left). A linear fit is made through the data and this line, together with the standard deviation between fit and data, is drawn in the graph as well. This fit is defined by:

$$\mathrm{T(ratio)} = 44.109 \cdot \mathrm{ratio} + 50.908 \ (\pm 0.8) \ [^{\circ}\mathrm{C}] \tag{8.5}$$

Since, the relation between ratio and temperature is linear, the translation of the ratio profile over the burner plate into a temperature profile is not needed to calculate the laminar burning velocity. It is nevertheless useful to make the translation to compare the results with those of the standard heat flux measurements.

A typical temperature distribution over the burner plate, in this case from a methane - air flame at $\phi = 1.2$, measured with the thermophosphor technique is shown in figure 8.9 (right). The results are shown in table 8.3, in which uncertainties are included. As can be seen in the table, there are some differences

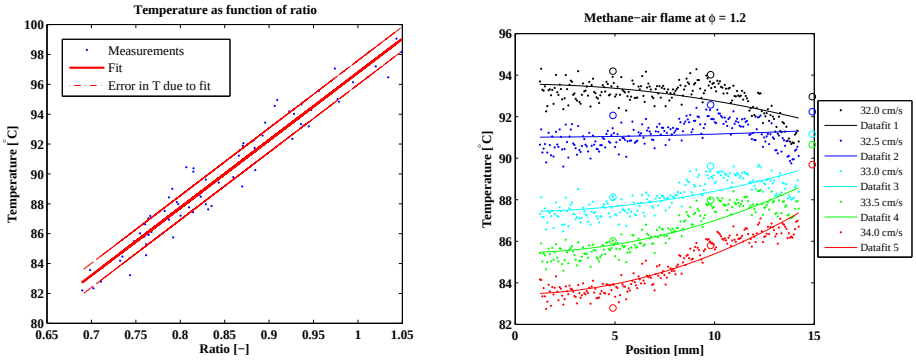

Figure 8.9. (Left) Calibration curve between calculated ratios and corresponding temperature from thermocouples, obtained during heat flux measurements. The graph shows the data points, the linear curve fit and the standard deviation of the fit. (Right) A typical temperature distribution over the burner plate, in this case from a methane - air flame at $\phi = 1.2$, measured with use of the thermophosphor technique.

Table 8.3. Measured laminar burning velocities of methane - air flames with the standard heat flux method, as well as with the new thermophosphor measurements.

Equivalence ratio ϕ [-]	Standard heat flux S_L [cm/s]	TP Measurements S_L [cm/s]
0.700 ± 0.015		18.6 ± 0.51
0.800 ± 0.013	26.5 ± 0.44	25.5 ± 0.41
0.900 ± 0.014	32.5 ± 0.44	32.2 ± 0.21
1.000 ± 0.014	35.9 ± 0.27	36.2 ± 0.26
1.100 ± 0.015	35.9 ± 0.27	36.7 ± 0.22
1.200 ± 0.017	30.7 ± 0.37	32.9 ± 0.29
1.300 ± 0.021	25.4 ± 0.40	24.8 ± 0.32

in the values of the laminar burning velocity. Besides that, the uncertainty in S_L is about 0.05 cm/s smaller for the thermophosphor measurements than for the standard heat flux measurements. In order to judge these results, they are plotted against literature values from the theses of Hermanns [17] and Bosschaart [20], who used the standard heat flux measurements. The relation between the equivalence ratio and laminar burning velocity is shown in figure 8.10.

One can see that there is a spread in all the values. They are closest at $\phi = 1.0$ in which the heat transfer is close to its maximum and the sensitivity of the

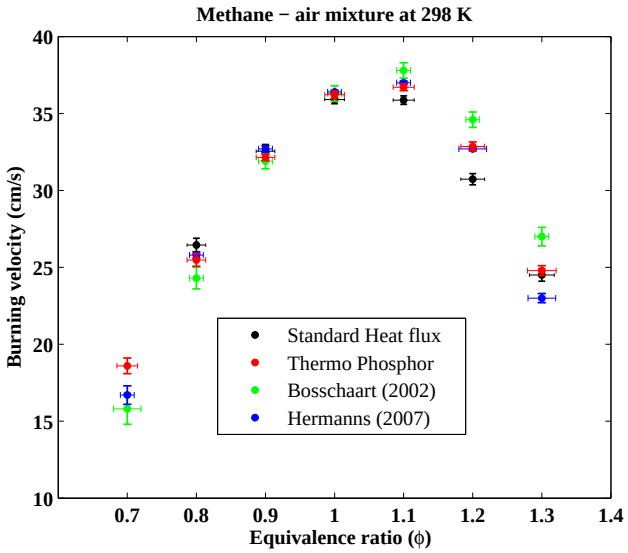

Figure 8.10. Plot of the measured laminar burning velocity as a function of the equivalence ratio, measured with the standard heat flux method and the method with the thermophosphor measurement. Besides that, also the literature values of Hermanns [17] and Bosschaart [20] are shown. The measurements were performed with unburnt gas temperatures of 25°C.

method is the best. In this region, the uncertainties in the measurements are the smallest too. The results of the measured S_L with the thermophosphor measurements are in most cases somewhere in between those of Hermanns [17] and Bosschaart [20] or atleast close to them. The standard heat flux measurements, in contrary, differ more from the literature values. From this comparison, one can state that the results of the thermophosphor measurements look reasonable, because they are close to literature values. The uncertainties are smaller than those of standard heat flux measurements, but the improvement is not significant yet and the quality of the new setup has to be improved to become really of added value.

Thermophosphor measurements in combination with the heat flux method performed by Li et al. [142] resulted in smaller errors ($\sigma_{S_L} \approx 0.25$ cm/s at $\phi = 0.7$) than achieved with the present setup. Although these measurements were performed at higher unburnt gas temperatures (near 45 °C) and therefore not directly comparable, it is remarkable how well their measurement points coincide with the parabolic fit they made. Especially if one considers that the temperature profiles in our measurements are averaged values over many points per radius. In the present measurements, however, some problems were encoun-

tered, which are described in the following section with suggestions of possible improvements. When these problems are solved, the spread in data points is expected to be smaller and the sine-like behavior in the temperature profiles should be decreased. Therefore, it is expected that the total accuracy of these measurements can be increased.

8.4 Possible Improvements

Quite some problems occurred during the thermophosphor measurements and by reducing them, the method can be made more accurate. The analysis of the errors in the measurement lead to the conclusion that chromatic aberrations in the prism cause a non-uniform light distribution over the CCD chip of the camera. Because of that, a sine-like behavior appears in the 2D temperature distribution over the plate. To reduce this effect, the edge filter could be replaced by a band pass filter. Such a filter transmits a narrower band of wavelengths and would therefore result in less chromatic aberrations. Another option is to replace our self-made prism by a commercially available stereoscope, of which the working principle is based on the reflections by mirrors. Reflections are not wavelength dependent and would therefore prevent the occurrence of chromatic aberrations. In our current setup, there is no notch filter to filter out the reflections of the laser light. It might be useful to add such a filter to the setup.

It was also seen that the intensity of the laser influences the emission of the phosphor material. An inhomogeneous laser profile therefore leads to ratio differences over the plate, even if it is at a uniform temperature. Although a correction can be made for this, it would be preferred to optimize the laser profile itself. We used a piece of scotch-tape for it, which worked remarkably well, but a beam homogenizer might lead to even better results.

Due to time restraints, some issues were not studied well enough. The calibration curve between ratio and temperature that has been made is not very accurate, as the linear fit through it has a standard deviation with the data points of about 0.8°C. The relation appears to be linear now, but there might be a possibility that this line is not entirely straight, which cannot be seen from our measurements. A more sophisticated calibration method could be designed to increase the accuracy of the calibration.

The burner plate was coated with use of an airbrush and the result is satisfying. The layer seems homogeneous and the holes are not filled with the zinc/paint mixture. The exact thickness remains unknown and it is hard to coat a second

plate with exactly the same properties. The coating, however, could influence the results and therefore it is interesting to optimize the thickness of it. This might not be possible with use of the airbrush method, so a different way to coat the plate has to be thought of. One opportunity for this is to coat the plate with the electrophoresis method. By changing the composition of the mixture or the time for deposition, different layer thicknesses can be achieved. We were unable to test this method, but according to Jeon [155], it should be promising. Once the thickness of the coating can be investigated, it is also advisable to make a simple model to study the influence of the coating on the heat transfer in the burner plate.

An optimization could also be performed for the laser power. We studied the effect of the laser power on the intensity ratio globally and it was found that the intensity of the beam influenced the calculated ratio. It was, however, not investigated whether the sensitivity or accuracy of the method changes with a change in laser power.

In terms of data processing, one could take a look into the fact that the images of the burner plate are not entirely circular because the camera is positioned at an angle with respect to the burner. This effect is not large and in the current program, a simple correction is made for it. It could be investigated whether this correction has to be improved even more, but because the assumption is made that the temperature difference between neighboring pixels is small, this should not lead to a large error in the results.

If all of the improvements on the method are carried out, the real quality of the method can be judged and one can choose to go on with it or not. If the accuracy is still not satisfying, there is a possibility to replace the spectral ratio method by a lifetime method, as explained in chapter 8.1. This method is reported to be more accurate than the ratio method and has some major advantages [147]. The downside of this method is the requirement of a high speed camera with sufficient spatial resolution and the need for a more complex method for data processing.

Besides the use of a thermophosphor method for measuring the laminar burning velocity, it can also be used to study the uniformity of the temperature profile over the burner plate. If the temperature distribution over the plate is not symmetrical, the theory behind the heat flux method has to be adapted to become more accurate. Furthermore, the thermophosphor measurements are not restricted to the heat flux method. The method seems to be very suitable for surface measurements in environments where it is not possible to use for

example thermocouples.

Summary

Measurements with the new thermophosphor technique were performed for methane - air flames with equivalence ratios(ϕ) between 0.7 and 1.3. Images of the phosphorescent emission from the coated burner plate were made for several settings of the gas velocity and all of them were corrected for background effects and pixel dependent sensitivities. The two images of the burner plate, split by the prism, were aligned and the intensity ratio of each corresponding pixel was calculated. A special watershed grid is used to distinguish between pixels on the burner plate and pixels in the holes. Ratios were translated into temperatures with use of a calibration curve and the profile over the burner plate was calculated for each setting of the gas velocity. In the next step, a parabolic fit is made through each temperature distribution, from which the laminar burning velocity could be calculated. The values for the laminar burning velocities that resulted from the thermophosphor measurements were compared with the results of standard heat flux measurements. An error analysis was also part of this comparison. Although there are some differences in the measured values with respect to literature values, the results look reasonable. At this moment, however, the uncertainty in the laminar burning velocity did not significantly decrease due to the application of the thermophosphor measurements. For the new method to be of added value, the uncertainty should be reduced even more.

CHAPTER 9

Conclusions & Future Work

Conclusions

The laminar burning velocity is a combustion property of a fuel-oxidizer mixture and is a function of pressure, temperature and equivalence ratio of the mixture. This property is utilized in stability, flashback and blow-off studies for burner designs. Along with that, the laminar burning velocity is also used in validating chemical reaction mechanisms which are necessary input to numerical simulations of combustion systems like the combustion chamber (including burner) of a gas turbine. Many technologies like, the Integrated Gasification Combined Cycle operates gas turbines at elevated pressures and temperatures to attain increased plant efficiency. The objective of this study was to investigate laminar flames at elevated pressures and determine laminar burning velocity of various fuels using the heat flux method.

One-dimensional, adiabatic, stretchless flat flames were stabilized on a heat flux method burner. Along with outlining the principle and operation of an atmospheric heat flux method system, numerical simulations were performed to understand the effect of pressure on the flat flame and how geometry of a perforated burner plate used in the experiments affects the flame.

A complete high pressure experimental facility was developed in order to perform experiments at elevated pressure. The facility includes two setups, one rated for operations below 10 bar and the other rated up to 30 bar. The experiments were performed using the heat flux method in the present work to determine laminar burning velocity of certain compositions of syngas (H_2/CO/N_2) and lower alkanes (C1-C3). For alkanes, the results were obtained for pressures up to 5 atm, 298 K and equivalence ratio from 0.8 to 1.4. An elaborate analysis of pressure dependence of methane-air mixtures is included with correlations. A similar but brief study is presented for ethane-air and propane-air mixtures. Experiments for syngas mixtures (50:50 H_2-CO, 85:15 H_2-CO and 85:15 H_2-N_2) were conducted for pressures up to 10 atm, 298 K and lean conditions (equivalence ratio down to 0.5) since such data is very scarce in the literature. The results obtained have uncertainties lower than other methods used in the literature [9, 11, 1].

A chemical reaction mechanism dedicated to syngas mixtures was updated and validated with the obtained experimental results and those from literature for a wide range of pressure, temperature and equivalence ratio. The proposed mechanism performs well at these conditions when compared to other mechanisms from literature [94, 77, 83, 27] and is appropriate for gas turbine combustion simulations.

In addition to the study of extending the heat flux method to elevated pressure, an attempt was made to introduce an unconventional thermophosphor technique in measuring burner plate temperature to increase the accuracy of the heat flux method system. An optical setup is designed to incorporate the spectral ratio method which relates image intensity to temperature of a surface. The flame is stabilized on a burner plate which is coated with Zn:ZnO phosphor. Conventional heat flux method experiments of methane-air mixture using thermocouples were compared to the thermophosphor experiments. The accuracy of the system with thermophosphor technique was similar to that of conventional system. From further analysis of the measurement procedure it was concluded that a few modifications in the optical setup can assist in improving the accuracy of the measurements to make it superior to the traditional method.

Future scope

The study of laminar flames at elevated pressure remains an interesting topic of research. Many of the applications in the present scenario make use of high

pressure conditions for efficient operations. An understanding of the properties of flames at such conditions can assist technology in many ways. Such an understanding among the combustion community is still scarce and needs great deal of research. In line with the present work, many other fuels gaseous (mixtures) and liquid, can be investigated at high pressure. Applications like IC engines use a wide variety of liquid fuels (and additives) which still need attention in property determination. Another interesting direction can be to measure burning velocity at higher temperature together with higher pressure at lean and rich conditions.

The heat flux method applied in the present work is capable for high pressure measurements. Since, this method is new to the research community, more high pressure investigations are required in defining the extent to which this method is applicable. According to the author, the research in this field can be steered in the following directions:

- The heat flux method can be further assessed at higher pressure by using different burner plate configurations. The dimensions of the plate can be modified according to the suggestions made in chapter 3. Numerical simulations of the kind presented in this thesis can be applied for other fuels and conditions as well.
- One of the limitations of the heat flux method, at this stage, is the upper limit of gas velocities (around 70 cm/s) that can be used in the current burner. Again, a reassessment of burner plate dimensions is required to find a higher limit.
- The syngas/high-H_2 syngas measurements performed in the present study were mostly limited to lean mixtures. Investigation of stoichiometric and rich flames with a variety of oxidizer compositions can be carried out. In case of rich flames, instability can be anticipated as reported in literature [4]. Argon or CO_2 is the most commonly used diluent in the oxidizer for rich mixtures. Apart from this, all these mixtures can be burnt at even higher pressures with the right oxidizer compositions and equivalence ratio.
- Possible improvements can be applied to the thermophosphor HFM measurements reported in this thesis. The edge filter used in the present measurements can be replaced by a band pass filter. There is a possibility of replacing the spectral ratio method by the lifetime method also. The thermophosphor technique can be used to study the uniformity of the temperature profile over the burner plate.

APPENDIX A

Tabulated Experimental Results

Table A1. Laminar burning velocity measurements of methane - air mixtures at 298 K using heat flux method. β_1 as in eq. 5.1, derived from the experimental results are also presented.

P [atm]	ϕ=0.8	ϕ=0.9	ϕ=1	ϕ=1.1	ϕ=1.2	ϕ=1.3	ϕ=1.4
1	26.6±0.5	32.5±0.6	35.9±0.7	35.9±0.7	30.8±0.6	25.4±0.5	17.1±0.3
1.5	18.4±0.4	25.9±0.5	30.0±0.6	30.5±0.6	25.9±0.5	19.8±0.4	15.4±0.4
2	17.8±0.4	24.4±0.5	27.7±0.5	27.8±0.5	22.9±0.4	17.0±0.4	12.3±0.3
2.5	16.8±0.4	22.7±0.4	25.5±0.5	25.7±0.5	21.4±0.4	14.6±0.3	10.5±0.3
3	15.9±0.3	20.9±0.4	23.7±0.4	23.9±0.4	20.0±0.4	12.9±0.3	9.3±0.2
3.5	15.0±0.3	19.6±0.4	22.4±0.4	22.6±0.4	18.5±0.3	12.3±0.3	8.6±0.2
4	14.4±0.3	18.6±0.4	21.5±0.4	21.5±0.4	17.4±0.3	11.5±0.3	-
4.5	13.8±0.3	17.7±0.3	21.0±0.4	20.37±0.4	16.2±0.3	10.8±0.2	-
5	13.0±0.3	17.4±0.3	-	19.6±0.4	15.3±0.3	10.5±0.2	-
β_1	-0.476	-0.405	-0.373	-0.373	-0.417	-0.580	-0.511

Table A2. Laminar burning velocity measurements of ethane - air mixtures at 298 K using heat flux method. β_1 as in eq. 5.1, derived from the experimental results are also presented.

P [atm]	ϕ=0.8	ϕ=0.9	ϕ=1	ϕ=1.1	ϕ=1.2	ϕ=1.3
1	31.2±0.6	36.1±0.7	39.8±0.8	41.9±0.8	39.8±0.8	35.6±0.7
2	23.0±0.5	28.0±0.5	31.5±0.6	35.0±0.7	34.0±0.7	30.0±0.6
3	19.0±0.5	24.0±0.5	28.0±0.6	31.5±0.7	31.3±0.7	26.5±0.6
4	18.0±0.4	23.0±0.5	27.0±0.6	-	-	-
5	16.6±0.4	-	-	-	-	-
β_1	-0.413	-0.349	-0.309	-0.259	-0.221	-0.262

Table A3. Laminar burning velocity measurements of propane - air mixtures at 298 K using heat flux method. β_1 as in eq. 5.1, derived from the experimental results are also presented.

P [atm]	ϕ=0.8	ϕ=0.9	ϕ=1	ϕ=1.1	ϕ=1.2	ϕ=1.3
1	29.4±0.6	35.3±0.7	39.6±0.8	40.2±0.8	38.2±0.8	32.7±0.7
2	21.5±0.5	26±0.6	29.9±0.6	33.5±0.7	30.0±0.6	25.5±0.6
3	19.0±0.5	24.2±0.6	28.2±0.6	29.7±0.7	28.0±0.7	22.5±0.5
4	17.9±0.5	23.1±0.5	27.0±0.6	28.0±0.6	-	-
β_1	-0.387	-0.345	-0.311	-0.266	-0.305	-0.347

Table A4. Experimental conditions and results for H_2-CO mixtures.

T	P	ϕ	X_{H_2}	X_{CO}	X_{O_2}	X_{N_2}	X_{He}	S_L	σ_{S_L}
(K)	(atm)	(-)	Fuel		Oxidizer			(cm/s)	(cm/s)
298	1	0.6	0.5	0.5	0.21	0.79	0	42.5	2
298	1	0.62	0.5	0.5	0.21	0.79	0	46.0	2
298	1	0.64	0.5	0.5	0.21	0.79	0	50.5	2
298	1	0.66	0.5	0.5	0.21	0.79	0	52.5	2.5
298	1	0.68	0.5	0.5	0.21	0.79	0	56.0	2.5
298	1	0.7	0.5	0.5	0.21	0.79	0	59.0	3
298	1	0.72	0.5	0.5	0.21	0.79	0	63.0	3
298	1	0.74	0.5	0.5	0.21	0.79	0	65.0	3.5
298	1	0.76	0.5	0.5	0.21	0.79	0	68.0	3.5
298	1	0.78	0.5	0.5	0.21	0.79	0	72.0	4
298	1	0.8	0.5	0.5	0.21	0.79	0	76.0	4
298	1	0.7	0.5	0.5	0.1	0	0.9	55.1	3
298	1.5	0.7	0.5	0.5	0.1	0	0.9	49.9	2.5
298	2	0.7	0.5	0.5	0.1	0	0.9	47.0	2.5
298	2.5	0.7	0.5	0.5	0.1	0	0.9	43.8	2
298	3	0.7	0.5	0.5	0.1	0	0.9	41.1	2
298	3.5	0.7	0.5	0.5	0.1	0	0.9	38.0	2
298	4	0.7	0.5	0.5	0.1	0	0.9	35.1	2
298	4.5	0.7	0.5	0.5	0.1	0	0.9	33.9	2.5
298	5	0.7	0.5	0.5	0.1	0	0.9	32.1	2.5
298	1	1	0.5	0.5	0.1	0.9	0	19.1	1
298	1.5	1	0.5	0.5	0.1	0.9	0	15.5	1.9
298	2	1	0.5	0.5	0.1	0.9	0	14.8	1.5
298	2.5	1	0.5	0.5	0.1	0.9	0	13.3	1.1
298	3	1	0.5	0.5	0.1	0.9	0	13.7	1
298	3.5	1	0.5	0.5	0.1	0.9	0	11.7	0.9
298	4	1	0.5	0.5	0.1	0.9	0	11.0	0.7

Table A5. Experimental conditions and results for H_2-CO mixtures.

T	P	ϕ	X_{H_2}	X_{CO}	X_{O_2}	X_{N_2}	X_{He}	S_L	σ_{S_L}
(K)	(atm)	(-)	Fuel		Oxidizer			(cm/s)	(cm/s)
298	1	0.7	0.5	0.5	0.15	0.85	0	22.1	1
298	1.5	0.7	0.5	0.5	0.15	0.85	0	18.7	2.2
298	2	0.7	0.5	0.5	0.15	0.85	0	17.5	1.6
298	2.5	0.7	0.5	0.5	0.15	0.85	0	16.3	1.3
298	3	0.7	0.5	0.5	0.15	0.85	0	15.7	1.1
298	3.5	0.7	0.5	0.5	0.15	0.85	0	14.9	1
298	1	0.6	0.5	0.5	0.125	0	0.875	62.5	8
298	2	0.6	0.5	0.5	0.125	0	0.875	50.0	5.1
298	3	0.6	0.5	0.5	0.125	0	0.875	43.9	4
298	4	0.6	0.5	0.5	0.125	0	0.875	42.1	3.3
298	5	0.6	0.5	0.5	0.125	0	0.875	39.5	2.9
298	6	0.6	0.5	0.5	0.125	0	0.875	37.0	2.6
298	7	0.6	0.5	0.5	0.125	0	0.875	34.8	2.2
298	8	0.6	0.5	0.5	0.125	0	0.875	33.5	1.9
298	9	0.6	0.5	0.5	0.125	0	0.875	32.0	1.7
298	1	0.7	0.85	0.15	0.15	0.85	0	37.2	2.2
298	1.5	0.7	0.85	0.15	0.15	0.85	0	32.9	2
298	2	0.7	0.85	0.15	0.15	0.85	0	29.0	1.5
298	2.5	0.7	0.85	0.15	0.15	0.85	0	27.0	1.5
298	3	0.7	0.85	0.15	0.15	0.85	0	24.1	1.3
298	3.5	0.7	0.85	0.15	0.15	0.85	0	23.0	1
298	4	0.7	0.85	0.15	0.15	0.85	0	21.5	1

Table A6. Experimental conditions and results for H_2-CO mixtures.

T	P	ϕ	X_{H_2}	X_{CO}	X_{O_2}	X_{He}	S_L	σ_{S_L}
(K)	(atm)	(-)	Fuel		Oxidizer		(cm/s)	(cm/s)
298	1	0.5	0.85	0.15	0.12	0.88	58.2	3
298	2	0.5	0.85	0.15	0.12	0.88	38.1	2.8
298	3	0.5	0.85	0.15	0.12	0.88	32	2.5
298	4	0.5	0.85	0.15	0.12	0.88	24.2	1.9
298	5	0.5	0.85	0.15	0.12	0.88	19.7	1.6
298	6	0.5	0.85	0.15	0.12	0.88	16.0	1.6
298	7	0.5	0.85	0.15	0.12	0.88	12.5	1.5
298	8	0.5	0.85	0.15	0.12	0.88	10.5	1.3
298	1	0.6	0.85	0.15	0.11	0.89	68.1	3
298	1.5	0.6	0.85	0.15	0.11	0.89	60.0	2.5
298	2	0.6	0.85	0.15	0.11	0.89	53.9	2.5
298	2.5	0.6	0.85	0.15	0.11	0.89	50.5	2
298	3	0.6	0.85	0.15	0.11	0.89	47.3	2
298	3.5	0.6	0.85	0.15	0.11	0.89	44.1	2
298	4	0.6	0.85	0.15	0.11	0.89	40.2	2
298	4.5	0.6	0.85	0.15	0.11	0.89	38.5	2
298	5	0.6	0.85	0.15	0.11	0.89	35.5	1.5
298	1	0.5	0.85	0.15	0.125	0.875	60.1	3
298	2	0.5	0.85	0.15	0.125	0.875	45.0	2.5
298	3	0.5	0.85	0.15	0.125	0.875	35.6	2
298	4	0.5	0.85	0.15	0.125	0.875	30.4	2
298	5	0.5	0.85	0.15	0.125	0.875	25.5	2
298	6	0.5	0.85	0.15	0.125	0.875	21.5	2
298	7	0.5	0.85	0.15	0.125	0.875	17.4	1.5
298	8	0.5	0.85	0.15	0.125	0.875	15.0	1.5
298	9	0.5	0.85	0.15	0.125	0.875	12.5	1.5
298	10	0.5	0.85	0.15	0.125	0.875	11.1	1.5

Table A7. Experimental conditions and results for H_2-N_2 mixture.

T	P	ϕ	X_{H_2}	X_{N_2}	X_{O_2}	X_{He}	S_L	σ_{S_L}
(K)	(atm)	(-)	Fuel		Oxidizer		(cm/s)	(cm/s)
298	1	0.5	0.85	0.15	0.125	0.875	61.9	3
298	2	0.5	0.85	0.15	0.125	0.875	48.1	2.5
298	3	0.5	0.85	0.15	0.125	0.875	38.0	2
298	4	0.5	0.85	0.15	0.125	0.875	31.2	2
298	5	0.5	0.85	0.15	0.125	0.875	22.9	2
298	6	0.5	0.85	0.15	0.125	0.875	18.1	2
298	7	0.5	0.85	0.15	0.125	0.875	15.0	1.5
298	8	0.5	0.85	0.15	0.125	0.875	11.0	1.5
298	9	0.5	0.85	0.15	0.125	0.875	8.5	1.5
298	10	0.5	0.85	0.15	0.125	0.875	6.5	1.5

APPENDIX B

CHEM1D

The in-house flame code CHEM1D used in this thesis is explained in this section. The combustion of gases is governed by a set of equations describing the conservation of mass, momentum, energy and species mass fractions. In the thesis of Hermanns [17] the general set of conservation equations used in CHEM1D is presented, together with the transport and chemistry models and the state equations for specific enthalpy and density. These equations are put into a 1D formulation and since the 1D at flames are stationary, the terms involving $\frac{\partial}{\partial \mathrm{t}}$ are zero. The equations are simplified with the assumptions of no bulk viscosity, no body forces, ideal gas behavior of the mixture and no radiative heat losses. Further simplification with an approximation for low Mach number reactive flows show that the pressure in the energy equation can be treated as spatially constant. Also the energy dissipation by viscous forces in the energy equation can be neglected. With these assumptions, the governing equations can be simplified by omitting the momentum equation [17]. Only the remaining conservation equations (mass, energy and species) are presented here, written in the form in which they are implemented in CHEM1D. This set of differential equations uses equation B.1 to determine the density.

Equation of state

$$\rho = \frac{\mathrm{p}_0 \overline{\mathrm{M}}}{\mathrm{RT}} \tag{B.1}$$

where ρ is the mixture mass density, $\mathrm{p_0}$ the ambient pressure, $\overline{\mathrm{M}}$ the mean molar mass, R the universal gas constant and T the temperature.

Conservation of mass

$$\frac{\partial}{\partial \mathrm{x}}(\rho \mathrm{v}) = 0 \tag{B.2}$$

where v is the gas mixture velocity.

Energy conservation equation

$$\frac{\partial}{\partial \mathrm{x}}(\rho \mathrm{vh}) = \frac{\partial}{\partial \mathrm{x}}(\frac{\lambda'}{\mathrm{c_p}}\frac{\partial \mathrm{h}}{\partial \mathrm{x}}) - \frac{\partial}{\partial \mathrm{x}}(\rho \sum_{\mathrm{i}=1}^{\mathrm{N_s}} \mathrm{U_i Y_i h_i}) + \frac{\partial}{\partial \mathrm{x}}(\mathrm{p} \sum_{\mathrm{i}=1}^{\mathrm{N_s}} \mathrm{D_i^T d_i}) \tag{B.3}$$

where h is the specific enthalpy, λ' the thermal conductivity, $\mathrm{c_p}$ the specific heat capacity at constant pressure, $\mathrm{N_s}$ the number of species, $\mathrm{U_i}$ the diffusion velocity of species i, $\mathrm{Y_i}$ the mass fraction of species i and $\mathrm{h_i}$ the enthalpy of species i. The last term represents the Dufour effect (the development of a temperature gradient due to diffusion), with p the pressure, $\mathrm{D_i^T}$ the thermal diffusion coefficient and $\mathrm{d_i}$ incorporates the effects of various gradients and external forces. The Soret effect is incorporated in the term $\mathrm{U_i}$, see equation E.5. It describes the effect that light species tend to go to parts in the flame with higher temperature and heavier species tend to go to colder parts [17].
Species conservation equation

$$\frac{\partial}{\partial \mathrm{x}}(\rho \mathrm{v Y_i}) + \frac{\partial}{\partial \mathrm{x}}(\rho \mathrm{U_i Y_i}) = \omega_\mathrm{i}', \mathrm{i}\epsilon[1, \mathrm{N_s} - 1] \tag{B.4}$$

where ω_i' is the chemical source term, which is characteristic for the reactive nature of the flow.

The above equation only needs to be solved for $\mathrm{N_s} - 1$ species (where $\mathrm{N_s}$ is the total number of species) since the mass fraction of one of the species can be solved using the constraint that the sum of all the species mass fractions equals 1.

$$\sum_{\mathrm{i}=1}^{\mathrm{N_s}} \mathrm{Y_i} = 1 \tag{B.5}$$

To minimize the numerical error, the species that is present in abundance is chosen for this species. In case of methane-air mixtures, this is nitrogen.

In order to solve the set of differential equations listed above, a set of boundary conditions is required. At the unburned and the burned side of the flame, boundary conditions for species and enthalpy are used. At the unburned side ($\mathrm{x} = -\infty$) a Dirichlet type of boundary conditions is used:

$$h = h_u \tag{B.6}$$

$$Y_i = Y_{i,u} \tag{B.7}$$

At the burned side ($x = \infty$) a Neumann type of boundary condition is used:

$$\frac{\partial h}{\partial x} = 0 \tag{B.8}$$

$$\frac{\partial Y_i}{\partial x} = 0 \tag{B.9}$$

CHEM1D uses a second order finite volume approach to discretize the conservation equations. The resulting nonlinear algebraic equations are solved using a fully implicit modified Newton method [19]. To solve this set of differential equations to determine the adiabatic burning velocity, the steady-state boundary value method is used. This method uses a frame of reference which is moving equally to the adiabatic burning velocity by fixing the temperature at one point. The mass flow rate ρu now becomes an eigenvalue of the set of differential equations. The resulting mass flow rate equals the mass flow rate of an adiabatic flame, resulting in $\rho_u u_u = \rho_u S_L$ from which the S_L can be calculated [17].

The domain dimensions are from x = -2 to 10 cm with 300 grid points. An adaptive gridding procedure is implemented in CHEM1D to increase the accuracy in the flame front [19]. This procedure places approximately 80% of the grid points in the area with the largest gradients (the flame front).

Nomenclature

A	Area (m^2)
A_p	Pre-exponential factor
c	Speed of light (m/s)
C1	Methane
C2	Ethane
C3	Propane
d	Hole diameter (mm)
E	Total specific energy (KJ/kg)
E_a	Activation energy (KJ/mol)
$E(n, \upsilon, J)$	Specific internal energy of a given state (J)
$\vec{F}$	External body forces (N)
$g_{n\upsilon J}$	Degeneracy factor of each energy level
h	Sensible energy
I	Intensity
$\vec{J_i}$	Diffusion flux of species (kg m^{-2} s^{-1})
k	Thermal conductivity (W/m.K)
k_r	Rate of reaction (mol cm^{-3} s^{-1})
k_B	Boltzmann constant (J K^{-1})
K	Flame stretch rate (s^{-1})
m	Mass (kg)
n	Overall reaction order (-)
n, υ, J	quantum numbers (-)
$N(n, \upsilon, J)$	Amount of molecules in a specific state (-)
N_0	Total number of molecules (-)
N_s	Total number of species (-)
p	Static pressure
P	Pressure (Pa)
P_0	Reference pressure (Pa)
$q(r)$	Net heat transfer from the gas to the burner plate (W)
Q_t	Total volume flow rate (ln/min)
r_b	Radius of the burner plate (mm)
R_i	Volumetric rate of creation of species i

$\mathrm{R_{CH_4}}$	Net reaction rate of methane (mol cm^{-3} s^{-1})
R	Gas constant (KJ/kg.K)
s	Sensitivity (K.s/mm^3)
$\mathrm{s'}$	Pitch (mm)
$\mathrm{S_L}$	Laminar burning velocity (cm/s)
$\mathrm{S_{L0}}$	Laminar burning velocity at reference conditions (cm/s)
$\mathrm{S_{incr}}$	Surface area increase (%)
$\mathrm{S_h}$	Source term which includes the heat of chemical reaction
t	Time (s)
T	Temperature (K)
$\mathrm{T_0}$	Reference temperature (K)
$\mathrm{T_{iso}}$	Temperature isotherm (K)
$\mathrm{T_p}$	Temperature of the burner plate (K)
$\mathrm{T_g}$	Temperature of the gas (K)
$\mathrm{U_g}$	Unburnt gas velocity (cm/s)
v	Gas mixture velocity (cm/s)
$\mathrm{v_u}$	Unburnt gas velocity (cm/s)
$\mathrm{X_{H_2}}$	Mole fraction of H_2 in fuel (-)
$\mathrm{X_{CO}}$	Mole fraction of CO in fuel (-)
$\mathrm{X_{O_2}}$	Mole fraction of O_2 in oxidizer (-)
$\mathrm{X_{N_2}}$	Mole fraction of N_2 in oxidizer or fuel (-)
$\mathrm{X_{He}}$	Mole fraction of He in oxidizer (-)
$\mathrm{Y_i}$	Mass fraction of species i
$\mathrm{Z(T)}$	Partition function
α_1	Temperature power exponent (-)
β_1	Pressure power exponent (-)
β_2	Pressure correlation coefficient (-)
γ	Parabolic coefficient (K/mm^2)
ϕ	Equivalence ratio (-)
α	Half cone angle ($^\circ$)
$\lambda_{\mathrm{p,x}}$	Thermal conductivity of the burner plate in axial direction x (W/m.K)
$\lambda_{\mathrm{p,r}}$	Thermal conductivity of the burner plate in radial direction r (W/m.K)
α_{gb}	Volumetric heat transfer coefficient between the gas and the burner plate
$\Delta\mathrm{m'}$	Error in mass flow rate (kg/s)
$\sigma_{\mathrm{S_L}}$	Error in S_L (cm/s)
σ_{tc}	Thermocouple scatter(K)
χ	Porosity of burner plate (-)
ρ	Density (kg/m^3)
$\overline{\overline{\tau}}$	Stress tensor (kg m^{-1} s^{-2})
$\rho\vec{\mathrm{g}}$	Gravitational body force (N)
τ	Time step (s)
h	Planck's constant (Js)
ν	Frequency (s^{-1})
λ	Wavelength (nm)

Bibliography

[1] J. Natarajan, Y. Kochar, T. Lieuwen, and J. Seitzman. Pressure and preheat dependence of laminar flame speeds of $H_2/CO/CO_2/O_2$/He mixtures. *Proc Combust. Inst.*, 32:1261–1268, 2009.

[2] S. Turns. *An Introduction to Combustion*. McGraw Hill, 2000.

[3] R.T.E. Hermanns, A.A. Konnov, R.J.M. Bastiaans, L.P.H. de Goey, K. Lucka, and H. Köhne. Effects of temperature and composition on the laminar burning velocity of $CH_4 + H_2 + N_2$ flames. *Fuel*, 89:114–121, 2010.

[4] M.P. Burke, M. Chaos, F.L. Dryer, and Y. Ju. Negative pressure dependence of mass burning rates of $H_2/CO/O_2$/diluent flames at low flame temperatures. *Combust. Flame*, 157:618–631, 2010.

[5] M. Goswami, S. Derks, K. Coumans, W.J. Slikker, M.H. de Andrade Oliveira, R.J.M Bastiaans, C.C.M. Luijten, L.P.H. de Goey, and A.A. Konnov. The effect of elevated pressures on the laminar burning velocity of methane + air mixtures. *Combust. Flame*, 160:1627–1635, 2013.

[6] O. Park, P.S. Veloo, N. Liu, and F.N. Egolfopoulos. Combustion characteristics of alternative gaseous fuels. *Proc. Combust. Inst.*, 33:887–894, 2010.

[7] H. Sun, S.I. Yang, G. Jomaas, and C.K. Law. High-pressure laminar flame speeds and kinetic modeling of carbon monoxide/hydrogen combustion. *Proc Combust. Inst.*, 31:439–446, 2007.

[8] F.N. Egolfopoulos, P. Cho, and C.K. Law. Laminar flame speeds of methane-air mixtures under reduced and elevated pressure. *Combust. Flame*, 76:375–391, 1989.

[9] C. Ji, E. Dames, Y.L. Wang, H. Wang, and F.N. Egolfopoulos. Propagation and extinction of premixed C_5-C_{12} n-alkane flames. *Combust. Flame*, 157:277–287, 2010.

[10] S.D. Tse, D.L. Zhu, and C.K. Law. Morphology and burning rates of expanding spherical flames in H_2/O_2/inert mixtures up to 60 atmospheres. *Proc. Combust. Inst.*, 28(2):1793–1800, 2000.

[11] B. Galmiche, F. Halter, and F. Foucher. Effects of high pressure, high temperature and dilution on laminar burning velocities and markstein lengths of iso-octane/air mixtures. *Combust. Flame*, 159:3286–3299, 2012.

[12] J. Powling. A new burner method for the determination of low burning velocities and limits of flammability. *Fuel*, 28(2):25–28, 1949.

[13] J.P. Botha and D.B. Spalding. The laminar flame speeds of propane/air

mixtures with heat extraction from the flame. *Proc. R. Soc. Lon. ser-A*, 255(II60):71–95, 1954.

[14] L.P.H. de Goey, A. van Maaren, and R.M. Quax. Stabilization of adiabatic premixed laminar flames on a flat flame burner. *Combust. Sci. Technol.*, 92:201–207, 1993.

[15] A. van Maaren. *One-step chemical reaction parameters for premixed laminar flames.* PhD thesis, University of Tec hnology Eindhoven, 1994.

[16] K.J. Bosschaart and L.P.H. de Goey. Detailed analysis of the heat flux method for measuring burning velocities. *Combust. Flame*, 132:170–180, 2003.

[17] R.T.E. Hermanns. *Laminar burning velocity of Methane-Hydrogen-Air Mixtures.* PhD thesis, Eindhoven University of Technology, 2007.

[18] A.A. Konnov, R. Riemeijer, and L.P.H. de Goey. Adiabatic laminar burning velocities of $\mathrm{CH_4} + \mathrm{H_2} +$ air flames at low pressures. *Fuel*, 89:1392–1396, 2010.

[19] L.M.T. Somers. *The simulation of flat flames with detailed and reduced chemical models.* PhD thesis, Eindhoven University of Technology, 1994.

[20] K.J. Bosschaart. *Analysis of the Heat Flux Method for Measuring Burning Velocities.* PhD thesis, University of Technology Eindhoven, 2002.

[21] Bronkhorst High Tech. 2011.

[22] A.A. Konnov, G. Puig Alvarez, I.V. Rybitskaya, and J. De Ruyck. The effects of enrichment by carbon monoxide on adiabatic burning velocity and nitric oxide formation in methane flames. *Combust. Sci. Technol.*, 1:117–135, 2009.

[23] L.P.H. de Goey, L.M.T. Somers, W.M.M.L. Bosch, and R.M.M. Mallens. Modeling of the small scale structure of flat burner-stabilized flames. *Combust. Sci. Technol.*, 104:387–400, 1995.

[24] Ansys fluent. *Academic Research Release 12.1*.

[25] M.D. Smooke. Reduced kinetic mechanisms and asymptotic approximation for methane-air flames. *Lecture notes in Physics, Springer Berlin*, 1991.

[26] A. Kazakov and M. Frenklach. Drm19. 1995.

[27] G.P. Smith, D.M. Golden, M. Frenklach, N.W. Moriarty, B. Eiteneer, M. Goldenberg, C.T. Bowman, R.K. Hanson, S. Song, W.C. Gardiner Jr, V.V. Lissianski, and Z. Qin. GRI-Mech 3.0, 1999.

[28] A.A. Konnov. Implementation of the NCN pathway of prompt-NO formation in the detailed reaction mechanism. *Combust. Flame*, 156:2093–2105, 2009.

[29] E. Hu, Z. Huang, J. He, and H. Miao. Experimental and numerical study on lean premixed methane-hydrogen-air flames at elevated pressures and temperatures. *Int. J Hydrogen Energy*, 34:6951, 2009.

[30] H. Kobayashi, T. Tamura, K. Maruta, and T. Niioka. Burning velocity of turbulent premixed flames in a high-pressure environment. *26th Symposium (International) on Combustion/The Combustion Institute*, pages 389–396, 1996.

[31] X. Qin, H. Kobayashi, and T. Niioka. Laminar burning velocity of hydrogen-air premixed flames at elevated pressure. *Experimental Thermal and Fluid Sc.*, 21:58, 2000.

[32] L. Ubbelohde and E. Koelliker. Information about the inner cone of the bunsen flame. *Journal fur Gasbeluchtung und Wasserversorgung*, 59:49–57, 1916.
[33] E. Mallard and H.L. Le Chatelier. Recherches expérimentales et théorétiques sur la combustion des mélanges gazeux explosifs. *Ann. Mines*, 8:274–295, 1883.
[34] E. Jouguet. *Compt. Rend. Acad. Sci., Paris*, 156:872, 1913.
[35] L. Crussard. *Compt. Rend. Acad. Sci., Paris*, 158:125, 1914.
[36] W. Nusselt. *Z. Ver. Deut. Ing.*, 59:872, 1915.
[37] P.J. Daniell. The theory of flame motion. *Proc. Roy. Soc. A*, 126:393, 1930.
[38] J. Zeldovich and D.A. Frank-Kamenetsky. *Compt. Rend. Acad. Sci. USSR*, 19:693, 1938.
[39] F.N. Egolfopoulos and C.K. Law. Chain mechanisms in the overall reaction orders in laminar flame propagation. *Combust. Flame*, 80:7–16, 1990.
[40] C. Rozenchan, D.L. Zhu, C.K. Law, and S.D. Tse. Outward propagation, burning velocities, and chemical effects of methane flames up to 60 atm. *Proc. Combust. Inst.*, 29:1461–1469, 2002.
[41] J.T. Agnew and L.B. Graiff. The pressure dependence of laminar burning velocity by the spherical bomb method. *Combust. Flame*, 5:209–219, 1961.
[42] S.P. Sharma, D.D. Agrawal, and C.P. Gupta. The pressure and temperature dependence of burning velocity in a spherical combustion bomb. *Proc. Combust. Inst.*, 18:493–501, 1981.
[43] T. Iijima and T. Takeno. Effects of temperature and pressure on burning velocity. *Combust. Flame*, 65:35–43, 1986.
[44] P.K. Bose, S.P. Sharma, and S. Mitra. Laminar burning velocity of methane-air mixture in the presence of a diluent. *Proc. of The 6th International Symposium on Transport Phenomena in Thermal Engineering, May, Seoul*, pages 648–653, 1993.
[45] A.E. Dahoe and L.P.H. de Goey. On the determination of the laminar burning velocity from closed vessel gas explosions. *J. Loss Prevention in Proc. Indust.*, 16:457–478, 2003.
[46] D. Smith and J.T. Agnew. The effect of pressure on the laminar burning velocity of methane-oxygen-nitrogen mixtures. *Proc. Combust. Inst.*, 6:83–88, 1957.
[47] V.S. Babkin and L.S. Kozachenko. Study of normal burning velocity in methane-air mixtures at high pressures. *Combust. Expl. Shock Waves*, 2:46–52, 1966.
[48] G.E. Andrews and D. Bradley. The burning velocity of methane-air mixtures. *Combust. Flame*, 19:275–288, 1972.
[49] H. Kobayashi, T. Nakashima, T. Tamura, K. Maruta, and T. Niioka. Turbulence measurements and observations of turbulent premixed flames at elevated pressures up to 3.0 MPa. *Combust. Flame*, 108:104–117, 1997.
[50] H. Eberius and Th. Kick. *Ber. Bunsenges. Phys. Chem.*, 96:1416–1419, 1992.
[51] A.M. Garforth and C.J. Rallis. Laminar burning velocity of stoichiometric

methane-air: Pressure and temperature dependence. *Combust. Flame*, 31:53–68, 1978.

[52] C.J. Rallis and A.M. Garforth. The determination of laminar burning velocity. *Prog. Energy Combust. Sci.*, 6:303–329, 1980.

[53] P.G. Hill and J. Hung. Laminar burning velocities of stoichiometric mixtures of methane with propane and ethane additives. *Combust. Sci. Technol.*, 60:7–30, 1988.

[54] R. Stone, A. Clarke, and P. Beckwith. Correlations for the laminar-burning velocity of methane/diluent/air mixtures obtained in free-fall experiments. *Combust. Flame*, 114:546–555, 1998.

[55] X.J. Gu, M.Z. Haq, M. Lawes, and R. Woolley. Laminar burning velocity and markstein lengths of methane-air mixtures. *Combust. Flame*, 121:41–58, 2000.

[56] M. Elia, M. Ulinski, and M. Metghalchi. *Trans. ASME*, 123:190–196, 2001.

[57] S.Y. Liao, D.M. Jiang, and Q. Cheng. Determination of laminar burning velocities for natural gas. *Fuel*, 83:1247–1250, 2004.

[58] F. Halter, C. Chauveau, N. Djebaili-Chaumeix, and I. Gokalp. Characterization of the effects of pressure and hydrogen concentration on laminar burning velocities of methane-hydrogen-air mixtures. *Proc. Combust. Inst.*, 30:201–208, 2005.

[59] G. Tsatsaronis. Prediction of propagating laminar flames in methane, oxygen, nitrogen mixtures. *Combust. Flame*, 33:217–239, 1978.

[60] N.Y. Shebeko, A.Y. Korolchenko, V.G. Shamonin, and S.G. Tsarichenko. Dependence of the normal rate of combustion of methane-air and hydrogen-air mixtures on pressure and composition. *Combust. Explos. Shock Waves*, 29:557–561, 1993.

[61] P. Han, M.D. Checkel, B.A. Fleck, and N.L. Nowicki. Burning velocity of methane/diluent mixture with reformer gas addition. *Fuel*, 86:585–596, 2007.

[62] P. Ouimette and P. Seers. Numerical comparison of premixed laminar flame velocity of methane and wood syngas. *Fuel*, 88:528–533, 2009.

[63] S. Bougrine, S. Richard, A. Nicolle, and D. Veynante. Numerical study of laminar properties of diluted methane-hydrogen-air flames at high pressure and temperature using detailed chemistry. *Int. J. Hydrogen Energy*, 36:12035–12047, 2011.

[64] H. Wang, X. You, A. Joshi, S.G. Davis, A. Laskin, F.N. Egolfopoulos, and C.K. Law. High-Temperature Combustion Reaction Model of H_2 / CO / C1-C4 Compounds. *USC Mech II*, 2007.

[65] I.V. Dyakov, A.A. Konnov, J. de Ruyck, K.J. Bosschaart, E.C.M. Brock, and L.P.H. de Goey. Measurement of adiabatic burning velocity in methane-oxygen-nitrogen mixtures. *Combust. Sci. Technol.*, 172:81–96, 2001.

[66] M.I. Hassan, K.T. Aung, and G.M. Faeth. Measured and predicted properties of laminar premixed methane/air flames at various pressures. *Combust. Flame*, 115:539, 1998.

[67] W. Lowry, J. de Vries, M. Krejci, E. Peterson, Z. Serinyel, W. Metcalfe, H. Cur-

ran, and G. Bourque. Laminar flame speed measurements and modeling of pure alkanes and alkane blends at elevated pressures. *J. Eng. Gas Turbines Power*, 133(9):091501–1–9, 2011.

[68] A.A. Konnov, I.V. Dyakov, and J. de Ruyck. Probe sampling measurements and modeling of nitric oxide formation in methane-air flames. *Combust. Sci. Technol.*, 169:127–153, 2001.

[69] A.A. Konnov. The effect of temperature on the adibatic laminar burning velocities of CH_4 -air and H_2-air flames. *Fuel*, 89:2211–2216, 2010.

[70] B. Yan, Y. Wu, C. Liu, J.F. Yu, B. Li, Z.S. Li, G. Chen, X.S. Bai, M. Alden, and A.A. Konnov. Experimental and modeling study of laminar burning velocity of biomass derived gases/air mixtures. *Int. J. Hydrogen Energy*, 36:3769–3777, 2011.

[71] K. Seshadri, X.S. Bai, and H. Pitsch. Asymptotic structure of rich methane-air flames. *Combust. Flame*, 127:2265–2277, 2002.

[72] C.M. Vagelopoulos and F.N. Egolfopoulos. Direct experimental determination of laminar flame speeds. *Symposium (International) on Combustion/The Combustion Institute*, 27:513–519, 1998.

[73] K.J. Bosschaart and L.P.H. de Goey. The laminar burning velocity of flames propagating in mixtures of hydrocarbons and air measured with the heat flux method. *Combust. Flame*, 136:261–269, 2004.

[74] G. Jomaas, X.L. Zheng, D.L. Zhu, and C.K. Law. Experimental determination of counterflow ignition temperatures and laminar flame speeds of C_2-C_3 hydrocarbons at atmospheric and elevated pressures. *Proc. Combust. Inst.*, 30:193–200, 2005.

[75] O. Park, P.S. Veloo, and F.N. Egolfopoulos. Flame studies of C_2 hydrocarbons. *Proc. Combust. Inst.*, 34:711–718, 2013.

[76] M.C. Krejci, O. Mathieu, A.J. Vissotski, S. Ravi, T.G. Sikes, E.L. Peterson, A. Kermones, W. Metcalfe, and H.J. Curran. Laminar flame speed and ignition delay time data for the kinetic modeling of hydrogen and syngas fuel blends. *J. Eng. Gas Turbines Power*, 135:0215031–0215039, 2013.

[77] A. Kéromnès, W.K. Metcalfe, K.A. Heufer, N. Donohoe, A.K. Das, C. Sung, J. Herzler, C. Naumann, P. Griebel, O. Mathieu, M.C. Krejci, E.L. Pertersen, W.J. Pitz, and H.J. Curran. An experimental and detailed chemical kinetic modeling study of hydrogen and syngas mixture oxidation at elevated pressures. *Combust. Flame*, 160:995–1011, 2013.

[78] I.C. McLean, D.B. Smith, and S.C. Taylor. The use of carbon monoxide/hydrogen burning velocities to examine the rate of the CO + OH reaction. *Proc Combust. Inst.*, 25:749–757, 1994.

[79] C. Prathap, A. Ray, and M.R. Ravi. Investigation of nitrogen dilution effects on the laminar burning velocity and flame stability of syngas fuel at atmospheric condition. *Combust. Flame*, 155:145–160, 2008.

[80] N. Bouvet, C. Chauveau, I. Gokalp, and F. Halter. Experimental studies of the fundamental flame speeds of syngas (H_2/CO)/air mixtures. *Proc. Combust.*

Inst., 33:913–920, 2011.

[81] B. Galmiche, F. Halter, F. Foucher, and P. Dagaut. Effects of dilution on laminar burning velocity of premixed methane/air flames. *Energy and Fuels*, 25:948–954, 2011.

[82] J. Li, Z. Zhao, A. Kazakov, M. Chaos, and F.L. Dryer. A comprehensive kinetic mechanism for CO, CH_2O and CH_3OH combustion. *Int. J. Chem. Kinet.*, 39(3):109–136, 2007.

[83] M.P. Burke, M. Chaos, Y. Ju, F.L. Dryer, and S.J. Klippenstein. Comprehensive H_2/O_2 kinetic model for high-pressure combustion. *Int. J. Chem. Kinet.*, 44:444–474, 2012.

[84] M. Goswami, R.J.M. Bastiaans, A.A. Konnov, and L.P.H. de Goey. Laminar burning velocity of lean H_2-CO mixtures at elevated pressure using the heat flux method. *Int. J. Hydrogen Energy*, 39:1485–1498, 2014.

[85] M.P. Burke, F.L. Dryer, and Y. Ju. Assessment of kinetic modeling for lean $H_2/CH_4/O_2$/diluent flames at higher pressures.

[86] S.G. Davis, A.V. Joshi, H. Wang, and F.N. Egolfopoulos. An optimized kinetic model of H_2/CO combustion. *Proc. Combust. Inst.*, 30:1283–1292, 2005.

[87] C.I. Heghes. $\mathrm{C}_1 - \mathrm{C}_4$ *Hydrocarbon Oxidation Mechanism.* PhD thesis, University of Heidelberg, 2006.

[88] A.A. Konnov. Remaining uncertainties in the kinetic mechanism of hydrogen combustion. *Combust. Flame*, 152:507–528, 2008.

[89] I. Gy. Zsely, J. Zador, and T. Turanyi. Uncertainty analysis of updated hydrogen and carbon monoxide oxidation mechanisms. *Proc. Combust. Inst.*, 30:1273–1281, 2005.

[90] P. Saxena and F.A. Williams. Testing a small detailed chemical-kinetic mechanism for the combustion of hydrogen and carbon monoxide. *Combust. Flame*, 145:316–323, 2006.

[91] R. Sivaramakrishnan, A. Comandini, R.S. Tranter, K. Brezinsky, S.G. Davis, and H. Wang. Combustion of CO/H_2 mixtures at elevated pressures. *Proc. Combust. Inst.*, 31:429–437, 2007.

[92] K.J. Hughes, T. Turanyi, A.R. Clague, and M.J. Pilling. Development and testing of a comprehensive chemical mechanism for the oxidation of methane. *Int. J. Chem. Kinet.*, 33:513–538, 2001.

[93] D.L. Baulch, C.T. Bowman, C.J. Cobos, R.A. Cox, T. Just, J.A. Kerr, M.J. Pilling, D. Stocker, J. Troe, W. Tsang, R.W. Walker, and J. Warnatz. Evaluated kinetic data for combustion modeling: Supplement II. *J. Phys. Chem. Ref. Data*, 34(3):757–1397, 2005.

[94] J. Li, Z. Zhao, A. Kazakov, and F.L. Dryer. An updated comprehensive kinetic model of hydrogen combustion. *Int. J. Chem. Kinet.*, 36:566–575, 2004.

[95] D. Fulle, H.F. Hamann, H. Hippler, and J. Troe. High pressure range of addition reactions of HO. II. Temperature and pressure dependence of the reaction HO + CO $\Leftrightarrow$ HOCO $\rightarrow$ H + CO_2. *J. Chem. Phys.*, 105:983–1000, 1996.

[96] E.L. Peterson, D.M. Kalitan, A.B. Barrett, S.C. Reehal, J.D. Mertens, D.J. Beerer, R.L. Hack, and V.G. McDonell. New syngas/air ignition data at lower temperature and elevated pressure and comparison to current kinetics models. *Combust. Flame*, 149:244–247, 2007.

[97] M. O'Connaire, H.J. Curran, J.M. Simmie, W.J. Pitz, and C.K. Westbrook. A comprehensive modeling study of hydrogen oxidation. *Int. J. Chem. Kinet.*, 36:603–622.

[98] G. Mittal, C.J. Sung, M. Fairweather, A.S. Tomlin, J.F. Griffiths, and K.J. Hughes. Significance of the $HO_2 + CO$ reaction during the combustion of $CO + H_2$ mixtures at high pressures. *Proc. Combust. Inst.*, 31:419–427, 2007.

[99] S.M. Walton, X. He, B.T. Zigler, and M.S. Woolridge. An experimental investigation of the ignition properties of hydrogen and carbon monoxide mixtures for syngas turbine applications. *Proc. Combust. Inst.*, 31(1):3147–3154, 2007.

[100] A. Burcat and B. Ruscic. Third Millennium Ideal Gas and Condensed Phase Thermochemical Database for Combustion with updates from Active Thermochemical Tables. *ANL-05/20 and TAE 960 Technion-IIT, Aerospace Engineering and Argonne National Laboratory Chemistry Division*, 2005".

[101] N. Cohen and K.R. Westberg. Chemical kinetic data sheets for high-temperature chemical reactions. *J. Phys. Chem. Ref. Data*, 12:531, 1983.

[102] J. Warnatz and W.C. Gardiner Jr (Ed.). *Combustion Chemistry, Springer-Verlag*, page 197, 1984.

[103] V. Naudet, S. Javoy, and C.E. Paillard. A high temperature chemical kinetics study of the reaction: $OH + Ar = H + O + Ar$ by atomic resonance absorption spectrophotometry. *Combust. Sci. Technol.*, 164:113–128, 2001.

[104] J. Troe. Detailed modeling of the temperature and pressure dependence of the reaction $H + O_2$ (+M) $\rightarrow HO_2$ (+M). *Proc. Combust. Inst.*, 28:1463–1469, 2000.

[105] R.W. Bates, D.M. Golden, R.K. Hanson, and C.T. Bowman. Experimental study and modeling of the reaction $H + O_2 + M \rightarrow HO_2 + M$ ($M = Ar$, N_2, H_2O) at elevated pressures and temperatures between 1050 and 1250 K. *Phys. Chem. Chem. Phys.*, 3:2337–2342, 2001.

[106] D.L. Baulch, C.J. Cobos, R.A. Cox, T. Just, J.A. Kerr, M.J. Pilling, D. Stocker, J. Troe, W. Tsang, R.W. Walker, and J. Warnatz. Summary table of evaluated kinetic data for combustion modeling: Supplement I. *J. Phys. Chem. Ref. Data*, 98:59–79, 1994.

[107] Z. Hong, D.F. Davidson, E.A. Barbour, and R.K. Hanson. A new shock tube study of the $H + O_2 \rightarrow OH + O$ reaction rate using tunable diode laser absorption of H_2O near 2.5 μm. *Proc. Combust. Inst.*, 33:309–316, 2011.

[108] R. Atkinson, D.L. Baulch, R.A. Cox, R.F. Hampson Jr., J.A. Kerr, M.J. Rossi, and J. Troe. Evaluated kinetic and photochemical data for atmospheric chemistry: Supplement VI. *J. Phys. Chem. Ref. Data*, 26:1329–1799, 1997.

[109] M.A. Mueller, T.J. Kim, R.A. Yetter, and F.L. Dryer. Flow reactor studies and kinetic modeling of the H_2/O_2 reaction. *Int. J. Chem. Kinet.*, 31:113–125,

1999.

[110] S.P. Karkach and V.I. Osherov. Ab initio analysis of the transition states on the lowest triplet H_2O_2 potential surface. *J. Chem. Phys.*, 110:11918–11927, 1999.

[111] Ch Kappel, K. Luther, and J. Troe. Shock wave study of the unimolecular dissociation of H_2O_2 in its falloff range and of its secondary reactions. *Phys. Chem. Chem. Phys.*, 4:4392–4398, 2002.

[112] R. Atkinson, D.L. Baulch, R.A. Cox, J.N. Crowley, R.F. Hampson, R.G. Hynes, M.E. Jenkin, M.J. Rossi, and J. Troe. Evaluated kinetic and photochemical data for atmospheric chemistry: Volume III Ű gas phase reactions of inorganic halogens. *Atmos. Chem. Phys.*, 7:981–1191, 2005.

[113] W. Tsang and R.F. Hampson. Chemical kinetic data base for combustion chemistry. Part I. Methane and related compounds. *J. Phys. Chem. Ref. Data*, 15:1087–1279, 1986.

[114] H. Hippler, H. Neunaber, and J. Troe. Shock wave studies of the reactions $HO + H_2O_2 \rightarrow H_2O + HO_2$ and $HO + HO_2 \rightarrow H_2O + O_2$ between 930 and 1680 K. *J. Chem. Phys.*, 103:3510–3516, 1995.

[115] M.T. Allen, R.A. Yetter, and F.L. Dryer. High pressure studies of moist carbon monoxide/nitrous oxide kinetics. *Combust. Flame*, 109:449–470, 1997.

[116] J. Troe. Thermal dissociation and recombination of polyatomic molecules. *15th Symposium(International) on Combustion/ The combustion Institute*, pages 667–680, 1975.

[117] G. Friedrichs, D.F. Davidson, and R.K. Hanson. Direct measurements of the reaction $H + CH_2O \rightarrow H_2 + HCO$ behind shock waves by means of vis-UV detection of formaldehyde. *Int. J. Chem. Kinet.*, 34:374–386, 2002.

[118] C.W. Larson, P.H. Stewart, and D.M. Golden. Pressure and temperature dependence of reactions proceeding via a bound complex. An approach for combustion and atmospheric chemistry modelers. Application to $HO + CO \rightarrow [HOCO] \rightarrow H + CO_2$. *Int. J. Chem. Kinet.*, 20:27–40, 1988.

[119] H.G. Yu, J.T. Muckerman, and J.S. Francisco. Direct ab initio dynamics study of the OH + HOCO reaction. *J. Phys. Chem. A*, 109:5230–5236, 2005.

[120] H.G. Yu and J.T. Muckerman. Quantum molecular dynamics study of the reaction of O_2 with HOCO. *J. Phys. Chem. A*, 110:5312–5316, 2006.

[121] J.V. Michael, N.-C. Su, J.W. Sutherland, J.J. Carroll, and A.F. Wagner. Rate constants for $H + O_2 + M \rightarrow HO_2 + M$ in seven bath gases. *J. Phys. Chem. A*, 106:5297–5313, 2002.

[122] R.X. Fernandes, K. Luther, J. Troe, and V.G. Ushakov. Experimental and modelling study of the recombination reaction $H + O_2$ (+M) $\rightarrow HO_2$ (+M) between 300 and 900 K, 1.5 and 950 bar, and in the bath gases M = He, Ar and N_2. *Phys. Chem. Chem. Phys.*, 10:4313–4321, 2008.

[123] J.W. Sutherland, J.V. Michael, and A.N. Pirraglia. Rate constant for the reaction of $O(_3P)$ with H_2 by the flash photolysisŮshock tube and flash photolysisŮresonance fluorescence techniques; 504 K $\leq$ T $\leq$ 2495 K. *Proc. Combust.*

Inst., 21:929–941, 1988.

[124] S.M. Hwang, S.O. Ryu, K.J. De Witt, and M.J. Rabinowitz. High temperature rate coefficient measurements of $H + O_2$ chain-branching and chain-terminating reaction. *Chemical Physics Letters*, 408:107–111, 2005.

[125] J. Troe and W.C. Gardiner Jr (Ed.). *Combustion Chemistry, Springer-Verlag*, pages 171–196, 1984.

[126] P.R. Westmoreland, J.B. Howard, J.P. Longwell, and A.M. Dean. Prediction of rate constants and pyrolysis reactions by bimolecular QRRK. *AIChE Journal*, 32:1971–1979, 1986.

[127] J. Warnatz, R.W. Dibble, and U. Maas. *Combustion, Physical and Chemical Fundamentals, Modeling and Simulation, Springer-Verlag*, 1996.

[128] J. Troe. Modeling the temperature and pressure dependence of the reaction $HO + CO \rightleftharpoons HOCO \rightleftharpoons H + CO_2$. *27th Symposium(International) on Combustion/ The combustion Institute*, 15:167–175, 1998.

[129] T.J. Kim, R.A. Yetter, and F.L. Dryer. New results on moist CO oxidation: high pressure, high temperature experiments and comprehensive kinetic modeling. *25th Symposium(International) on Combustion/ The combustion Institute*, pages 759–766, 1994.

[130] R.S. Timonen, E. Ratajczk, and D. Gutman. Kinetics of the reactions of the formyl radical with oxygen, nitrogen dioxide, chlorine and bromine. *J. Phys. Chem.*, 92:651–655, 1988.

[131] Z. Zhao, J. Li, A. Kazakov, and F.L. Dryer. Temperature-dependent feature sensitivity analysis for combustion modeling. *Int. J. Chem. Kinet.*, 37:282–295, 2005.

[132] D.L. Baulch, C.J. Cobos, R.A. Cox, C. Esser, P. Frank, T. Just, J.A. Kerr, M.J. Pilling, J. Troe, R.W. Walker, and J. Warnatz. Evaluated kinetic data for combustion modeling. *J. Phys. Chem. Ref. Data*, 21:411, 1992.

[133] A. Miyoshi, H. Matsui, and N. Washida. Detection and reactions of the HOCO radical in gas phase. *J. Chem. Phys.*, 100:3532–3539, 1994.

[134] J.T. Petty, J.A. Harrison, and C.B. Moore. Reactions of trans-HOCO studied by infrared spectroscopy. *J. Phys. Chem.*, 97:11194, 1993.

[135] J. Nolte, J. Grussdorf, F. Temps, and H. Gg Wagner. Kinetics of the Reaction of HOCO with O_2 in the Gas Phase. *Z. Naturforsch. A*, 48:1234–1238, 1993.

[136] G. Poggi and J.S. Francisco. An ab initio study of the competing reaction channels in the reaction of HOCO radicals with NO and O_2. *J. Chem. Phys.*, 120:5073–5080, 2004.

[137] A. Kazakov. *Personal Communication*, 2004.

[138] A.E. Lutz, R.J. Kee, and J.A. Miller. *Senkin: Report SAND-87-8248; Sandia National Laboratories, Albuquerque*, 1988.

[139] R.A. Yetter, F.L. Dryer, and H. Rabitz. Flow reactor studies of carbon monoxide/hydrogen/oxygen kinetics. *Combust. Sci. Technol.*, 79(1-3):129–140, 1991.

[140] A.A. Paletskii, L.V. Kuibida, T.A. Bolshova, O.P. Korobeinichev, and R.M.

Fristrom. Study of the structure of a tem-atmosphere H_2-O_2-Ar flame using molecular-beam inlet mass-spectrometric probing. *Combust. Explos. Shock Waves*, 32(3):245–250, 1996.

[141] U. Struckmeier, P. Oßwald, T. Kasper, L. Böhling, M. Heusing, M. Kohler, A. Brockhinke, and K. Kohse-Höinghaus. Sampling probe influences on temperature and species concentrations in molecular beam mass spectroscopinc investigations of flat premixed low-pressure flames. *Z. Phy. Chem.*, 223(4-5):503–537, 2009.

[142] B. Li, J. Lindén, Z.S. Li, A.A. Konnov, M. Aldén, and L.P.H. de Goey. Accurate measurements of laminar burning velocity using the Heat Flux method and thermographic phosphor technique. *Proc. Combust.Inst.*, 33:939–946, 2011.

[143] A.H. Khalid and K. Kontis. Thermographic Phosphors for high temperature measurements: Principles, Current state of the art and recent applications. *Sensors*, 8:5673–5744, 2008.

[144] N. Dam. An introduction to spectroscopy. Lecture notes of the course: Advanced Laser Diagnostics in Combustion Systems., 2010. Course 4P620.

[145] S.W. Allison and G.T. gillies. Remote thermometry with thermographic phosphors: Instrumentation and applications. *Review of Scientific Instruments*, 68:261– 2650, 1997.

[146] ir. C. H. M. Baltis. Measurements on ZnO:Zn samples. 2012.

[147] N. Fuhrmann, Brüback J., and A. Dreizler. Phosphor Thermometry: A Comparison of the Luminescence Lifetime and the Intensity Ratio Approach. *Proc. Combust. Inst.*, 32, 2012.

[148] M. Aldén, A. Omrane, M. Richter, and G. Särner. Thermographic phosphors for thermometry: A survey of combustion applications. *Prog. Energy Combust. Sci.*, 37:422–461, 2011.

[149] G. Särner, M. Richter, and M. Aldén. Two-dimensional thermometry using temperature-induced line shifts of ZnO:Zn and ZnO:Ga fluorescence. *Optics Letters*, 33(12), 2008.

[150] David Pendrill. Phosphor Technologies Ltd (UK). http://www.phosphor-technology.com.

[151] J. Anthony and Y. Qiang. Cathodoluminescence from a device of carbon nanotube-field emission display with ZnO nanocluster phosphor. *Nanotechnology*, 18, 2007.

[152] A.E. Rakhshani, A. Bumajdad, J. Kokaj, and S. Thomas. Structure, composition and optical properties of ZnO:Ga films electrodeposited on flexible substrates. *Applied Physics A Materials Science and Processing*, 97:759–764, 2009.

[153] J. Anthony, X.B. Chen, J. Morrison, J. Bergman, and Y. Qiang. ZnO nanoclusters: Synthesis and photoluminescence. *Applied Physics Letters*, 87, 2005.

[154] A.E. Rakhshani, A. Bumajdad, and J. Kokaj. ZnO films grown by successive chemical solution deposition. *Applied Physics A Material Science & Processing*, 89:923–928, 2007.

[155] B.S. Jeon, J.S. Yoo, and J.D. Lee. Electrophoretic Deposition of ZnO:Zn Phosphor for Field Emission Display Applications. *Journal of the Electrochemical Society*, 143(12), 1996.

Samenvatting

Door de groeiende energiecrisis hebben duurzame brandstoffen een belangrijke opmars gemaakt in de energiesector. Veel technologiën, zoals bijvoorbeeld Integrated Gasification Combine Cycle, werken met hoge drukken en temperaturen. De ontwikkeling van nieuwe technologiën richt zich voornamelijk op het verhogen van de efficiëntie van centrales, brandstof flexibiliteit, carbon capture and storage (CCS) and het omgaan met strikte emissie eisen. Enkele van de brandstoffen die op dit moment veel gebruikt worden zijn aardgas en syngas. De verbrandingseigenschappen van deze gassen zijn erg belangrijk voor veel verschillende doeleinden. Dit geld vooral voor praktisch relevante condities (gas turbine condities: druk $\sim$ 30 bar, instroom temperatuur $\sim$ 673 K en arme mengsels). Dit proefschrift heeft als doel hier aan bij te dragen. De laminaire verbrandingssnelheid is een verbrandingseigenschap van brandstof-oxidator mengsel en is een functie van de druk, temperatuur en equivalentieverhouding. Deze eigenschap wordt gebruikt voor onderzoek naar vlamstabiliteit, vlaminslag en het afblazen van vlammen, voor verschillende branderontwerpen. Verder wordt de laminaire verbrandingssnelheid gebruikt om chemische reactiemechanismes te valideren voor numerieke verbrandingssimulaties.

In dit werk zijn verschillende experimenten uitgevoerd met de heat flux method (HFM) om de laminaire verbrandingssnelheid te vinden voor bepaalde syngas samenstellingen ($H_2/CO/N_2$) en C1-C3 alkanen voor drukken van 1 atm tot 10 atm. Eéndimensionale, adiabatische, uitrekkingsloze vlakke vlammen werden gestabiliseerd op een heat flux method burner. Tegelijk met het onderzoeken van de principes en de werking van een atmosferische heat flux method, zijn er numerieke simulaties uitgevoerd om het effect van de druk en de geometrie van de geperforeerde branderplaat te begrijpen. Om drukeffecten te onderzoeken is er een mogelijkheid opgebouwd om de experimenten bij verhoogde drukken uit te voeren. Voor C1-C3 alkanen zijn er experimenten uitgevoerd voor drukken tot 5 atm, bij 298 K en equivalentieverhoudingen van 0.9 tot 1.4. Daarbij is ook een uitvoerige analyse gemaakt van de drukafhankelijkheid van methaan - lucht mengels. Dergelijke correlaties zijn ook gevonden voor ethaan - lucht en propaan lucht mengels. Experimenten voor syngas mengels (50:50

H_2-CO, 85:15 H_2-CO and 85:15 H_2-N_2) zijn uitgevoerd van atmosferische druk tot 10 atm, bij 298 K en zuurstofarme condities (equivalentieverhouding tot 0.5), omdat deze data schaars is in de bestaande literatuur. Een chemisch reactiemechanisme voor syngas mengels is vernieuwd en gevalideerd met deze experimentele resultaten en die uit de bestaande literatuur voor een groot bereik van drukken, temperaturen en equivalentie verhoudingen. Naast een onderzoek naar het uitbreiden van de heat flux method voor verhoogde drukken, is er getracht een onconventionele (niet verstorende) thermophosphor techniek toe te passen om de precisie van het HFM systeem te beoordelen. Conventionele heat flux method experimenten met methaan - lucht mengels en thermokoppels zijn vergeleken met de thermophosphor metingen. De precisie van het systeem met de thermophosphor techniek was vergelijkbaar met het conventionele systeem. Een extra analyse wees uit dat de precisie van de meting verbeterd konden worden door de optische opstelling aan te passen.

Acknowledgements

With my sincere regards I thank Philip, my professor, for his amazing guidance. When I first joined TU/e, I knew I was joining one of the best combustion groups in the world and a very famous professor. With time I saw and understood the inspiration Philip passes on to his students. To add to this, I felt very special because I worked with the very founder of HFM which is the essence of this thesis!

I thank my co-promoter Alexander for extending his great support all the way from Sweden. His expertise in HFM and kinetics came as an important support to this thesis. Even though he supervised me from across the Baltic, he always responded promptly to my queries and discussions. I also acknowledge the support of my daily supervisor, Rob. Apart from helping me through his numerical expertise, his critical remarks on my scientific writing has steered me into becoming a better writer.

TU/e provides its doctoral students a large exposure to the research world by sending them to conferences, laboratories in other universities and research institutes and handling international projects. Along the way, I met many experienced people and learnt lot many things from them. Some of them include Fokion Egolfopoulos (USC), Dirk Roekaarts (Delft), Roy Hermanns (OWI), Peter Jahnson (PSI), Peter Griebel (DLR) and Henry Curran (NUI). The financial support for this dissertation by the European Union within the H_2-IGCC project (agreement no. 2393349) is also gratefully acknowledged.

The work in this thesis was made possible by the assistance of Hans, Bart, Gerard, Theo and Henri who are my colleagues at the combustion laboratory. I also acknowledge Nico Dam, Viktor Kornilov, Jereon van Oijen and Bart Somers for sharing their expertise. I want to thank all my colleagues especially Atieh, Akshay, Nico, Marjan, Miao (Tian), Thiago, Alessio, Ebrahim, Marcelo, Evgeniy, Sander, Kris and Mara for the great time spent here at the university. This place was the perfect platform where I learnt so much more about people from all across the globe. Like in my culture, I fold my hands together in gratitude and thank all of you once again.

A few people who have become my great friends for life are Kapur uncle (*dadaji*), Nidhi, Manohar and Anjan Sir. Thank you for being there for me.

With great pleasure, I thank my family for their amazing support. My *deuta*, who understands me in every respect, is a great father a girl can ask for. His confidence in me at every step of my life has brought me to this doctor's title today. Thank you, *Maa*, you took care of me always like your little girl. Many thanks to my brother Mayur and sister Manjari, for their love, affection, understanding, fights, pranks, jokes and rebellions (at times). I also want to take this opportunity to thank my wonderful (late) grandfather. He was a Sanskrit scholar with an eye for perfection. In his last note to me, he blessed me to be a 'Gargi', a 'Maitreyi' (Indian women scholars from Vedic times). And finally, with all my heart, I thank Kiran, my husband, without whom life wouldn't be so beautiful for sure. Your love and support has made me sail through many difficult times. You are my best friend, indeed!

Curriculum Vitae

Mayuri Goswami

14 August 1985	Born in Jorhat, India
1990 - 2002	Secondary school: Kendriya Vidyalaya Delhi, Guwahati, Chennai (India)
2002 - 2006	Bachelor of Mechanical Engineering Anna University, Chennai (India)
2007-2009	Master of Technology, Thermal Engineering Indian Institute of Technology, Delhi (India)
2010 - 2014	PhD research Section Combustion Technology Department of Mechanical Engineering Technische Universiteit Eindhoven (Netherlands)

Publications

Journals

- M. Goswami, S. Derks, K. Coumans, W.J. Slikker, M.H. de Andrade Oliveira, R.J.M Bastiaans, A.A. Konnov and L.P.H. de Goey. The effect of elevated pressures on the laminar burning velocity of methane+air mixtures. *Combustion and Flame* 160 (2013) 1627-1635.
- M. Goswami, R.J.M Bastiaans, A.A. Konnov and L.P.H. de Goey. Laminar burning velocity of lean H_2-CO mixtures at elevated pressure using the heat flux method. *International Journal of Hydrogen Energy* 39 (2014) 1485-1498.

- M. Goswami, K. Coumans, R.J.M Bastiaans, A.A. Konnov and L.P.H. de Goey. Numerical simulations of flat laminar premixed methane-air flames at elevated pressure. *Combustion Science and Technology* (Accepted) (2014).

- M. Goswami, J.G.H. van Griensven, R.J.M Bastiaans, A.A. Konnov and L.P.H. de Goey, Experimental and modeling study of the effect of elevated pressure on lean high-hydrogen syngas flames. Submitted to *Proc. Combust. Inst.* 35 (2015).

Conference - Refereed proceedings

- M. Goswami, R.J.M. Bastiaans, L.P.H. de Goey and A.A. Konnov . Laminar burning velocity of lean H_2-CO mixtures at elevated pressure using the heat flux method. 24th International colloquim on dynamics of explosions and reactive systems (ICDERS), Taipei, Taiwan, 28 July - 2 August, 2013.

- M. Goswami, K. Coumans, R.J.M. Bastiaans, L.P.H. de Goey and A.A. Konnov. Numerical simulations of flat laminar premixed CH_4/air flames at elevated pressure. 24th International colloquim on dynamics of explosions and reactive systems (ICDERS), Taipei, Taiwan, 28 July - 2 August, 2013.

- M. Goswami, S.C.R. Derks, K. Coumans, M.H. Andrade Oliveira, A.A. Konnov, R.J.M. Bastiaans, C.C.M. Luijten and L.P.H de Goey. Effect of elevated pressures on laminar burning velocity of methane + air mixtures using heat flux method. 23rd International Colloquium on the Dynamics of Explosions and Reactive Systems (ICDERS), Irvine, USA, July 24 - 29, 2011.

- M. Goswami, R.J.M. Bastiaans, L.P.H. de Goey and A.A. Konnov. Updated chemical reaction mechanism for methane combustion at high pressure. 7th International Conference on Chemical Kinetics (ICCK), MIT, Massachusetts, USA, July 10 - 14, 2011.

Conference - Non-refereed proceedings

- M. Goswami, M. Wustmans, N.J. Dam, A.A. Konnov, R.J.M. Bastiaans and L.P.H. de Goey. Temperature measurement for the heat flux method using ZnO:Zn thermophosphor. 6th European Combustion Meeting, Lund, Sweden, June 2013.

- M. Goswami, R.J.M. Bastiaans, L.P.H. de Goey and A.A. Konnov. Syngas combustion at high pressure. 5th European Combustion Meeting, Cardiff, UK, June 2011.
- M. Goswami, R.J.M. Bastiaans, A.A. Konnov and L.P.H. de Goey. Modeling study of H_2/Air combustion and NO_x formation at high pressures. 8th Asia-Pacific Conference on Combustion, Hyderabad, India, December 2010.